An Experimental Study of Shock/Turbulent Boundary Layer Interactions at DNS Accessible Reynolds Numbers

Patrick Brian Bookey

A THESIS PRESENTED TO THE FACULTY
OF PRINCETON UNIVERSITY IN CANDIDACY FOR
THE DEGREE OF MASTER OF SCIENCE IN ENGINEERING

RECOMMENDED FOR ACCEPTANCE BY THE DEPARTMENT OF
MECHANICAL AND AEROSPACE ENGINEERING

May 2005

Report Documentation Page

Form Approved
OMB No. 0704-0188

1. REPORT DATE	2. REPORT TYPE	3. DATES COVERED
01 MAY 2005	**N/A**	**-**

4. TITLE AND SUBTITLE	5a. CONTRACT NUMBER
An Experimental Study of Shock/Turbulent Boundary Layer Interactions at DNS Accessible Reynolds Numbers	5b. GRANT NUMBER
	5c. PROGRAM ELEMENT NUMBER
6. AUTHOR(S)	5d. PROJECT NUMBER
	5e. TASK NUMBER
	5f. WORK UNIT NUMBER
7. PERFORMING ORGANIZATION NAME(S) AND ADDRESS(ES) **Princeton University**	8. PERFORMING ORGANIZATION REPORT NUMBER
9. SPONSORING/MONITORING AGENCY NAME(S) AND ADDRESS(ES)	10. SPONSOR/MONITOR'S ACRONYM(S)
	11. SPONSOR/MONITOR'S REPORT NUMBER(S)

12. DISTRIBUTION/AVAILABILITY STATEMENT
Approved for public release, distribution unlimited

13. SUPPLEMENTARY NOTES
The original document contains color images.

14. ABSTRACT

15. SUBJECT TERMS

16. SECURITY CLASSIFICATION OF:			17. LIMITATION OF ABSTRACT	18. NUMBER OF PAGES	19a. NAME OF RESPONSIBLE PERSON
a. REPORT	b. ABSTRACT	c. THIS PAGE			
unclassified	**unclassified**	**unclassified**	**UU**	**147**	

An Experimental Study of Shock/Turbulent Boundary Layer Interactions at DNS Accessible Reynolds Numbers

Prepared by:

Patrick B. Bookey

Approved by:

Alexander J. Smits	M. Pino Martin
Professor	Assistant Professor
Thesis Advisor	Thesis Reader

Abstract

An experimental investigation was conducted to study four shock/turbulent boundary layer interactions at the Princeton University Gas Dynamics Laboratory. In Mach 2.9 flow, a 24º compression corner and a 12º reflected shock interaction were studied at $Re_\theta = 2400$. In Mach 8 flow, an 8º compression corner and a 10º sharp fin were studied at $Re_\theta = 3500$. The flow was examined through the use of surface oil flow visualization, surface pressure measurements, mean Pitot pressure and total temperature surveys and condensate-enhanced filtered Rayleigh scattering (FRS). The combination of these experimental techniques allowed the determination of velocity profiles, separation and reattachment points, mean surface pressure distribution, key surface features and provided information on the large-scale structures in the boundary layer through the shock interactions. This low Reynolds number experimental data is intended to form the foundation for a future, larger database of experimental data to which DNS computations can be directly compared at the same Reynolds numbers.

The 24º compression corner interaction at Mach 2.9 produced a fully separated flow with the characteristic lengths of separation and mean pressure distribution significantly different than those of higher Reynolds numbers. The FRS images revealed a highly unsteady separation shock that was disturbed by passing large structures. The organized structures showed very little change through the interaction. The 12º reflected shock interaction produced the characteristics of a fully separated flow, with the height of the separation bubble on the order of the incoming boundary layer height. The point of intersection of the incident and separation shocks was unsteady.

The 8º compression corner at Mach 8 was found to remain attached from surface oil flow visualizations, contrary to expectations. The shockwave was deeply entrained in the boundary layer and was highly distorted by passing large turbulent structures for several boundary layer thicknesses downstream of the corner. The 10º sharp fin interaction revealed the quasiconical symmetry of this type of interaction.

Acknowledgements

My stay here at Princeton has been a very short year and a half. However, in that time, there are many people that have helped me in my academic courses, joined me for endless hours in the laboratory, and become my very good friends. Their contributions to this work are as much as my own and they deserve recognition.

My greatest thanks go to Chris Wyckham, my partner in crime out at the Gas Dynamics Lab. He essentially put a lot of his PhD work on hold to help me in nearly every aspect of the experiments. We experienced 24-hour shifts watching the compressors, the failure of nearly every piece of equipment we operated and countless hours examining mysterious pressure signals. I am extremely thankful for his help and guarantee this work could not have been completed as quickly as it was without him. Good luck to him finishing his PhD and continuing his love of flying.

Bob Bogart, another Navy man, was extremely helpful with all things out at Gas Dynamics. Bob is a generous man who never hesitated to stop what he was doing to help out with any problem I was having with the wind tunnels and various other equipment. When we were under the gun to meet a deadline, he came in early on Father's Day to help us complete a run. Bill Stokes was also of great help when I was first starting out on the LTVG. Bill Dix is an amazing machinist and made nearly all the models used in these experiments. Larry and Barry in the SEAS machine shop helped in emergency modifications to models. Scott from AirGas was of great help in supplying our never-ending need for bottles of carbon dioxide and helium.

Prof. Lex Smits was a great advisor and it was a pleasure working with him. He took me on as a Master's student and pushed me so that I could finish my degree in 18 months and get back to the Navy. He is an excellent instructor and always seemed to have the answers to the seemingly unsolvable problems I encountered. To him and the other Gas Dynamics Laboratory graduate students, I am grateful for their support and guidance. Prof. Pino Martin graciously agreed to read my thesis and her comments and suggestions were extremely helpful in the completion of this document.

My best friends and roommates here at Princeton were Tom Smith and Tim Ombrello. Fellow motorheads, they taught me a lot about the intricacies of the automobile. Tim's '79 Camaro and Tom's '68 Nova have me convinced that I need to join them in owning a classic American muscle car. I'll always remember the night Beavis made an appearance at the Graduate College dinner table and our nights playing pool at the D-bar. Tim is the hardest working person I've ever met in my life. Tom is, well….Tom. Good luck to both of them.

The rest of the crew in MAE at Princeton: Melissa, Luke, Luca, Laurent (Frenchy), Mike and Val, MAE Softball Team, Ben, Manny, Amir, Sunil, Jessica, and everybody else. I wouldn't have passed any of my classes without the group effort. Janel, thanks for your constant support.

My family has always been there for me. My parents, Brian and Renee Bookey, have been behind me even when I decided to enter the military and move to the other side of the country to go to the Naval Academy. My successes are directly attributed to their love and support through the many trials and tribulations I have put myself through in my academic career. I would not be the person I am today without such great parents. My

brother Mike, despite being the polar opposite of myself as he pursues degrees in English and Screenwriting, has always been and always will be my best friend. He is the funniest person I know and his writing has always amazed me. My sister Meghan and I have in the past few years grown so much closer and she, the youngest, always seems to have the best advice when things are down. I love my family and thank them for supporting me throughout the course of this work.

This work was supported by the Air Force Office of Scientific Research under grant # F49620-02-1-0361, monitored by Dr. John Schmisseur. This thesis carries the number 3134-T in the records of the Department of Mechanical and Aerospace Engineering.

Table of Contents

List of Figures

List of Tables

Nomenclature

a	speed of sound
CFD	Computational Fluid Dynamics
C	correlation coefficient
D	computational domain size
DNS	Direct Numerical Simulation
FRS	Filtered Rayleigh Scattering
H	shape factor
L_i	inception length
M	local Mach number
M_n	Mach number normal to oblique shock
N_{xyz}	number of computational meshpoints
q	turbulence velocity scale
r	recovery factor
RANS	Reynolds Averaged Navier Stokes
Re	Reynolds number
Re_θ	Reynolds number based on momentum thickness $\equiv \rho_\infty U_\infty \theta / \mu_\infty$
$Re_{\delta o}$	Reynolds number based on boundary layer thickness $\equiv \rho_\infty U_\infty \delta_0 / \mu_\infty$
Re/m	unit freestream Reynolds number
Re_T	turbulent Reynolds number $\equiv q^4 / \varepsilon$
P	pressure
P_0	stagnation (total) pressure
psi(a)	pounds per square inch (absolute)
T	temperature
T_0	stagnation (total) temperature
U	velocity
u_τ	friction velocity
VCO	Virtual Conical Origin
x,y,z	Cartesian coordinates, respectively streamwise, wall-normal, and spanwise

X_U	upstream influence length
X_S	separation length
$y_{0.5}$	mean position of the superlayer
α	compression ramp or sharp fin angle
β	angle of surface features in spherical polar coordinates
β_U	upstream influence line
β_{S1}	primary separation line
β_{S2}	secondary separation line
β_{A1}	primary reattachment line
β_0	inviscid shock trace
δ	boundary layer thickness
$\delta_{0.99}$	boundary layer thickness ($U = 0.99U_\infty$)
δ_0	incoming boundary layer thickness
δ^*	displacement thickness
Δ	mesh size
ε	dissipation rate per unit mass
η	Kolmogorov length scale
θ	momentum thickness
λ	intermittency function, Taylor microscale, sharp fin shock structure
Λ	integral length scale
μ	molecular viscosity or mach angle
ν	kinematic viscosity
ρ	density
τ	stress
φ	reflected shock turning angle

Subscripts

aw	adiabatic wall condition
e	boundary layer edge condition
w	wall quantity
∞	freestream quantity

Chapter 1 Introduction

1.1 Motivation

1.1.1 Shock/Turbulent Boundary Layer Interaction Research

The study of high-speed aerodynamics has received great attention in the past few decades due to the creation of many exciting projects in the supersonic and hypersonic flight regime. New weapons systems, reusable reentry vehicles, hypersonic airplanes, and scramjet engine design push forward the need for a better understanding of the nature of supersonic and hypersonic flows. In November 2004, NASA successfully tested the X-43A research aircraft, which flew to nearly Mach 9.8 at 110,000 feet powered by a scramjet. The X-43A, shown in Figure 1.1, is the first aircraft to prove the feasibility of high-speed air-breathing propulsion. The application of this technology to a practical aircraft could make long-distance and space travel more economical and safer. However, in order to make these leaps in technology, a great deal of data over a large range of supersonic and hypersonic flight conditions must be collected and understood. The success of such projects as the X-43A has and will continue to depend on the fundamental understanding of high-speed aerodynamics.

There are many areas of high-speed aerodynamics that are of critical importance to the design of new high-speed aircraft. One of these areas is the interaction of a shock wave with a turbulent boundary layer. Boundary layers develop on any surface exposed to the moving freestream air and in most cases become turbulent over a great deal of the surface. A shock/boundary layer interaction occurs from two basic mechanisms. When

the supersonic flow is turned abruptly, a shock is generated which interacts with the boundary layer. This type of interaction might occur on engine inlet ramp or a deflected control surface, creating a compression ramp interaction which is nominally two-dimensional in nature. It may also occur on the intersection of the wing and body of an aircraft or extruding struts, which create a sharp fin interaction. Shock/boundary layer interactions can also occur when an externally generated shock impinges on the boundary layer. This type of interaction occurs in internal flows such as engines where the shock from the inlet reflects off the surface of the interior of the engine, interacting with the boundary layer on that surface. If the interaction is strong enough, the flow may separate in the corner or at the surface of the shock impingement, causing the shock motion to become highly unsteady. The detail of these interactions will be studied in greater depth later in this chapter, but this section has highlighted the importance of gaining a fundamental understanding of the structure of these interactions.

Figure 1.1: NASA X-43A hypersonic research vehicle. From NASA fact sheet (2004).

1.1.2 Computational Studies

Shock/boundary layer interactions occur over a very large range of Mach and Reynolds numbers representing the vast real flight regime. Experimental facilities are often limited in their ability to simulate only a small range of flight conditions and experiments can prove to become very expensive projects. With the dramatic developments in computing power in the past few years, designers are turning to computational fluid dynamics (CFD) to predict flows that are either too expensive or out of range of available experiment facilities. CFD can produce very accurate predictions of many aspects of shock/turbulent boundary layer interactions, including surface pressure, skin friction distributions, velocity profiles, and even information on the turbulent flowfield. These all depend on the type of computation. In most engineering applications, calculations are based on the Reynolds-Averaged-Navier-Stokes (RANS) equations, incorporating some models for the turbulence. These turbulent models have not been calibrated for complicated flows, such as in a separated compression corner interaction, and current turbulence models lead to highly inaccurate results.

In Direct Numerical Simulation (DNS), in contrast to RANS, the full three-dimensional time-dependent Navier-Stokes equations are solved exactly, thus computing the evolution of all significant scales of motion with no modeling assumptions. The accuracy of DNS greatly depends on the numerical methods employed and the size of the grid. Some of the earliest work was done using spectral methods, providing very accurate spatial differentiation (Orszag and Patterson 1972). Rai and Moin (1989) showed promising results using higher-order finite differences methods for more complex models. Wu and Martin (2005) used a 3rd order, bandwidth optimized WENO (Weighted

Essential Non-Oscillatory) scheme in their DNS of shock/turbulent boundary layer interaction. A discussion of the details of DNS and the various numerical methods used in DNS computations is beyond the scope of this thesis. However, in order to better explain the motivation for the experiments carried out in this study, the following is a discussion on the resolution requirements of DNS.

Reynolds (1991) provided an excellent discussion on the variation of mesh requirements with Reynolds number. DNS is limited to low Reynolds number by the computational resolution, but must resolve both the smallest and largest eddies. As an upper bound for three-dimensional DNS, Reynolds considered the number of meshpoints necessary for homogeneous isotropic turbulence. The smallest length scale that must be resolved was estimated to be $l = 4\eta$, where η is the Kolmogorov scale [$\eta = (\nu^3/\varepsilon)^{1/4}$] and the largest scale, L, to resolve was twice the longitudinal integral scale, Λ. Taking these assumptions into account, the ratio of the largest to smallest scales that must be resolved in each direction is:

$$\frac{L}{l} = \frac{2\Lambda}{4\eta} \approx 0.15\,\mathrm{Re}_T^{3/4} \tag{1.1}$$

where $\mathrm{Re}_T = q^4/(\varepsilon\nu)$ is the Reynolds number of the large-scale turbulence. A more familiar Reynolds number to experimentalists is that based on the Taylor microscale, λ, and the rms longitudinal velocity fluctuation. The two Reynolds numbers are related by $\mathrm{Re}_\lambda = 1.8\sqrt{\mathrm{Re}_T}$. W.C. Reynolds stated that the mesh size Δ must be $l/2$ to resolve eddies of scale l, and the domain, D, must be larger than L. He argues that $D = 4L$ sufficiently captures enough large eddies to compute turbulence statistics. Therefore the number of meshpoints required for homogeneous isotropic turbulence is:

$$N_{xyz} = \left(\frac{D}{\Delta}\right)^3 \approx 1.7\,\mathrm{Re}_T^{9/4} \approx 0.1\,\mathrm{Re}_\lambda^{9/2} \tag{1.2}$$

Boundary layers, appropriate to the current study, require slightly different requirements due to differences in computational domain requirements. Spalart (1988) conducted simulations on a flat plate boundary layer at Re_θ = 1,410 using about 10^7 meshpoints. Reynolds estimated the number of gridpoints necessary for computations similar to Spalart as:

$$N_{xyz} \approx 10^7 \times \left(\frac{\mathrm{Re}_\theta}{1410}\right)^{2.7} \tag{1.3}$$

It is now apparent from the estimates for the number of meshpoints necessary to resolve the range of turbulent scales that DNS is inherently limited to relatively low Reynolds numbers. As seen above, increasing the Reynolds number dramatically increases the number of meshpoints, which in turn increases demands on computing power and time. Recently, computing power has increased significantly and the ability of DNS to compute complex flows at a greater range of operating conditions is proving to be invaluable in shedding insight into turbulence physics.

As for shock/turbulent boundary layer interactions, DNS has real potential to provide the data unattainable by experiment. In 1998, NATO established RTO Working Group 10 with a subgroup assigned to study shockwave/turbulent-boundary layer interactions combining experiments and simulations. A great deal of insight has been gained from the efforts of this subgroup (Knight, 2002 and Knight et al., 2002). However, the experiments and computations were not performed at the same Reynolds number, making the resulting disagreement among experimental and computational data very difficult to diagnose. A clear demonstration of this fundamental limitation was the

DNS study by Adams (2000) at Mach 3 and $Re_\theta = 1{,}685$, where the comparable experimental data were only available at much higher Reynolds numbers.

1.1.3 Current Shock/Turbulent Boundary Layer Computations

The Crocco Laboratory at Princeton University has undertaken a project to compute shock/turbulent boundary layer interactions using DNS and LES. At the time of publication of this thesis, computations had been completed on two configurations at Mach 2.9: a 24º compression corner and a 12º reflected shock interaction at $Re_\theta = 2400$ (Wu and Martin, 2004; Wu et al., 2005). Initial comparisons of the numerical results have shown fairly good agreement with the experimental data of much higher Reynolds number ($Re_\theta \approx 80{,}000$) flows of the same type. However, there are several differences between the computations and experiment that cannot be reconciled due to the major difference in Reynolds number. For example, the computations have shown a significant difference in the surface pressure distribution shortly after the initial pressure rise in the 24º compression corner. All experimental data sets of this configuration show a plateau in the pressure distribution in the separated region, while the DNS data does not reveal this plateau. Wu and Martin (2005) hypothesized that this was possibly due to a Reynolds number effect, since the computations were carried out at a much lower Reynolds number than the corresponding experimental data. However, no definite conclusion could be made at that time due to the lack of experimental data at the same Reynolds number for direct comparison.

At the time of this publication, plans were in place in the Crocco Laboratory for the computation of two additional shock/turbulent boundary layer interactions at Mach 8: an 8º compression corner and 10º sharp fin at $Re_\theta = 3500$. The experimental data

summarized in this thesis is expected to be used for direct comparison to the results of these future computations.

1.1.4 Goals and Overview of Thesis

The purpose of this thesis is to provide experimental data of shock/turbulent boundary layer interactions at Reynolds numbers accessible to DNS. More specifically, the experimental data presented here will be used as the foundation for a low Reynolds number database. The initial comparisons of DNS against the experimental data are expected to lead to more in depth investigations to further support and validate DNS computations.

To this end, experiments were conducted on four shock/turbulent boundary layer interactions corresponding to the DNS computation configurations currently under investigation as described in Section 1.1.3. In Mach 2.9 flow, a 24º compression corner and a 12º reflected shock interaction were studied at $Re_\theta = 2400$. In Mach 8 flow, an 8º compression corner and a 10º sharp fin were studied at $Re_\theta = 3500$. The compression corner and reflected shock interactions were expected to produce a nominally two-dimensional interaction, while the sharp fin was expected to be three-dimensional. The flow conditions were such that the flow was expected to separate in all cases. Measurements were made with mean pressure and temperature surveys, surface oil flow, surface pressure, and visualized using filtered Rayleigh scattering (FRS). The results of these studies will be used to validate the ability of DNS to compute mean velocity profiles, surface pressure, separation/reattachment, and statistics on large scale structures in the boundary layer.

The remainder of this chapter summarizes the relevant background information and previous investigations into compression corner, reflected shock and sharp fin interactions with a summary of the expected flowfields for the four experimental configurations. Chapter 2 describes the wind tunnel facilities, model descriptions, procedures and experimental techniques used in these investigations. Chapter 3 summarizes the results of the 24º compression corner and 12º reflected shock interactions at Mach 2.9. Chapter 4 summarizes the results of the 8º compression corner and 10º sharp fin at Mach 8. The final chapter summarizes the results and provides some insights for further work to complete a low Reynolds number experimental database.

1.2 The Compression Corner Interaction

The compression corner interaction is a simplified case of the types of interactions that occur over deflected control surfaces, engine intakes and wing/body junctions. The flowfield in a compression corner has been studied extensively by such authors as Settles et al (1979), Kuntz et al (1987), Smits and Muck (1987), Dolling and Murphy (1983), Ardonceau (1984), and Selig et al. (1987). This previous work covers a wide range of turning angles and Reynolds numbers, but the lowest Reynolds number reported from these studies is $Re_\theta \approx 23{,}000$ (Settles et al., 1978). The following provides a description of compression corner flows and highlights the results of previous studies.

A compression corner interaction occurs when supersonic flow along a flat plate is compressed by a wedge or ramp of angle α. In inviscid flow, a single oblique shock at angle β would be generated originating from the corner location and turn the flow by an angle α. This turning causes a step change in the pressure between the incoming flow and the flow over the wedge. Knowing the freestream Mach number and turning angle,

the downstream properties can be calculated using oblique shock relations at least for all cases where the shock is attached. The actual viscous flow picture is much more complicated. The pressure gradient imposed by the wedge can be sufficiently strong to cause the flow to separate at the corner location. The actual flow picture and the effect of the wedge angle are shown in Figure 1.2. These shadowgram images at Mach 2.9 at increasing wedge angles showed the effect of the wedge angle, hence shock strength. At 8º, the flow somewhat resembles the inviscid picture, with the flow attached and the shock originating at the corner location, except that the curvature of the shock results from Mach number gradient in the incoming in boundary layer. A greater upstream influence is seen in the 16º corner, where the shock begins to fan out into a series of compression waves in the boundary layer. The 16º turning at this Mach number is known as incipient separation (Settles et al, 1979) as the surface oil visualization revealed the first evidence of a separation line just upstream of the corner. The 20º and 24º wedge angles create a fully separated interaction with the upstream influence increasing with shock strength. The 24º case shows the reattachment compression waves merging with the separation shock generated by the separation bubble and reinforces it. The dual compression wave system is a clear indication of the presence of separation (Settles, 1976).

The mean surface pressure for various wedge angles (shock strengths) is shown in Figure 1.3 for flow at Mach 2.85. Unseparated flows are similar to the inviscid picture, with a sharp rise in pressure at the corner. Incipient separation at 16º shows a shift in the sharp pressure rise indicating the beginning of upstream influence. The pressure

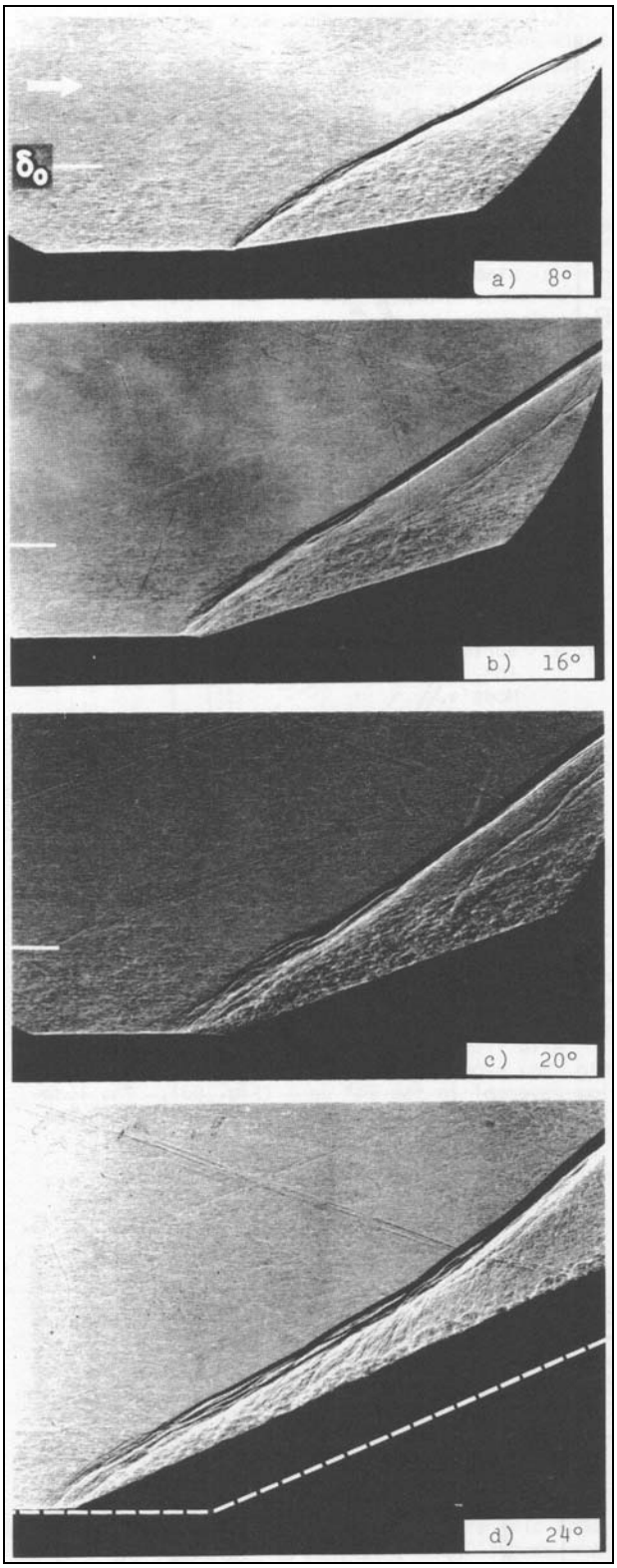

Figure 1.2: Shadowgram images of Mach 2.85 compression corner interactions at various wedge angles. From Settles et al (1976).

distributions for 20º and 24º indicate that in a region of separation, the wall pressure initially rises gradually through the unsteady motion of the separation shock (Selig et al., 1989). The mean pressure is the average of the undisturbed pressure upstream of the shock and the higher pressure behind the shock. A higher mean pressure corresponds to the shock being located upstream of that position for a greater amount of time than a station with a lower mean pressure. The wall pressure reaches a quasi-plateau in the fully separated region and then rises gradually again after the flow reattaches. Note in all cases that the compression and flow turning is not completed through the initial wave system, and the pressure rise continuing rather gradually many boundary layer thicknesses downstream of the corner indicating the presence of a complicated wave system downstream of the corner. In the 24º case of Settles et al (1978), the pressure did not reach the inviscid oblique-shock value by the end of the model, nearly 8δ downstream of the corner. The pressure distribution reveals the large upstream influence and large streamwise extent of the interaction.

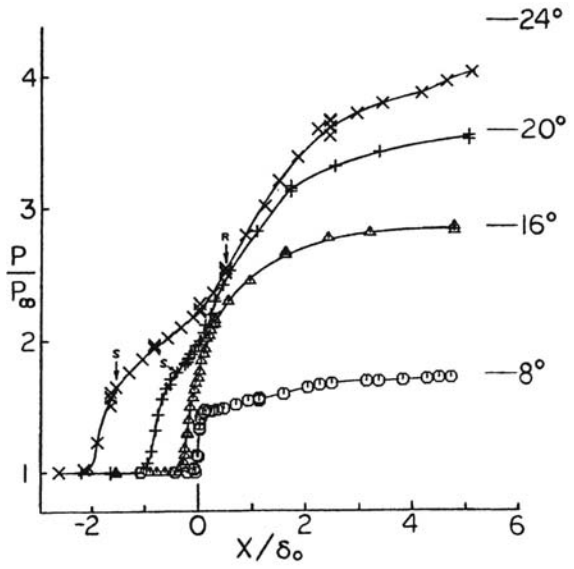

Figure 1.3: Surface pressure distributions on various compression corner interactions at Mach 2.85. From Settles et al. (1978).

The intensity of a shock/boundary layer interaction can also be characterized by its upstream influence, i.e. the upstream distance at which the shock presence is first felt (Delery and Marvin, 1986). Most often determined from inspection of the surface pressure distribution, the upstream influence is taken to be the streamwise distance from the corner, X_u, of an extrapolation to the wall of the quasi-linear pressure rise at separation (Settles and Bogdonoff, 1973; Roshko and Thomke, 1974; Hayakawa and Squire, 1982). The main parameters that influence the extent of the upstream influence are the upstream Mach number, Reynolds number, wedge angle (α) and thickness of the incoming boundary layer (Green, 1970). Scaling the upstream influence distance by the incoming boundary layer thickness (δ_0), it is generally agreed that for a fixed value of $Re_{\delta 0}$, the upstream influence increases with α for fixed Mach number and decreases when the Mach number increases at fixed α. There is controversy on the influence of Reynolds numbers. Experiments at low to moderate Reynolds number ($Re_{\delta 0} \leq 10^5$) have shown that the upstream influence increases with Reynolds number (Spaid and Frishett, 1972). However, experiments at high Reynolds numbers have shown that the upstream influence decreases with increasing Reynolds numbers (Settles et al, 1975; Roshko and Thomke, 1974). The experiments completed in this study at Mach 2.9, $Re_{\delta 0} \approx 3.5 \times 10^4$ may shed some light on this controversy.

The separation length, X_s, is another characteristic length describing the streamwise extent of the interaction. This is the distance from the corner to the point of separation, which can be found from many different methods, but is often found from surface oil flow visualization. The location of ridges of accumulation of the oil associated with the stagnation points of separation and reattachment are measured to determine the

separation length (Settles and Teng, 1982). The overall tendencies observed for the upstream influence length are valid for the separation length (Delery and Marvin, 1986).

The characteristic lengths discussed above are determined from time-averaged measurements. The instantaneous values vary constantly with time due to the highly unsteady motion of the separation shock. The upstream influence, as described above is the furthest point upstream of the corner where pressure fluctuations are large enough and frequent enough to cause a discernible increase in the mean wall pressure. The streamwise extent of the fluctuation is a function of the shock strength and is a significant fraction of the distance from the beginning of the interaction to the separation point. The frequency of the shock motion is an order of magnitude less than the characteristic frequency of the boundary layer U_e/δ, but shows no evidence of periodicity (Dolling and Murphy, 1983). The pressure distribution is therefore a superposition of the pressure fluctuations caused by unsteady shock motion on the mean pressure profile of the undisturbed boundary layer.

The variation of the velocity profile through the interaction reveals more about the mean structure of the boundary layer. Nine mean velocity profiles spanning a 24º compression corner interaction at Mach 2.9 are shown in Figure 1.4 from the work of Selig et al (1989). The incoming boundary layer is typical of an equilibrium turbulent boundary layer. The retardation of the flow is apparent at the point of separation. Wake-like shear layer profiles are seen in the profiles taken in the separated zone, with large regions of flow reversal. Reverse flow ends at the reattachment point, but the flow is still highly retarded. The profiles downstream of the corner show a rapid filling out towards a recovery to the equilibrium profile. This rapid change is caused by enhanced turbulent

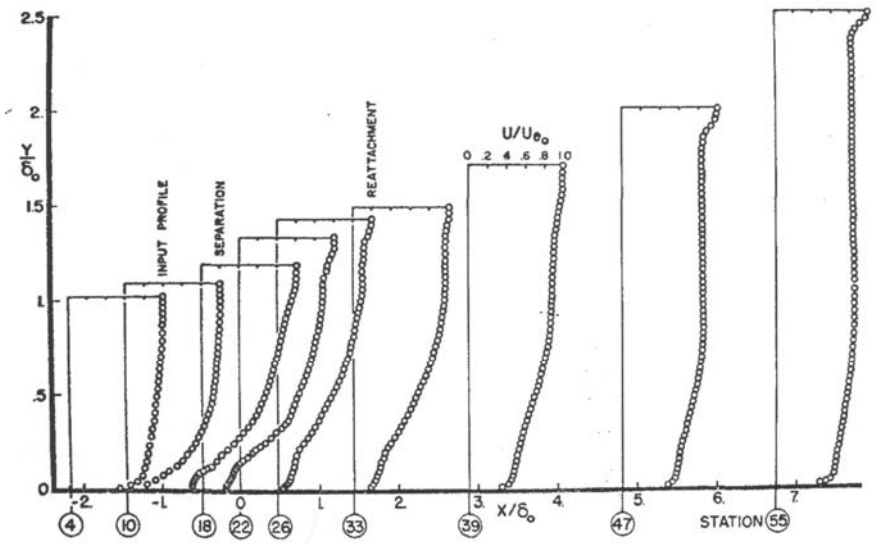

Figure 1.4: Velocity profiles through the separated 24° compression corner at Mach 2.85. From Settles et al (1978).

mixing due to the formation of large-scale eddies, or large turbulent scales (Kuntz et al, 1986). A close comparison of the far downstream and incoming profile reveals that the profile has a small wake component, indicating in the context of that experiment that the boundary layer takes at least 8δ downstream of the corner to recover to the equilibrium profile of the incoming boundary layer. Also of interest is the gradual decrease of the velocity at the edge of the boundary layer. This is indicative of the gradual pressure rise and flow turning shown in the surface pressure distribution.

Experiments carried out to study the turbulent flowfield revealed large non-uniform amplifications of turbulent intensities and stresses (Smits and Muck, 1987; Selig et al, 1989; Ardonceau, 1983; Kuntz et al, 1986). A detailed summary of the turbulent flowfield is beyond the scope of this thesis, but the references mentioned above provide insight to the effects of the compression corner interaction on the turbulent flowfield.

1.3 The Reflected Shock Interaction

The reflected shock interaction typically occurs in internal flows where shocks generated by disturbances near the leading edge of supersonic engine inlets impinge on the boundary layer of the opposite wall of the inlet. This type of interaction has not been as extensively investigated as the compression corner interaction because measurements are more difficult to obtain and they also tend to be three-dimensional showing effects of side walls. However, studies have shown that the characteristics of the interaction are very similar to the compression ramp interaction. An excellent review of reflected shock interactions is contained in Delery and Marvin (1986). The following summarizes the nature of the reflected shock interaction and highlights some previous work on the subject.

In experimental investigations, the shock is generated by a sharp leading edge flat plate inclined to the incoming flow or by a ramp mounted on the wall of a test section. The oblique shock originating from the sharp edge or ramp corner impinges on a flat wall or plate. The strength of the incident shock determines the nature of the interaction. For weak incident shocks, the interaction somewhat resembles the inviscid picture where the shock reflects off the surface of the flat plate. These weak interactions are shown schematically in Figure 1.5. The incident shock (C_1) progressively curves as it penetrates the boundary layer due to the Mach number gradient. The pressure rise due to the incident shock propagates upstream in the subsonic region where the thickened subsonic region generates outgoing compression waves that coalesce into the reflected shock (C_2). If the incident shock is strong enough, the boundary layer will separate leading to a flow picture that is complicated and much different than the inviscid flowfield.

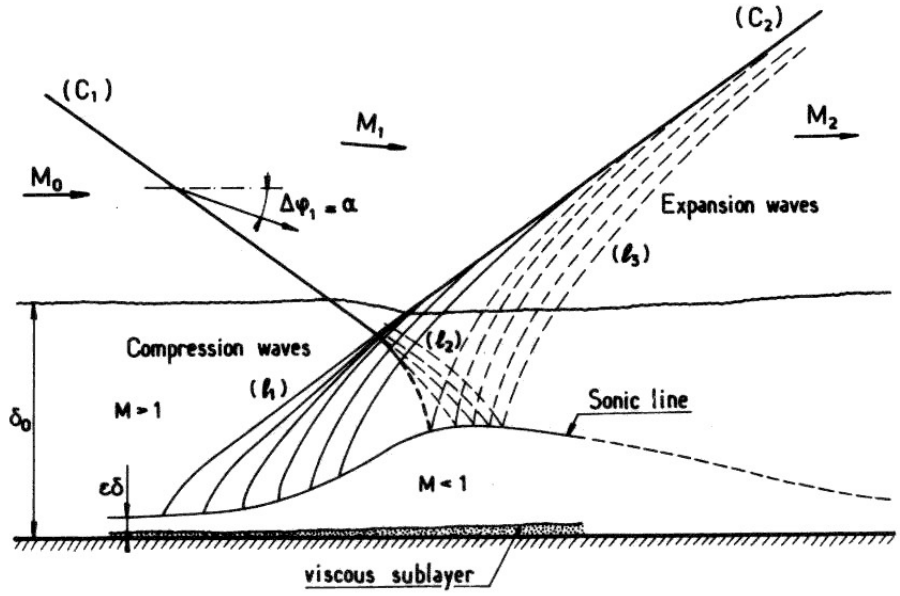

Figure 1.5: Schematic of an unseparated reflected shock interaction. From Delery and Marvin (1986).

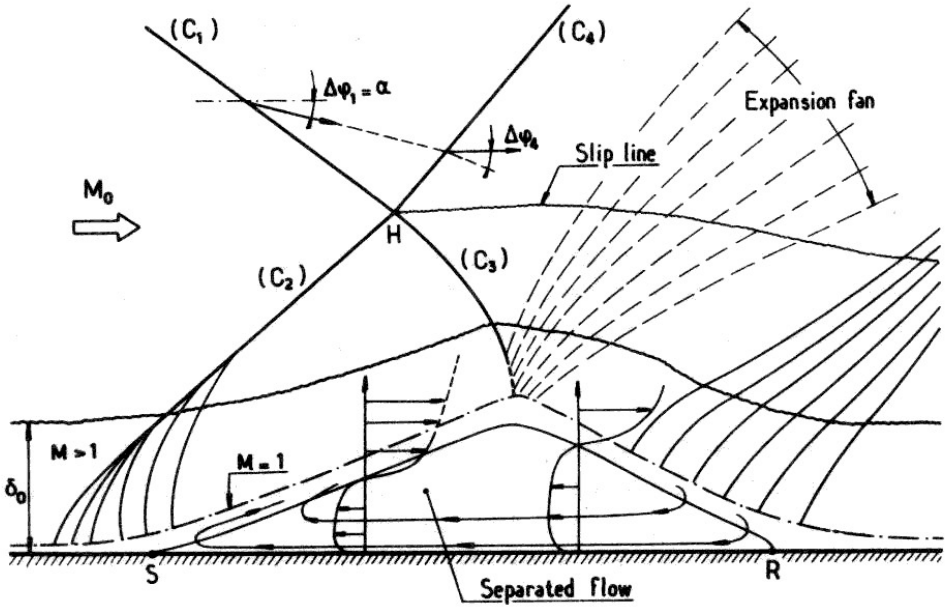

Figure 1.6: Schematic of a separated reflected shock interaction. From Delery and Marvin (1986).

A schematic representation of the separated flowfield is shown in Figure 1.6. The boundary layer separates at point S, well upstream of the location where the incident shock would meet the surface in inviscid flow. The compression at separation appears in the form of compression waves which coalesce to form the separation shock (C_2). The separated shock intersects the incident shock at point H which generates the refracted shocks C_3 and C_4. The refracted shock C_3 enters the boundary layer where it reflects off the separated region into an expansion fan. The fan continues to turn the flow towards the wall, which decreases the height of the separated region until the flow reattaches at point R. The resulting reattachment compression waves are a much more progressive wave system than the deflection at separation and may not be visible in flow visualization.

Green (1970) points out that the wave system produced in the reflected shock interaction is similar to the separated compression corner flow. In both cases, there is a strong outward turning of the flow at separation followed by an abrupt change in the flow direction relative to the wall direction. For the compression corner, the wall turns by the ramp angle α. In the reflected shock case, the flow is turned by the incident shock and expansion fan through the angles $(\Delta\varphi_1 + \Delta\varphi_3) \approx 2\alpha$. Therefore, a compression corner of angle 2α and incident shock of initial deflection α produces a similar series of compression interactions at separation and reattachment. If the overall pressure rise is the same, the surface pressure distributions may be nearly identical. The work of Shang et al (1976) reveals the similarities of the compression corner and reflected shock interactions where both cases were tested at Mach 2.96, $Re_{\delta 0} = 1 \times 10^7$ (Figure 1.8). The two flows are strikingly different in flow visualization but create a very similar surface pressure

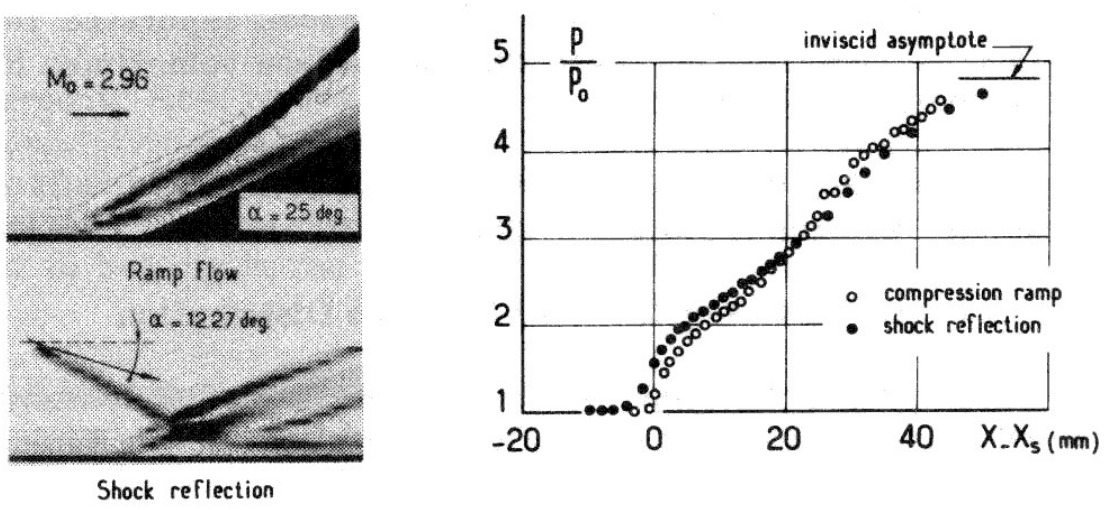

Figure 1.7: Comparison of the surface pressure distribution of the compression corner and reflected shock interactions. Images on left from density contours. From Shang et al (1976).

distribution if the total pressure rise is the same and the compression ramp angle is twice the initial turning angle of the reflected shock interaction.

The scaling of the upstream influence length and separation length show the same general tendencies described in Section 1.2 for the compression corner interaction (Delery and Marvin, 1986).

One major difference of the compression corner and reflected shock interactions is revealed in velocity profiles. For both cases, the velocity profiles show the retardation of the flow in the separated region and the wake-like properties downstream of the separation point as the profile recovers to equilibrium. However, the reflected shock interaction produces a much larger separation zone, with height on the order of the incoming boundary layer, as shown in Figure 1.6. The velocity profiles show much larger regions of flow reversal resulting in a significant increase in the boundary layer height as the boundary layer must flow over the separated region.

Three-dimensionality has been observed in this ideally two-dimensional interaction (Bourgoing and Reijasse, 2001; Doerffer and Szawba, 2004; Dussauge et al., 2005). Surface flow visualizations showed the presence of two vortices embedded in the separation zone which are symmetric with respect to the streamwise axis. This three-dimensional character is most likely the result of tunnel side-wall interactions in most experiments. Figure 1.8 shows the tornado-like vortices present in the separated region, where the height of the structure is only about half the boundary layer thickness. Curvature of the mean separation line and leading shock waves further suggested strong three-dimensionality of the reflected shock interaction

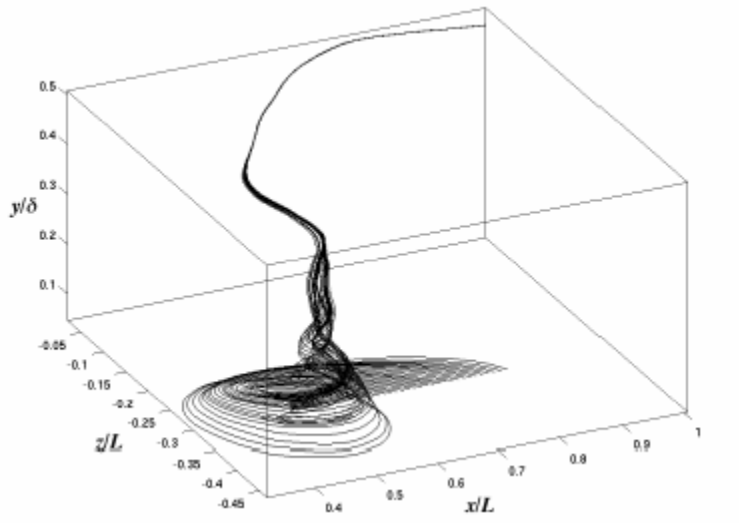

Figure 1.8: Vortex structure in the separated region of the reflected shock interaction. From Smits and Dussauge (2005).

1.4 The Sharp Fin Induced Interaction

One of the most commonly studied three-dimensional shock/turbulent boundary layer interaction is that generated by a sharp fin mounted at an angle of attack, α, mounted perpendicular to a flat surface or plate. This interaction, commonly referred to

as a sharp fin interaction, is a simplified version of the more complex interactions that occur in engine inlets and fin/body junctions. The majority of the work on these interactions lies in the supersonic range of Mach numbers from 2.5 to 5 (e.g., Dolling and Bogdonoff, 1981; Schmisseur and Dolling, 1992; Tran et al, 1985; Alvi and Settles, 1991; Settles and Lu, 1985; Knight et al, 1987). Studies conducted on interactions at hypersonic Mach numbers are much fewer in number (Knight et al, 1992; Law, 1975; Kussoy et al, 1991). This section provides an overview of the nature of the sharp fin interaction with the discussion based on the main body of available data at supersonic Mach numbers.

If the shock generator does not introduce a dimensional quantity (i.e. its height is much larger than δ_0 and its leading edge has negligible thickness), then the only parameter describing the interaction is the angle of attack, α. Other parameters in the problem deal exclusively with the incoming flow, including Re, M_∞, and δ_0. The incoming boundary layer thickness is the only parameter that introduces a dimensional quantity, suggesting the interaction will produce some characteristic length scale whereas the rest of the flow is expected to be dimensionless (Settles and Dolling, 1991).

Previous investigations have found that the interaction created by the sharp fin grows with distance from the leading edge. This growth has been observed to be conical in nature, except for a small region near the fin leading edge. Parametric studies by Zheltovodov (1997) have shown the conical character of these interactions to be true for a wide range of fin angles and Mach numbers. This *quasiconical* nature is the most notable feature of the sharp fin interaction. As a result, the appropriate coordinate system when studying this interaction is a spherical/polar coordinate system with the origin centered at

a point near the leading edge, as shown in Figure 1.9. Pertinent features can then be referenced to angles relative to the freestream.

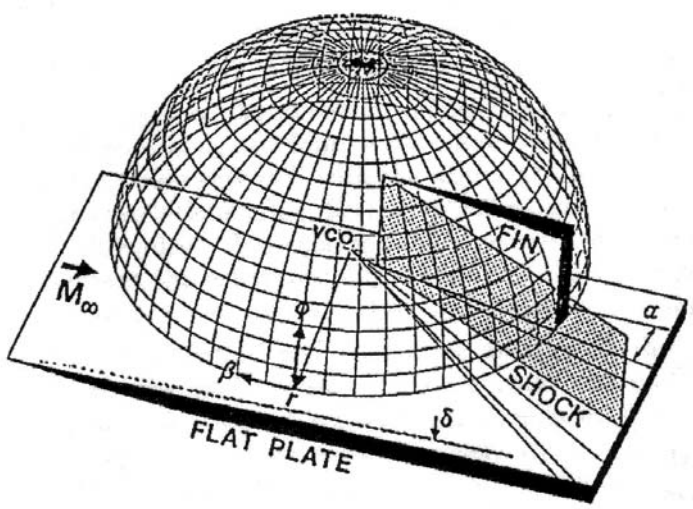

Figure 1.9: Spherical/polar coordinate system appropriate to sharp fin interactions. From Settles and Dolling (1991).

As with the compression corner and reflected shock interactions, the boundary layer in a sharp fin interaction may separate due to the pressure gradient imposed by the inviscid oblique shock attached to the leading edge of the fin. The evolution of separation in sharp fin interactions is a gradual process depending on the shock strength, which depends on the Mach number and fin angle. A more detailed discussion of the onset of separation is beyond the current scope, and the remainder of this discussion will concentrate on fully separated interactions which occur for sufficiently strong shock strengths.

Figure 1.10 illustrates the pertinent features of the interaction footprint along with the appropriate nomenclature. The various flow features highlighted in Figure 1.10 are obtained from surface oil flow visualization. The line where the incoming flow first feels the presence of the interaction is known as the upstream influence line, β_U. This line is seen in surface flow visualization as the line along which the surface stream lines first

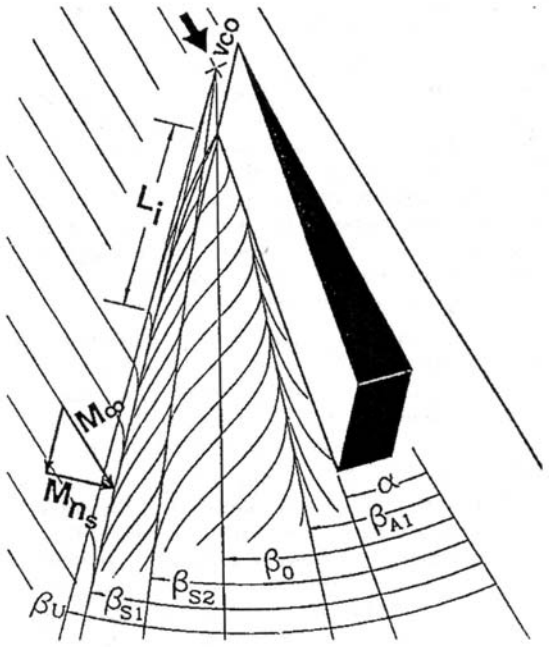

Figure 1.10: Schematic of the interaction footprint from surface oil flow visualization with appropriate nomenclature. From Settles and Dolling (1991).

diverge from the freestream direction. This point correlates well to the point where the mean pressure first increases (Schmisseur and Dolling, 1992). The primary separation line, β_{S1}, is marked by the convergence of surface streamlines from both the incoming flow and the streamlines just inside the separated zone (also known as a "line of convergence" in topology).

The primary attachment line, β_{A1}, marks the "line of convergence" where the flow reattaches after having left the flat plate at the separation line. In between the separation and reattachment lines, the flow forms a spiraling, helical separation vortex. A secondary separation may occur, but the secondary separation line, β_{S2}, is rarely seen in surface flow visualizations and little is known about the nature of secondary separation. The trace of the inviscid shock line, β_0, does not show up in surface oil flow visualization but is commonly drawn in for reference. In Figure 1.10, the lines converge to a common vertex, known as the virtual conical origin (VCO). The VCO lies at the center of the

spherical/polar coordinate system and is upstream of the sharp fin leading edge due to the inception region.

The region in the near vicinity of the sharp leading edge is known as the inception region. In this area, significant viscous effects cause there to exist a certain distance before the flowfield becomes quasiconical, as seen in Figure 1.10. As discussed above, this distance is the single characteristic length imposed by the incoming flow conditions and is known as the *inception length*, L_i. The inception length, when non-dimensionalized by the incoming boundary layer height, is the natural parameter describing sharp fin interactions (Settles and Dolling, 1991). Through an order of magnitude analysis of the governing equations, Inger (1987) discovered the nondimensional inception length, L_i/δ_0, to be related to the strength of the interaction represented by the inviscid shock angle, β_0. His finding that $L_i/\delta_0 \approx \cot(\beta_0)$ was in good agreement with experiment of sharp fin interactions (Inger, 1987).

The strength of the interaction is measured by the Mach number normal to the inviscid shock, M_n. When dealing with the spherical coordinate system discussed above, the streamlines and features of the flow may be simplified to two dimensions by replacing the surface of the sphere with a plane tangent to the sphere and normal to the inviscid shock (Settles and Dolling, 1991). Thus, the pertinent Mach number is that normal to the inviscid shock. This combines the effects of M_∞ and α, since an increase in M_∞ at fixed α or an increase of α at fixed M_∞ will produce an increase in M_n.

Lu, Settles and Horstman (1990) examined the effect of Mach number over the range $2.5 \leq M_\infty \leq 4.0$. They found the Mach effect to be accounted for by referencing the inviscid shock (β_0) and the upstream influence (β_U) to the incoming Mach angle (μ_∞).

The behavior of these angles with changing fin angle reflects the effect of Mach number and was found from a least squares regression of the data in the Mach range described above:

$$\Delta\beta_U = 2.2\Delta\beta_0 - 0.027\Delta\beta_0^2 \tag{1.4}$$

where $\Delta\beta_U = (\beta_U - \mu_\infty)$ is the reduced upstream influence and $\Delta\beta_0 = (\beta_0 - \mu_\infty)$ is the reduced shock strength. Schmisseur and Dolling (1992) reported that this relationship slightly underpredicts the behavior of the upstream influence in experiments at Mach 5. Data at hypersonic Mach numbers is scarce and the capability of this relationship to make accurate predictions at the higher Mach numbers is unknown. Equation 1.4 is expected to fail at very strong interactions, where it would predict the reduced upstream influence to be less than the reduced inviscid shock, a physical impossibility. It is possible that in the strongest interactions, the upstream influence line will collapse to the inviscid shock trace

The boundary layer thickness, δ, varies along the swept interaction line. There were early concerns that the flowfield scaling would depend on the local boundary layer thickness and hence the Reynolds numbers. Experiments by Dolling et al (1977) concluded that only the Reynolds number and boundary layer thickness at the leading edge play a role in defining the flowfield scaling of the sharp fin interaction, which was shown above to have only one parameter, the inception length. Application of Reynolds numbers scaling laws for general swept interactions (Dolling and McClure, 1983) to the single scaling parameter in sharp fin interactions (Dolling and McClure, 1983) yields an expression for the effect of changes in Reynolds number:

$$\frac{L_i/\delta_0}{M_n} \propto \mathrm{Re}_\delta^{-1/3} \tag{1.5}$$

Since the inception length is the only dimensional parameter, the effect of Reynolds number is to expand or shrink the scale of the footprint without geometric distortion, leaving the conical symmetry region invariant. Thick boundary layers with relatively low Reynolds numbers can produce a large dimensional inception length and investigators must be wary of the relationship shown in Equation 1.5 so that experiments and computations extend far enough to reach beyond the inception length into the conical flow region.

Moving beyond the interpretation of the surface footprint of the sharp fin interaction, Alvi and Settles (1991) provided a physical model the flowfield structure for a range of interaction strengths at freestream Mach numbers between 3 and 4. The physical model developed from conical shadowgraph, conical holographic interferogram, and Planar Laser Scattering (PLS) images are shown in Figure 1.11 in conical symmetry coordinates with the flow direction normal to the inviscid shock from right to left. The views presented here are planes normal to a surface of the spherical coordinate system, as shown in Figure 1.12 for clarification. The inviscid shock is seen to split into a lambda (λ) shape where the upstream leg is the separation shock that extends to the surface at the primary separation line. The separated shock deflects the flow away from the plate until the rear leg of the λ redirects it back down. The separated boundary layer rolls up into a tight vortex and as clearly shown in Figure 1.11, the entire boundary layer separates and is rolled up into the vortex. Behind the separation bubble, the flow impinges on the surface at the reattachment line through a system of Prandtl-Meyer expansions and compression waves. The secondary separation (S_2) is seen in Figure 1.11 as a bulge in the reverse flow near the surface.

Of critical importance to the understanding of the conical symmetry of the interaction is that these flowfield maps were taken at various radial distances from the VCO. The results reinforce the notion that the structure of sharp fin interactions in spherical polar coordinates is independent of the radial distance from the VCO outside the inception region (Alvi and Settles (1991). Kussoy et al (1991) studied a 15º sharp fin at Mach 8.2 and found a similar flowfield structure except the λ shock was completely embedded in the incoming boundary layer, a much different phenomenon then found by Alvi and Settles (1991).

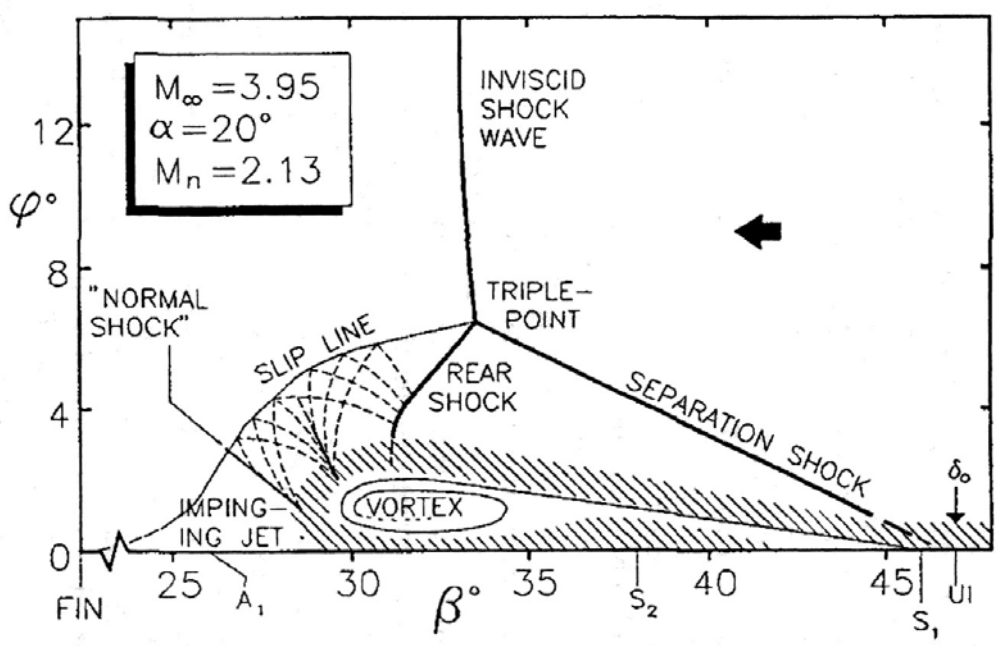

Figure 1.11: Flowfield structure map for Mach 4, 20º sharp fin interaction in spherical polar coordinates. From Alvi and Settles (1991).

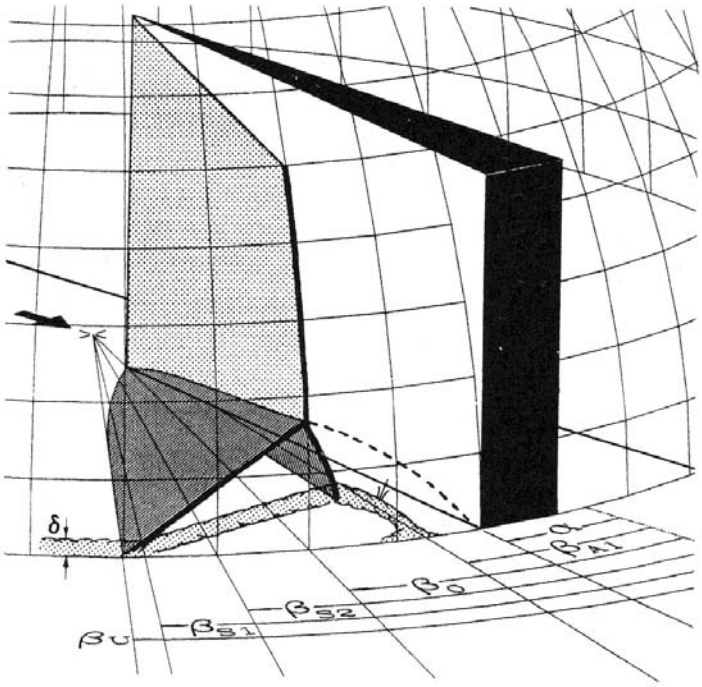

Figure 1.12: Projection of the quasiconical interaction onto spherical coordinate surface. From Settles (1993).

As was the case in the two-dimensional compression corner and reflected shock interaction, the sharp fin interaction has been shown to be highly unsteady (Tran et al, 1985). Rayleigh scattering images of the shock structure of a Mach 3 20º sharp fin interaction revealed significant movement of both the separation point and the triple point of the λ shock system (Smith et al, 1991). The mean and fluctuating pressure signal was shown to scale in conical coordinates (Gibson and Dolling, 1991; Garg and Settles, 1993). The pressure fluctuations increased with fin angle and were highly intermittent near separation.

1.5 Description of Expected Flows

Four flow configurations were examined in this study, including a 24º compression corner and 12º reflected shock at Mach 2.9 and an 8º compression corner and 10º sharp fin interaction at Mach 8. The 24º compression corner was studied extensively at Mach 2.9 by Settles (1975) at high Reynolds number, $Re_\theta \approx 67{,}000$. Settles' experiments revealed this configuration to create a large separated flowfield. It was expected that the 24º compression corner investigated here ($Re_\theta = 2400$) to produce a similar flowfield from which data could be extracted to test the validity of DNS computations. As discussed above, the compression corner and reflected shock interactions are similar in strength when the initial turning angle of the reflected shock is half the compression corner angle, α, and the overall pressure rise is the same. Therefore, the 12º shock generator was selected and subjected to the same test conditions as the compression corner interaction ($Re_\theta = 2400$). These configurations were examined visually with Filtered Rayleigh Scattering (FRS) and surface oil flow visualizations and quantitative measurements of mean surface pressure, Pitot pressure and total temperature distributions were made.

The strength of the Mach 8 compression corner interaction was desired to be similar to that of the 24º compression corner at Mach 2.9. Therefore, the 8º wedge was selected and was expected to produce a shock of similar strength. Separation of the boundary layer was therefore expected, although little information on hypersonic boundary layer separation was available to provide conclusive evidence of this prediction. The 10º sharp fin at Mach 8 was chosen in order to create the three-dimensional quasi-conical interaction discussed above. Kussoy et al (1991) found a 10º

sharp fin at Mach 8.2 to separate, so the configuration studied here was expected to behave similarly. These two flow configurations at Mach 8 were examined visually using FRS imaging and surface oil flow visualizations, providing both qualitative and quantitative information.

Chapter 2 Experimental Methods

2.1 Supersonic Wind Tunnel Facility

2.1.1 General Overview

Experiments at Mach 2.9 were conducted in the Princeton University Gas Dynamics Laboratory Low Turbulence Variable Geometry (LTVG) supersonic wind tunnel with a working section nominally 8" x 8" (200mm x 200mm). This facility is a blowdown wind tunnel using air as the working fluid. A schematic of the working section of the wind tunnel is shown in Figure 2.1. The stagnation pressure for this tunnel ranges from 5 psia to over 100 psia. In order to match the Reynolds number attainable by the DNS computations, the stagnation pressure in the experiments conducted here was 10.6 psia, requiring the use of an ejector system to give a back pressure of approximately 0.3 psia. This condition provided a freestream unit Reynolds number (Re/m) of 5.6 x 10^6.

The tunnel air is supplied by four 18 m^3 high-pressure storage tanks. The air is compressed by eight Ingersoll-Rand 3-stage air-cooled compressors. Water vapor, dust and oil residue from the compressors are removed by filters and driers before the air enters the storage tanks. The storage tanks, when filled to the working pressure of 2400 psi, provided one to two minutes of run time in the LTVG. Typically, the compressors must pump for 24 hours in order to bring the storage tanks back up to working pressure. The storage air is connected to the settling chamber through a Fisher Controls pneumatic valve. The flow passes through a series of honeycombs and mesh screens to reduce the freestream turbulence. Pressure and temperature measurements are made in the settling

chamber before the air enters a two-dimensional nozzle where the flow is accelerated to a nominal Mach number of 2.9. The test section is comprised of a 20 cm x 20 cm cross sectional area 92 cm in length. A flush mounted window allows optical access from the ceiling of the test section. A circular window of 20 cm diameter mounted in the test section sidewall provides optical access from the side. A diagram of the LTVG wind tunnel is shown in Figure 2.1. There is no second throat and the flow enters the diffuser immediately downstream of the test section.

The diffuser is connected to the ejector system that provides the low backpressure required to start and maintain supersonic flow in the test section. The two-stage ejector system manufactured by Fox Valve Development Corporation provides a zero flow backpressure of approximately 0.35 psia when both ejectors are in operation. The ejectors draw air from the same high-pressure air as the tunnel, but require much larger mass flow. The ejectors may be run in single or dual ejector mode. The LTVG requires both ejectors when operating at the stagnation pressure used in these experiments to maintain the necessary backpressure for Mach 2.9 operation. The large mass flow requirements limit the run times to 1-2 minutes.

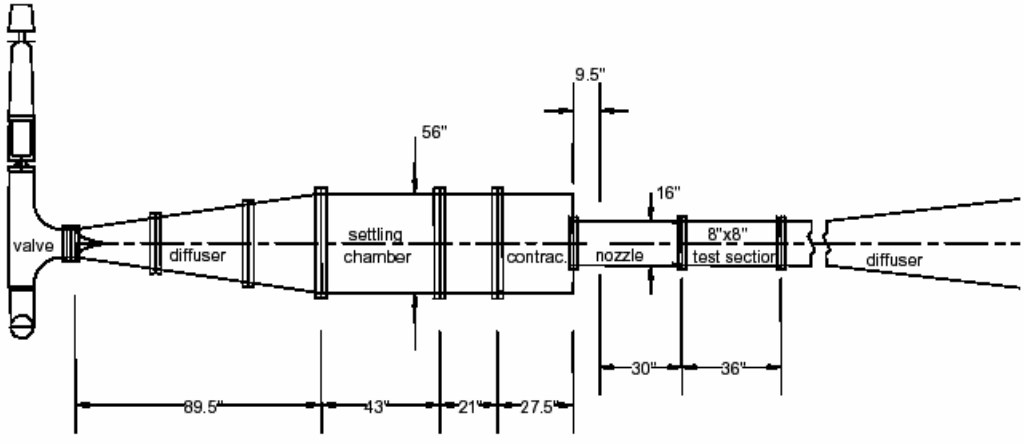

Figure 2.1: Schematic drawing of the LTVG supersonic wind tunnel.

2.1.2 Mach 2.9 Models

All experiments were performed on a brass flat plate. Constructed of 360 free-cutting brass, the plate spanned the entire width of the tunnel. The plate was mounted three inches above the tunnel floor with the leading edge at the nozzle exit. A cylindrical wire trip, 1.65 mm in diameter, was mounted 7 cm from the leading edge to fix the transition point. This diameter was chosen based on the estimates given by Pope and Goin (1978). The plate was built with a single row of pressure taps along the centerline for surface pressure measurements.

The two-dimensional compression corner interaction was created using a 24º wedge. Constructed of 360 free-cutting brass, the wedge was bolted to the flat plate with the leading edge 335 mm downstream of the flat plate leading edge. To minimize interference effects due to the tunnel wall boundary layer, the model did not span the entire width of the test section and sharp-edged fences were used on either side of the model as shown in Figure 2.2. In order to gain optical access during the Filtered Rayleigh Scattering experiments (see Chapter 3), one fence was removed. The wedge was fully pressure tapped along the streamwise centerline with 3 mm spacing. The pressure tap tubes exited the tunnel through a small access hole in the sidewall of the test section.

The nominally two-dimensional reflected shock interaction was created using a 12º wedge of 360 free-cutting brass mounted on the tunnel ceiling. Aerodynamic fences were attached on the sides of the wedge in the same fashion as the 24º wedge. The model is shown as mounted in the test section in Figure 2.3.

Figure 2.2: 24º compression corner as mounted on flat plate for Mach 2.9 experiments. One aerodynamic fence has been removed to allow optical access for FRS flow visualization.

Figure 2.3: 12º reflected shock generator mounted in the ceiling of the test section with aerodynamic fences on both sides of the ramp for experiments at Mach 2.9.

2.1.3 Data Acquisition and Instrumentation

Boundary Layer Surveys

Measurements of Pitot pressure, static pressure and total temperature on the flat plate were taken to characterize the incoming boundary layer. A probe assembly with both a Pitot pressure and total temperature probe was used in order to simultaneously capture Pitot pressure profiles and total temperature profiles. The Pitot probe was a 2 mm wide flattened tip with a 0.3 mm opening. Time response was ruled more important than spatial resolution in the decision to use this probe since the tunnel run time is limited. The total temperature probe was an unsheathed bare-wire K-type thermocouple that extended 2mm inches from its sheath. The extension served to minimize conduction effects from the ceramic binder that sealed the thermocouple to the probe. A complete calibration of the total temperature probe was not undertaken; instead the recovery factor was established from a quasi-calibration in the freestream flow outside the boundary layer resulting in a typical recovery factor of 0.87. The static pressure at the location of each boundary layer profile was derived from a static pressure port in the flat plate just upstream of the probe location to avoid the bow shock created by the probe.

The probe was mounted on a traversing system rigidly bolted to the ceiling of the test section as shown in Figure 2.4. Access to the test section was possible through a ceiling plug with lubricated rubber gaskets to prevent leakage. The traverse was mounted on a fine threaded steel rod driven by a computer controlled stepper motor. A linear potentiometer calibrated against a dial gauge was used to measure the vertical position.

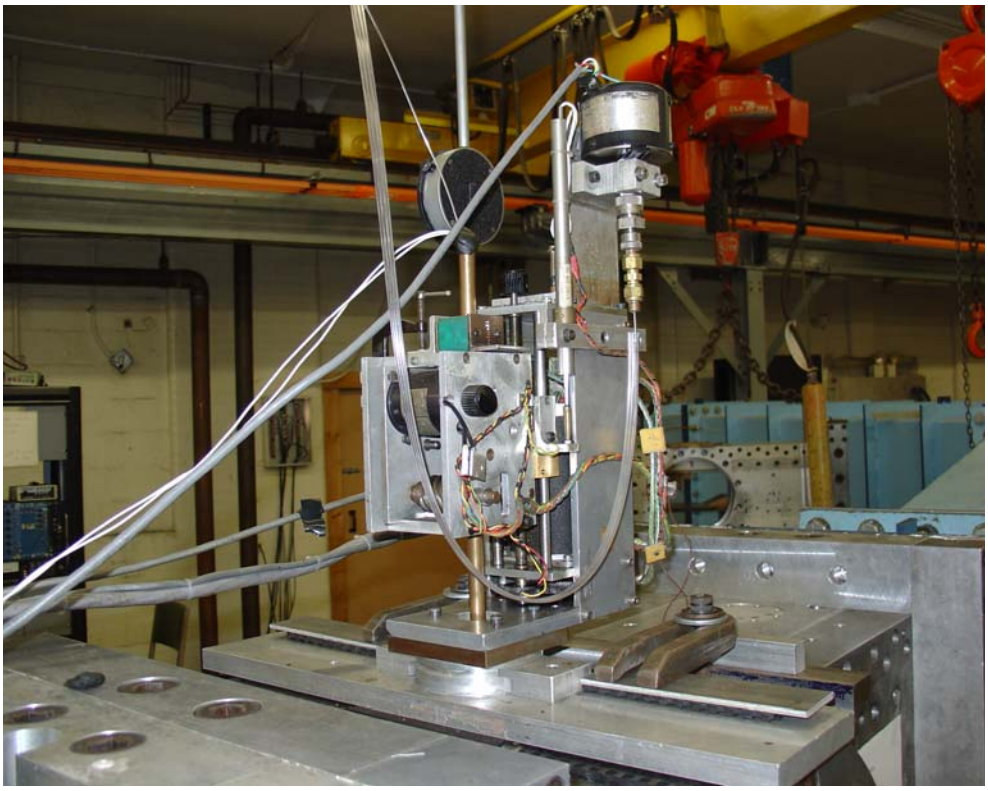

Figure 2.4: Pitot and total temperature probe drive assembly mounted through the ceiling of the test section for experiments at Mach 2.9.

Surface Pressure Measurement

The flat plate was instrumented with a single streamwise row of 23 pressure taps made from 0.065" outer diameter stainless steel tubing. The tubing was routed through the tunnel floor through a diamond shaped support under the flat plate where they were connected to a 48 port Model 48J4-2141 Scanivalve via 6 inches of rubber tubing. The response time of the surface pressure measurement system was determined by sealing the pressure tap holes and drawing the system down to vacuum and then abruptly opening the holes to atmospheric pressure. The time constant, defined as the time required to reach 67% of the final value, was found to be 400 ms. Therefore, a delay of 1.2 seconds was required between measurements of successive pressure taps. The pressure was measured

using a 1000 torr (19.6 psia) MKS Baratron absolute pressure transducer. The transducer voltage was scanned over a period of one second and averaged to determine the mean pressure at each tap location.

Surface Flow Visualization

The surface streamline patterns were visualized using a mixture of Dow Corning 200 silicon fluid and graphite particles. The graphite particles used ranged in size from minute particles to small granules on the order of 0.001 inch in diameter. Due to the low Reynolds numbers investigated here, the mixture was kept thin by combining the silicone and graphite particles in a ratio of about six parts to one. This mixture was applied in a pattern of equally spaced dots spanning the breadth of the expected interaction region. In the case of the compression corner, the mixture was applied in discrete dots to the surface of the ramp. So long as the tunnel was started shortly after application, the dots did not move down the ramp prior to the tunnel start.

Upon starting the tunnel, the mixture streamed down the flat plate and coated the surface evenly. Flow separation was indicated by the presence of an accumulation of graphite particles at the convergence of forward and reverse surface shear forces. Within about twenty seconds, the mixture flowed through the interaction region revealing surface shear stress patterns. In order to capture the development of the surface flow over the course of the run, a Canon Elura Progressive Scan CCD Camcorder was used to record the run to video in real time. Still images from the video were digitized. Using the static pressure ports as a physical reference, direct measurements of the separation and reattachment lines were made from the surface flow still images.

Data Acquisition

To obtain boundary layer profiles, three basic quantities were measured: pressure, temperature and distance from the surface of the model. The stagnation pressure was monitored using a Pace 50 psig transducer referenced to atmosphere. Pitot pressure measurements were made using a 1000 torr (19.6 psia) MKS Baratron transducer. This same transducer was also used to measure the surface pressure distributions on all models as well. A MKS Baratron 100 torr (1.96 psia) transducer was used to monitor surface pressures during boundary layer profiles and Filtered Rayleigh Scattering. All pressure transducers were calibrated against precision Wallace and Tiernan absolute pressure gauges using a precision voltmeter.

Temperatures in the stagnation chamber and total temperature profiles were measured using Omega K-type chromel-alumel thermocouples referenced to an Omega Ice Point Cell. The signals were sent through an amplifier calibrated against a millivolt source.

The distances required for boundary layer profiles were measured using an Infinitron linear potentiometer. Prior to each survey, the potentiometer was calibrated against a dial gauge to ± 0.001".

The data acquisition system is controlled by a Dell desktop computer operating Windows 98. The program used for data input and control was National Instruments Labview Version 5.1. The physical connection is made by a National Instruments MIE-60 series data acquisition board. Transducer and thermocouple outputs are read on separate analog input connections with an input range of +/- 10 volts. The outputs are then converted to physical units in the Labview program written by the author using the

calibration coefficients. Control signals to the boundary layer probe traversing system and Scanivalve system were provided using digital output channels. The stepper motor was given a square wave control signal with the required number of steps to reach the desired survey height. The Scanivalve required a single 5 volt pulse to move one step.

During a typical boundary layer survey, simultaneous measurements of tunnel stagnation pressure, total pressure and wall pressure were made along with the survey measurements. A delay of one second was found to be sufficient for equilibration of the pressure transducers between readings. A total of 1000 scans of voltage signal were made at a rate of 1000 scans a second for each measurement reading and averaged. All data inputs were written to a spreadsheet file for further analysis.

Run Procedures

The experiments completed in the LTVG wind tunnel at M = 2.9 were done at a nominal stagnation pressures of P_0 = 10.6 psia. The total temperature was determined by the total temperature in the air storage facility. The total temperature in the tanks varied little with a value of T_0 = 293 K ± 3 K over the course of all the runs. The beginning of each run began with the starting of the dual ejector system and the pressure in the entire system was drawn down to approximately 0.35 psia. At this point the tunnel was started. The pneumatic valve required about five seconds in order to stabilize the pressure in the stagnation chamber. When the stagnation chamber had settled, data acquisition began. Actual run conditions were within 5% of nominal values and varied less than 3% during the course of a run for both P_0 and T_0.

2.2 Hypersonic Wind Tunnel Facility

2.2.1 General Overview

The facility used to complete the Mach 8 experiments was the Princeton University Gas Dynamics Laboratory Hypersonic Boundary Layer Facility (HyperBLAF), using air as the working fluid with a nominal test section diameter of 225 cm (9”). A schematic of the working sections of the tunnel are shown in Figure 2.5. Stagnation pressures range from 500 psi to 1500 psi. The wind tunnel is described in detail by Baumgartner (1997).

A brief description of the tunnel is offered here. Air is supplied by the same compressors and storage tanks as described above for the LTVG wind tunnel. From the storage tanks, the air passes through a Kay and MacDonald Model FD3ccXF Type 3 dome loaded-regulator valve. This valve in conjunction with the control system, regulates the supply air from 500 to 1500 psi.

The heater heats the air to the desired stagnation temperature of 750 K as it passes through 185 m (280ft) of 6.35 cm (2.5”) diameter stainless steel pipe wound into a helical coil. The pipes are resistively heated by a set of transformers that step the three-phase 480 V supply to approximately 20 volts, which is rectified by passing the low voltage, high current, three-phase power through a diode bank. Typically, the heater must run for 8 hours in order for the coil to reach a working temperature of 810 K. During the course of a run, the heater is cooled by the passing supply air. Therefore, the working temperature of the coil is set higher than the desired stagnation chamber to compensate for this effect.

From the heater, the air passes into the 15.2 cm (6”) diameter, 45.7 cm (18”) long stagnation chamber, where measurements are made of pressure and temperature. The

velocity in the stagnation chamber is approximately 5 m/s (16.4 ft/s). The air passes into the axisymmetric nozzle with a contraction length of 20 cm (8”) and throat diameter of 15 mm (0.5934”). The nozzle downstream of the throat is based on a nozzle design in use at the Aircraft Division of Israeli Aircraft Industries. From throat to exit, the nozzle measures 119 cm (47”) and the exit diameter is 22.9 cm (9.0”).

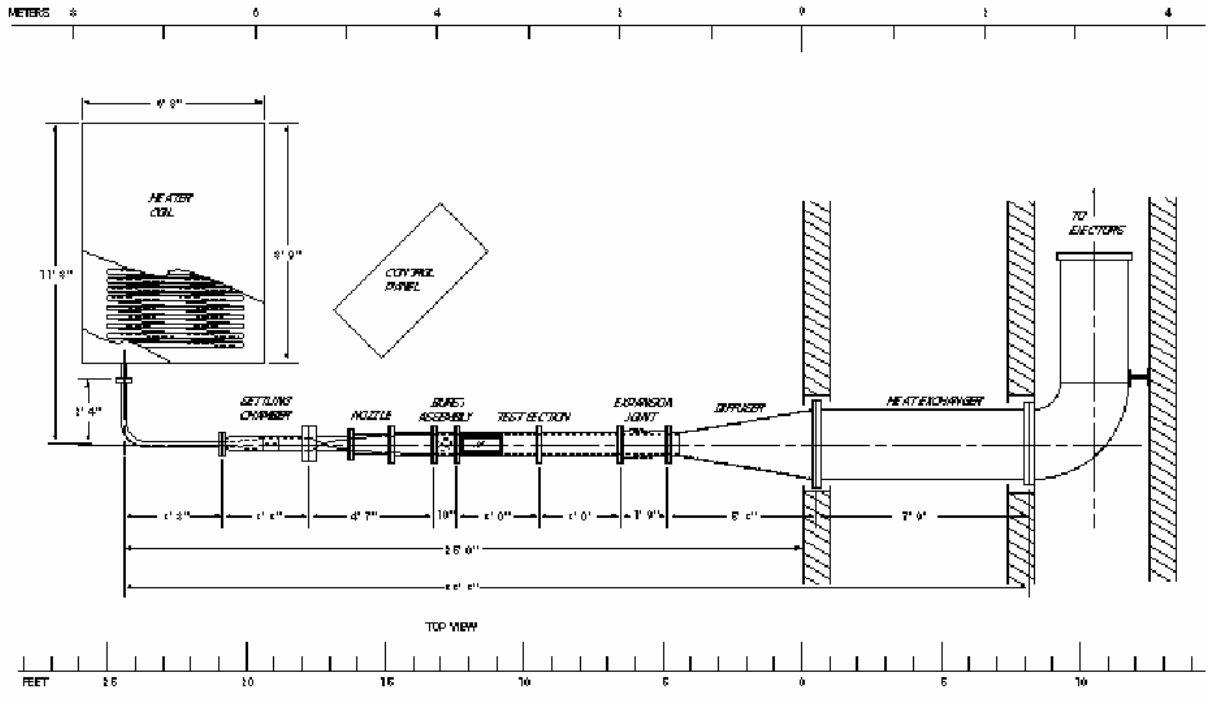

Figure 2.5: Schematic of the HyperBLAF wind tunnel. Inlet control valve and ejector system are not shown.

The test section, which will be described in the next section, is mounted directly downstream of the nozzle. Following the test section is a 26.7 cm (10.5”) burst assembly which feeds into a 10º half-angle diffuser where the flow is recompressed to subsonic flow through a series of shocks. The flow is cooled by water injection, and then passes through the ejector system which was described previously in the description of the Mach

2.9 experiments. The stagnation pressure was fixed at 1000 psi and required the use of only one ejector during these experiments. This allowed for approximately 2-3 minutes of run time for each experiment.

2.2.2 Test Section and Flow Properties

The test section is made up of two 91.4 cm (3') long, 22.9 cm (9") inside diameter stainless steel sections. One section is fitted with four orthogonal window cavities. The cavities are 12.7 cm (5") x 20.6 cm (16") rectangular sections, beginning 8.9 cm (3.5") from the beginning of the pipe. The windows are recessed 3.8 cm (1.5") from the walls of the test section. The models are mounted in the test section on a support which is fastened to a solid stainless steel window plate that bolts to the bottom window cavity. The top and side window cavities were used for optical access to the test section. The actual windows are mounted into stainless steel window plates that fit over the window cavity. The windows are 22.5 cm x 13.7 cm x 1.27 cm quartz windows. In previous experiments in this facility (Etz, 1997), the window cavities were found to cause disturbances that were detrimental to the starting of the tunnel. Ramps were installed at the end of the window plates to help alleviate this problem.

The flow in the test section has been characterized by Baumgartner (1997) and Magruder (1997). The Mach number is 8.0 ± 0.1 over 80% of the working section. Readers are referred to the work of these authors for a specific description of property variations in the test section. A summary of the mean test conditions for this study is shown in Table 2.1.

P_0 (psia)	T_0 (K)	T_w (K)	$T_{aw} - T_w$ (K)	T_w/T_{aw}	M_∞
979 ± 1.5%	780 ± 1.3%	518 ± 2.0%	185 ± 2.0%	0.74	8.0 ± 0.1

Table 2.1: Mean run conditions. The standard deviations demonstrate the repeatability of the experimental conditions.

2.2.3 Mach 8 Models

The incoming boundary layer developed on a flat plate 15.2 cm wide, 47.6 cm long, and 1.2 cm thick constructed from 360 free-cutting brass. The construction and choice of material was described in detail by Etz (1998), who designed and built the flat plate. It was supported by a support with a diamond-shaped cross section bolted to the solid stainless steel window plate which was attached to the bottom window opening in the test section. This orientation placed the centerline of the surface of flat plate on the centerline of the test section. Preliminary surveys on the flat plate showed a transitional to marginally turbulent boundary layer at the survey location. In order to ensure a turbulent boundary layer, a two-dimensional cylindrical tripping device was attached 5.8 cm downstream of the leading edge, measuring 2.4 mm in diameter or approximately 20 times the viscous length scale (on the order of 100 μm) at that location. The determination of the proper trip size and location was described in detail by Etz (1998).

The 8º compression corner measured 15.2 cm wide and 17.6 cm long and was mounted so the leading edge of the corner was 30 cm from the leading edge of the plate. The face of the compression ramp was 11.5 cm long to allow access to a flow approximately equal to 10δ downstream of the corner. The model height was limited to eliminate any chance of tunnel blockage issues. The 8º compression ramp is shown in Figure 2.6 as mounted on the flat plate. A piece of the ramp leading edge was broken off

during the machining of the compression corner, as seen in Figure 2.6. This was filled in with epoxy to minimized disturbances. All measurements were taken well away from the ding in the leading edge of the ramp.

The 10º sharp fin was constructed from 360 free-cutting brass and mounted to the aft end of the flat plate as shown in Figure 2.7. The dimensions of the sharp fin, shown in Figure 2.8, were chosen based on the location of existing mounting holes and the nature of the expected interaction. Due to the high Mach number, the shock generated by the sharp fin was expected to be highly swept, limiting the available space between the interaction and disturbances caused by the model's various geometries. Tunnel blockage was also a concern, so the overall size of the model was limited. The final design of the model maximized the available area of the interaction to be analyzed while avoiding tunnel blockage. The design also made use of existing mounting holes used for the 8º compression corner. Silicon sealant was applied to the bottom of the sharp fin model to prevent leakage underneath the model.

Figure 2.6: 8º compression corner as mounted on the flat plate for experiments at Mach 8. The model was painted black to attenuate background scattering from the laser.

Figure 2.7: 10º sharp fin as mounted on the flat plate for experiments at Mach 8.

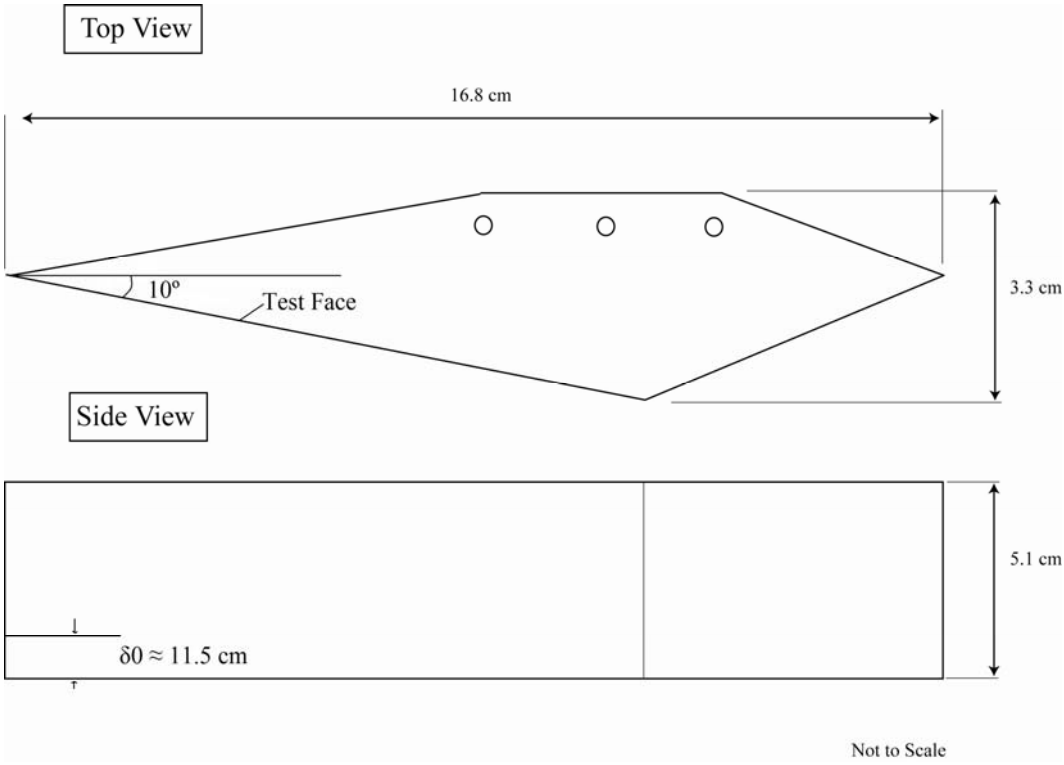

Figure 2.8: Schematic of the 10º sharp fin indicating appropriate dimensions.

2.2.4 Surface Oil Flow Visualizations

The surface shear stress pattern was visualized using an oil flow technique. The oil mixture used was 1,000 centistokes Dow Corning 200® silicon fluid mixed with titanium dioxide powder (1 μm particle size). The silicon fluid was chosen based on its high viscosity, low vapor pressure and ability to operate in high temperatures. The white titanium dioxide powder was added to the clear silicon fluid to create a strong contrast between the oil flow and the black surface of the model. Also, as the oil flowed across the surface, the powder was left behind showing a clear trace of the surface flow features.

The mixture was applied using a syringe in several rows of small dots just ahead of the expected beginning of the interaction in both the sharp fin and compression corner experiments. Additional rows of oil dots were applied inside and slightly behind the expected interaction region. The tunnel was started, without preheat, and run for approximately 15-25 seconds with the stagnation pressure set at 1000 psi. The oil mixture flow was visualized using a Canon Elura Progressive Scan CCD Camcorder, which recorded to a mini-DV (Digital Video) cassette. The video system was used due to concerns about the oil flow being disturbed by tunnel shutdown. This concern was correct as significant distortion of the surface pattern was observed upon tunnel shutdown, which made it impossible to make post run measurements.

Data analysis was accomplished by printing out the still images and measuring angles and distances by hand. Angle measurements in the sharp fin interaction were estimated to be correct within $\pm 2^{o}$.

2.2.5 Data Acquisition

In order to monitor and establish the tunnel operating conditions, measurements of stagnation pressure, stagnation temperature, nozzle exit static pressure and upstream plate static pressure were taken. The pressure and temperature in the stagnation chamber was monitored using an Omega 2000 psig pressure transducer and type K thermocouple. Nozzle exit pressure was monitored by a MKS Baratron 10 torr (0.19 psia) pressure transducer. A MKS Baratron 100 torr (1.96 psia) pressure transducer monitored the static pressure above the plate well upstream of the interaction regions. The data was collected through the same computer control system as described previously for the LTVG wind tunnel Mach 2.9 experiments.

2.2.6 Test Procedures

The nominal stagnation pressure for these experiments was 1000 psi. Eight hours prior to the run, the heater coil power was turned on and allowed to reach 810 K (1000º F). Prior to each run, except for the oil flow visualizations, the control valve was opened to approximately 400 psi in order to preheat the tunnel sidewalls and model. When the model reached 500 K, the tunnel was shutdown by closing the control valve. The preheat allowed the wall temperature to reach approximately 75% of the adiabatic wall condition. With the tunnel supply air off, the ejectors were started and allowed to reach steady state ($P_s \approx 0.6$ psia) at which point the tunnel supply air was brought up again. The stagnation pressure was overshot to 1400 psi to ensure tunnel start and then brought down to the nominal value of 1000 psi. Actual run conditions were typically within 2% of nominal value and varied less than 2% over the course of a run for both P_0 and T_0.

2.3 Filtered Rayleigh Scattering

In addition to the conventional diagnostic tools used to investigate the flows described above, a technique known as CO_2 Enhanced Filtered Rayleigh Scattering (FRS) was used to image and obtain both quantitative and qualitative information from these flowfields. The development and application of this technique is detailed by Erbland et al. (1997). A brief overview is offered here.

2.3.1 General Overview

Filtered Rayleigh Scattering (FRS) was used to visualize the structure of the boundary layer in all canonical cases. Rayleigh scattering is the scattering of light from particles that are of the order of (or less than) the wavelength of light. If the scatterers are individual molecules, then the velocity, temperature, pressure and density can be determined from the shape and location of the intensity versus frequency curve of the scattered light. If the scatterers are not individual molecules, the static temperature and pressure information may be lost, but other useful information may still be obtained. The scatterers used in the Mach 2.9 and Mach 8 experiments were condensed nanometer scale particles of CO_2, which are used to enhance the Rayleigh scattering signal. Because the CO_2 particles are not individual molecules, quantitative information such as temperature, pressure and density were lost. However, much information on the structure of the interactions was discovered using the FRS technique.

In both the HyperBLAF and LTVG, the carbon dioxide is injected upstream of the stagnation chamber so that the mass flux of CO_2 was about 1.0% of the tunnel air mass flux. As the air-CO_2 mixture cools in the nozzle, the CO_2 condenses and forms clusters

that were estimated by Erbland (1997) to be of order 10 nm. When the CO_2 clusters become entrained in the boundary layer, aerodynamic heating effects in the boundary layer causes the temperature to rise above the sublimation value and the condensate vaporizes. The boundary layer is therefore imaged as a region of low intensity Rayleigh signal, bounded by bright regions corresponding to freestream fluid. The interface between the hot boundary layer fluid and the cold freestream flow is well-represented by the intensity of the Rayleigh scattering signal since the time scale of the sublimation is small compared to the typical time scales of the entrainment process (Forkey, 1996).

In the initial experiments at the Mach 2.9, we attempted to use the inherent water vapor in the supply air as the scattering particles. Even though the air is dried and filtered, there is estimated to be 13 parts per million water in the air. The low densities explored in the Mach 2.9 studies provided inadequate scatterers and no flow could be visualized in early experiments. Consideration was given to removing the drier from the compressor process, but the possibility of long term damage to the air supply system ruled this out. Analysis of the thermodynamic properties in the Mach 2.9 flow showed that CO_2 would indeed sublimate and provide the necessary scattering particles in the freestream.

The difference between Rayleigh scattering and filtered Rayleigh scattering is the ability to differentiate between scattered light from the flow and background scattering from the models and tunnel walls. Figure 2.9 shows how filtered Rayleigh scattering is used to make this distinction. The scattering signal is Doppler-shifted by an amount that depends on the angles between the camera, the laser vector, and the predominant flow vector. The Doppler-shift is proportional to the flow velocity. The magnitudes of the signals in Figure 2.9 are not to scale. Typically, the signal from background scattering

outweighs that of the flow scattering. Therefore, an extremely narrow molecular filter is placed between the flow and the camera which attenuates background scattering which occurs at the laser frequency and is not Doppler shifted.

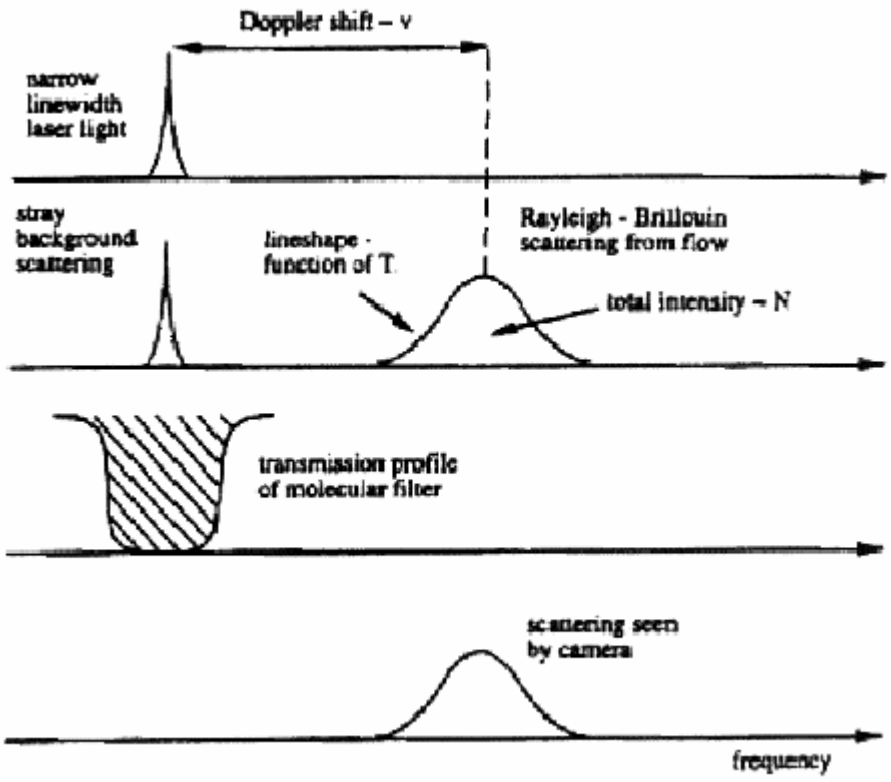

Figure 2.9: Concept of using molecular filter to suppress background scattering. From Forkey (1996).

2.3.2 Apparatus

Laser and Optics

The laser used in these experiments was a Spectra-Physics Quanta Ray, Q-switched, injection-seeded, frequency-doubled Nd:YAG pulsed laser with pulse energies in the 150 mJ range (Miles et al, 1992). Pulses are generated at 10 Hz with a pulse length of 10 ns. The laser could be tuned to the desired frequency in the absorption band of the filter by inputting a voltage to the injection seeding.

Figure 2.10 andFigure 2.11 show schematics of the optical configurations for the Mach 2.9 and Mach 8 flows, respectively. Several first-surface mirrors were used to direct the laser beam into the test section. A single half-wave polarizer was used to orient the polarization of the laser light to maximize the scattering in the plane perpendicular to the camera. A focusing lens followed by a cylindrical lens was used to focus the beam in one direction and spread it in the other. This created a sheet of light in the test section near the surface of the models with a sheet thickness that was estimated to be about 100 μm in the imaging region, with the centerline of the sheet at 135º to the mean streamwise flow vector.

The laser sheet orientation was the same as that shown in Figure 2.11 for the 12º reflected shock case, with the laser sheet entering the test section just behind the shock generator. In the case of the 8º compression ramp experiment at Mach 8, the laser configuration was similar to the setup shown for the Mach 2.9 compression ramp study.

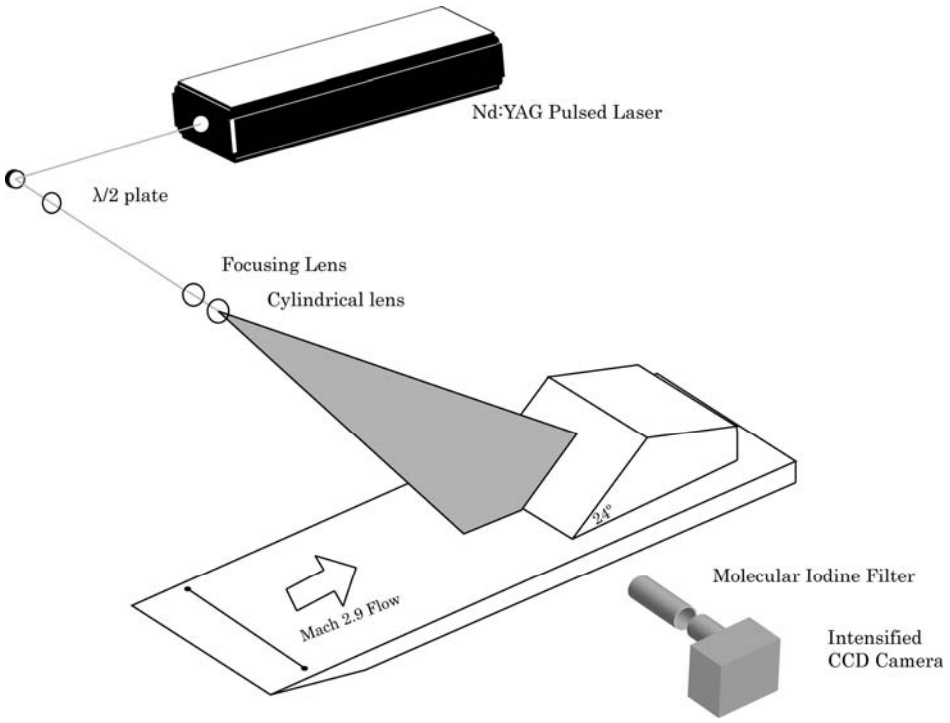

Figure 2.10: Optical arrangements for FRS imaging in Mach 2.9 experiments.

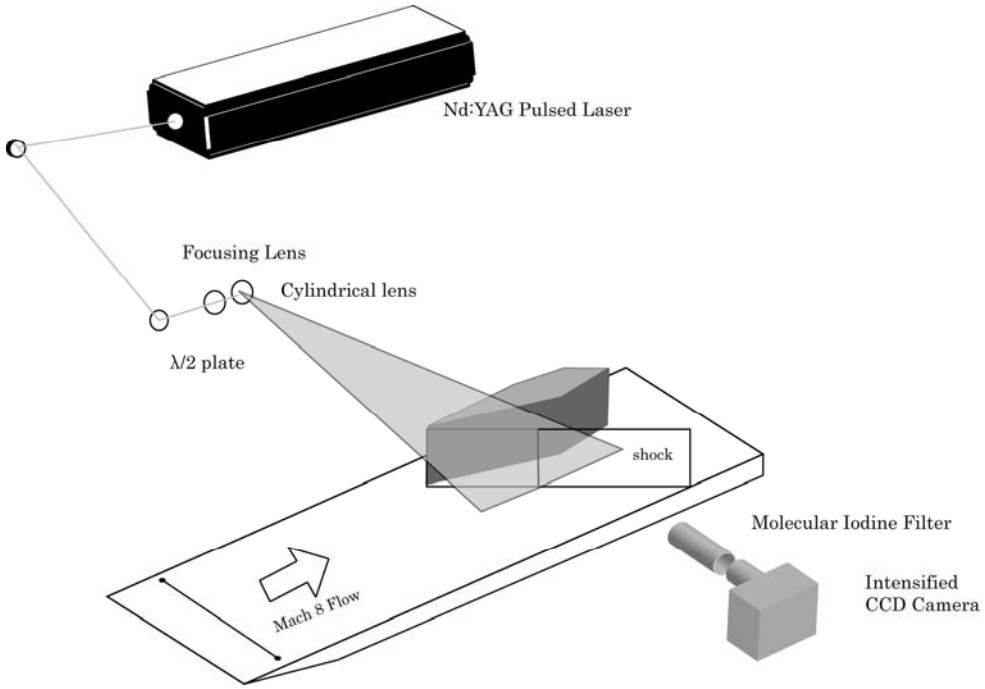

Figure 2.11: Optical arrangements for 10° sharp fin experiments at Mach 8.

Iodine Cell and Camera

Figure 2.12 shows a schematic of the iodine filter used to attenuate background scattered light. It was simply a glass cell with a fixed volume filled with iodine vapor. The opacity of the vapor cell depends on its density. The vapor pressure was controlled in the cell by a hot water bath at 50º C. To prevent iodine condensation on the walls of the cell, the entire cell was wrapped with heating tape and its temperature controlled at 80º C. The choice of the iodine cell was made based on previous experiments conducted in the same facilities. Forkey (1996) detailed the main advantages of using iodine. The iodine vapor transmission spectrum overlaps the Nd:YAG second harmonic and its wide distinctive absorption band makes it ideal for use in Filtered Rayleigh scattering applications.

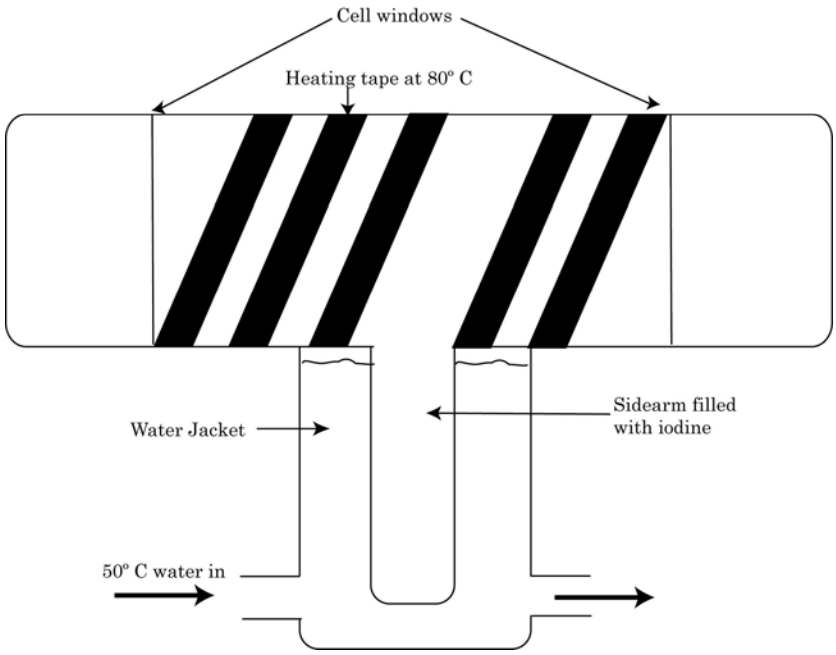

Figure 2.12: Schematic of the iodine cell used to suppress background scattering.

Figure 2.13 shows the transmission spectrum for the iodine cell that is within the tuning range of the laser with the water bath at 50º C and the sidewalls at 80º C. It was created by carrying out a voltage sweep to the input of the injection seeding. The wide band (≈ 1 GHz or 1 Volt) centered around 2.5 Volts with essentially zero transmission was the absorption band used in these experiments. In order to tune the laser into the absorption band, the voltage sweep described above was carried out several times to establish the repeatability of the filter temperature settings. The absorption band was found to be very steady with the filter setting set the same each time. Therefore, the laser injection voltage was selected and remained constant throughout the course of these experiments. Image quality was then only a function of the camera gain settings.

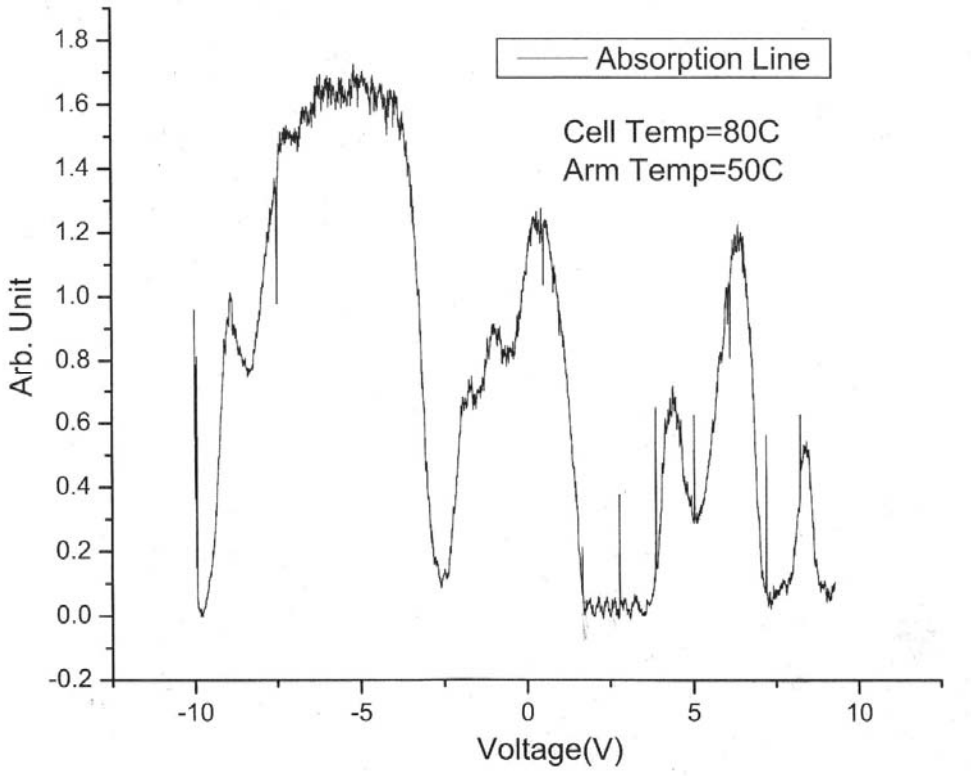

Figure 2.13: Molecular iodine filter transmission spectrum.

A double-intensified CCD camera with a 100 mm focal length f/4.5 lens was used to image the flow. The output of the camera was passed to a commercial grade SVHS recorder and video monitor. The camera settings were controlled by a simple DOS based program that allowed control of gain, exposure time, and trigger delay. The camera was triggered from the Q-switch output of the laser. The exposure was set to 1 ms, ensuring the capture of the 10 ns pulse from the laser. Before each run, the gain setting in the control program was set and rarely adjusted during the course of a run. The potentiometer dial on the back of the camera allowed small scale gain adjustments. The iodine filter was placed directly in front of the lens to suppress background scattering. The filter and camera were placed perpendicular to the laser sheet as shown in Figure 2.10 and Figure 2.11.

CO_2 Injection System

The system used to inject CO_2 into the air supply for the Mach 8 experiments was designed and is described in detail by Erbland et al. (1997). The injection system is linked to the tunnel air supply just downstream of the stagnation pressure control valve but upstream of the heater. CO_2 compressed gas cylinders arrive from the distributor in both the liquid and gas phase at vapor pressure of approximately 800 psi. This would not push the CO_2 into the tunnel supply air due to the high stagnation pressures used to drive the tunnel (1000 psi). Special cylinders that allow access to both the liquid and gas phases of the CO_2 were obtained, which allowed the liquid portion to be injected into the supply air by a driver gas connected to the gas phase at the top of the CO_2 cylinder. The driver gas was helium, which arrived in cylinders at 2800 psi. The helium pressure at the

top of the CO_2 cylinder was maintained at 1500 psi, which allowed adequate control of the flow of liquid CO_2 through an Omega volume flow meter and a precision flow valve. The meter was calibrated for water flows, but a simple specific gravity conversion allowed for accurate mass flow rates since the pressure and temperature of the liquid CO_2 were known from measurements just upstream of the meter. Figure 2.14 shows a schematic of the injection system. A similar system was adapted for use in the Mach 2.9 experiments. Here, the CO_2 was injected into the tunnel just downstream of the control valve, well upstream of the settling chamber. In both the Mach 2.9 and Mach 8 flows, the flow of CO_2 was adjusted so that the CO_2 to air mass flux fraction was approximately 1%.

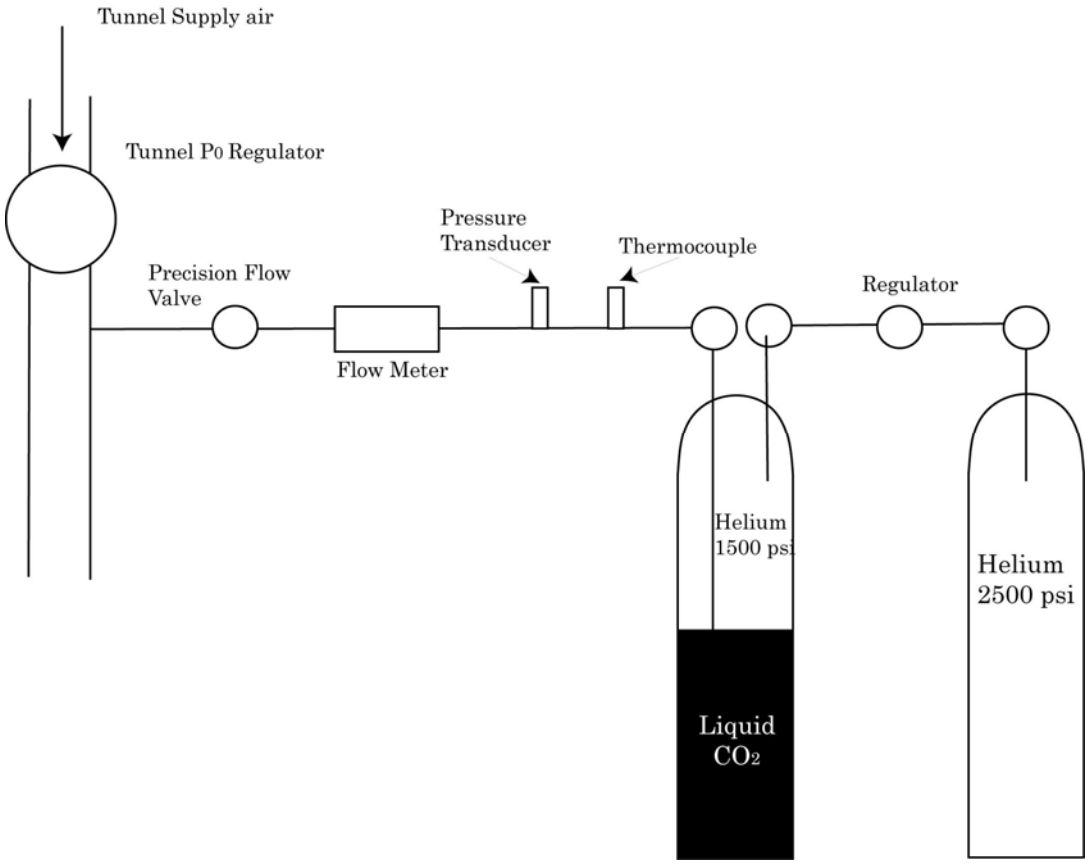

Figure 2.14: Schematic of the CO_2 injection system used in both Mach 2.9 and Mach 8 experiments.

Chapter 3 Mach 2.9 Experiments

This chapter describes the overall results of the experimental investigations at Mach 2.9. Included here are results from the investigation of the undisturbed boundary layer developed on the flat plate, the 24º compression corner and 12º reflected shock interaction. These results include mean flow surveys, surface pressure distributions, surface oil flow visualizations and Filtered Rayleigh Scattering imaging.

3.1 Undisturbed Boundary Layer

3.1.1 Mean Flow Surveys

This section provides the results obtained from a series of boundary layer surveys performed in the Mach 2.9 flow. The tunnel operating conditions were $P_0 = 10.6 \pm 0.1$ psia and $T_0 = 290 \pm 3$ K. Velocity and density distributions were calculated from stagnation pressure and total temperature profiles. In turn, the velocity and density distribution were used to determine the characteristic length scales developing in the boundary layer.

Data Reduction

The Pitot survey data, $P_{0,2}$, was used to determine the Mach number distribution in the boundary layers. The pressure measured by a Pitot tube in supersonic boundary layer is that pressure behind a normal shock ($P_{0,2}$) at the local Mach number (M_1). To

find the stagnation pressure, $P_{0,1}$, the standard Rayleigh-Pitot tube equation (White, 1991) was used:

$$\frac{P_{0,2}}{P_{0,1}} = e^{-(s_2 - s_1)/R} \tag{3.1}$$

where

$$s_2 - s_1 = c_p \ln\left\{\left[\left[1 + \frac{2\gamma}{\gamma+1}\left(M_1^2 - 1\right)\right]\left[\frac{2 + (\gamma-1)M_1^2}{(\gamma+1)M_1^2}\right]\right\} - R\ln\left[1 + \frac{2\gamma}{\gamma+1}\left(M_1^2 - 1\right)\right] \tag{3.2}$$

By assuming a constant ratio of specific heats ($\gamma = 1.4$), equation 3.1 can be solved for the local Mach number, M_1. $P_{0,1}$ is the local stagnation pressure and may not be equal to the settling chamber stagnation pressure. An isentropic form of the energy equation is solved simultaneously with equation 3.1 to account for this unknown.

$$\frac{P_{0,1}}{P_1} = \left(1 + \frac{\gamma - 1}{2} M_1^2\right)^{\frac{\gamma}{\gamma-1}} \tag{3.3}$$

Using the measured static pressure (P_1) and assuming it to be constant throughout the boundary layer gives the local Mach number distribution.

Once the Mach number distribution was known, the static temperature was found using the experimentally obtained stagnation temperature $T_{0,2}$ and the one-dimensional energy equation:

$$T = T_{0,1}\left(1 + r\frac{\gamma - 1}{2} M_1^2\right)^{-1} \tag{3.4}$$

Since the stagnation temperature is unchanged through a normal shock, the local stagnation temperature $T_{0,1}$ is equal to the probe stagnation temperature $T_{0,2}$. The recovery factor, *r*, was included to account for heat conduction away from the probe tip. A complete calibration was not conducted to find *r*, but it was determined through a

quasi-calibration of the probe in the freestream flow outside the boundary layer. The recovery factor was found to be 0.87.

With the local Mach number and static temperature distributions, velocity and density profiles were found using the following equations:

$$u_1(y) = M_1(y)\sqrt{\gamma R T_1(y)} \tag{3.5}$$

$$\rho_1(y) = \frac{P_w}{R T_1(y)} \tag{3.6}$$

Once the local velocity and density profiles have been determined, the characteristic scales can be determined by integrating to obtain the displacement thickness δ^*, and the momentum thickness, θ, as defined by the following equations.

$$\delta^* \equiv \int_0^\delta 1 - \frac{\rho}{\rho_\infty}\frac{u}{u_\infty}\,dy \tag{3.7}$$

$$\theta \equiv \int_0^\delta \frac{\rho}{\rho_\infty}\frac{u}{u_\infty}\left(1 - \frac{u}{u_\infty}\right)dy \tag{3.8}$$

In order to calculate Reynolds numbers, the correlation due to Keyes (1952) was used to determine the viscosity:

$$\mu = \frac{1.488\,x\,10^{-6}\sqrt{T}}{1 + \left(\frac{122.1}{T}\right)10^{-5/T}} \tag{3.9}$$

Boundary Layer Profiles

Surveys of the undisturbed boundary layer were taken on the flat plate centerline 375 mm downstream of the leading edge. Mean velocity, Mach number and density profiles are shown in Figures. 3.1, 3.2 and 3.3.

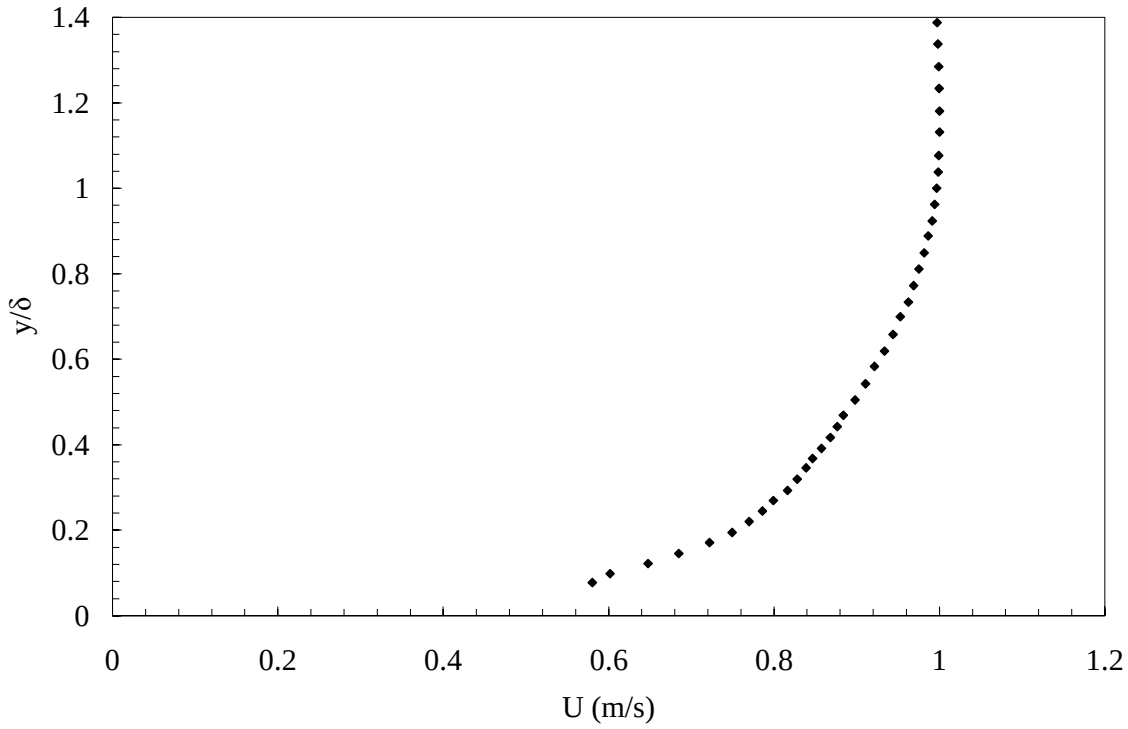

Figure 3.1: Undisturbed boundary layer profile at M = 2.9, Re_0 = 2400.

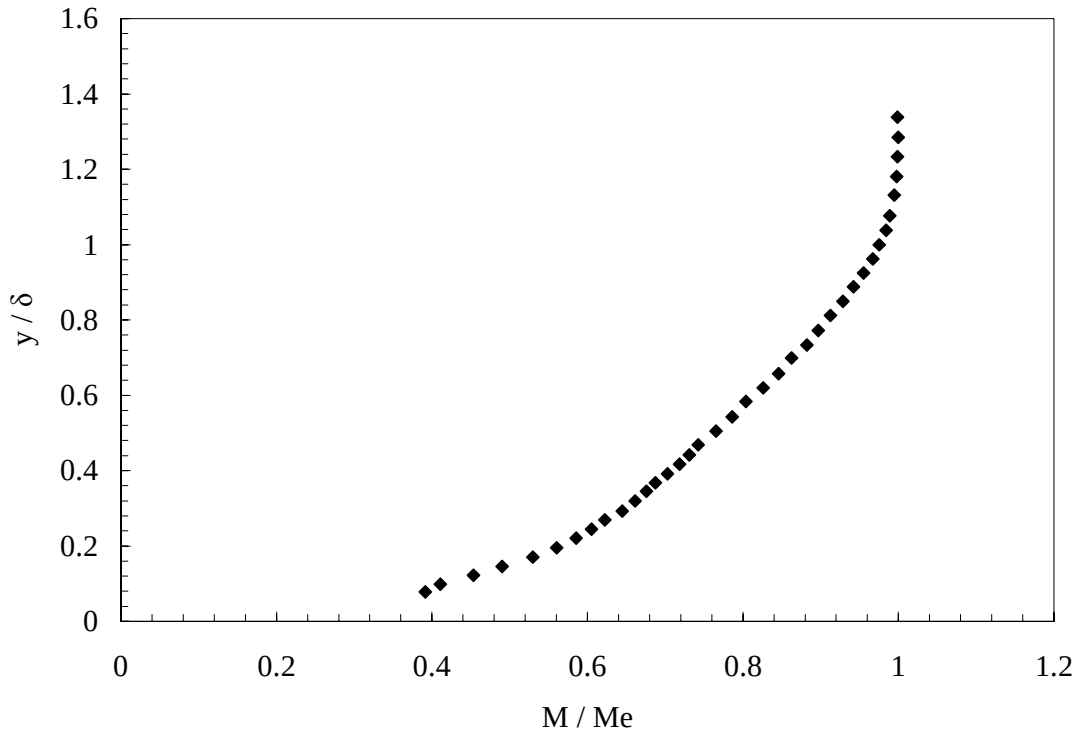

Figure 3.2: Mean Mach number profiles of the undisturbed boundary layer at Mach 2.9, Re_0 = 2400.

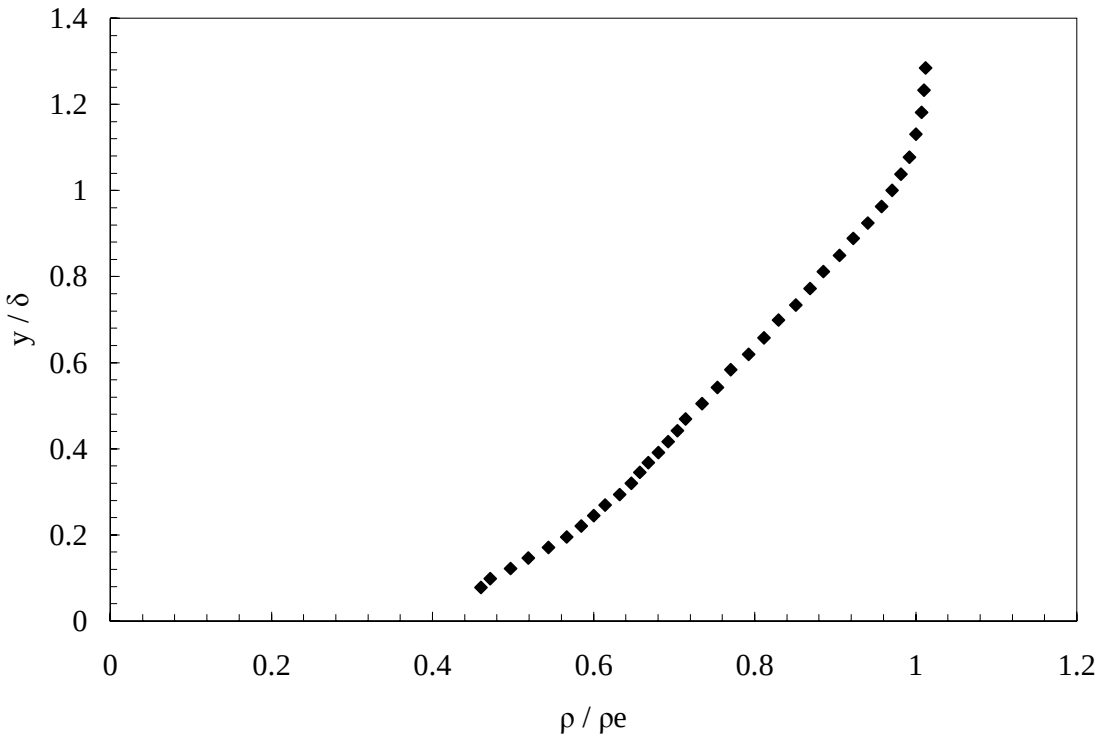

Figure 3.3: Mean density profiles for the undisturbed boundary layer at Mach 2.9, Re_0 = 2400.

Figure 3.4 presents a log-linear plot of the van Driest transformed effective velocity profiles. Included for reference are the theoretical curves for the linear sublayer ($u^+ = y^+$) and the log law. The value of τ_w was obtained by the Clauser chart method and used to non-dimensionalize the data shown in Figure 3.4. No probe corrections were made, and it was assumed that the Pitot probe measured the stagnation pressure at the mid-point of the flattened tip probe.

The transformed velocity profiles show a well-defined turbulent profile with small logarithmic region and wake-region typical of a low Reynolds number turbulent boundary layer. The dip seen in the logarithmic region is not believed to be the beginning of the buffer region between the linear sublayer and the log law. Due to the

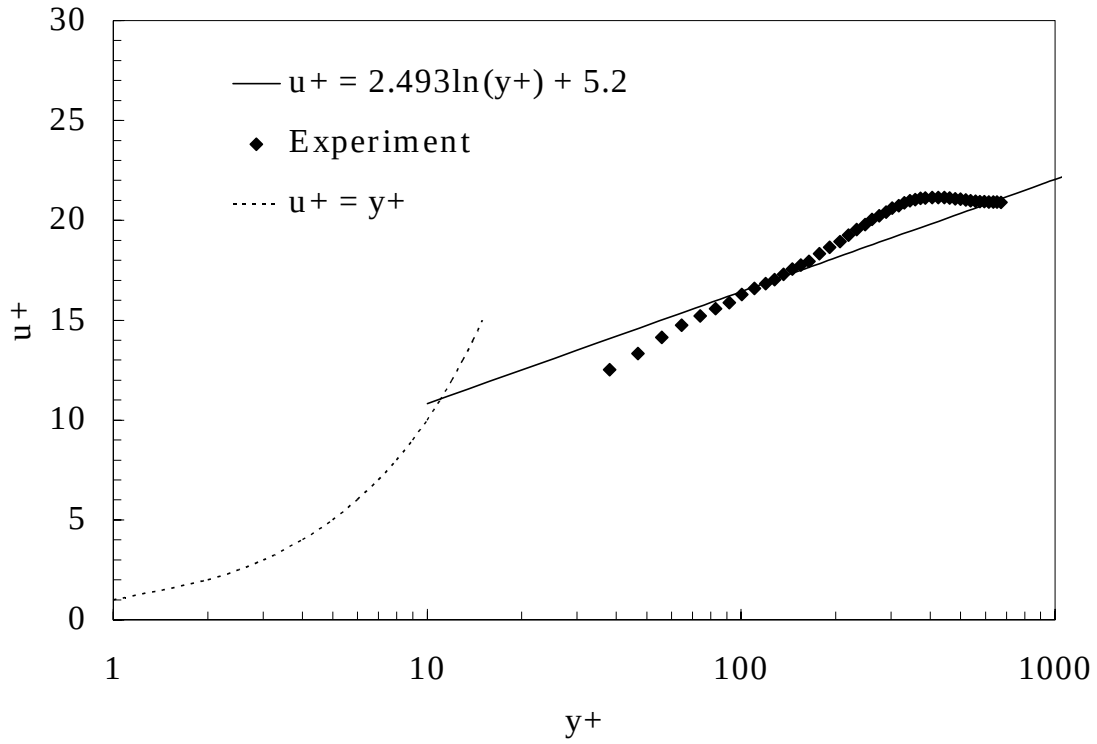

Figure 3.4: Velocity profile of the undisturbed boundary layer at M = 2.9, Re_0 = 2400 transformed according to van Driest using the Clauser method for wall shear stress.

short run times available and the low pressures being measured, a relatively large probe was required to provide acceptable time response at the cost of spatial resolution. Attempts were made to improve the spatial resolution by flattening the tip of the probe, but near wall data could not be obtained because of the large probe size. Further, the large probe created significant disturbance effects near the wall where the bow shock in front of the probe caused local separation of the boundary layer. Also, near the wall, the bow shock may not be normal to the probe, which was assumed in the analysis of the Pitot probe measurements. Despite the lack of highly accurate near wall data, the measurements for $y^+ \geq 80$ were believed accurate. The near-wall effects were expected to be small.

Characteristic Scales

Table 3.1 gives the characteristic scales and ratios for the incoming boundary layer: boundary layer thickness δ, displacement thickness δ*, momentum thickness θ, shape factor H≡δ*/θ, the Reynolds Number based on momentum thickness Re_θ, the skin friction coefficient C_f, and the friction velocity $u_\tau = \sqrt{\tau_w / \rho_w}$.

δ_{99} (mm)	δ^* (mm)	θ (mm)	$H = \delta^* / \theta$	Re_θ	C_f x 10^3	u_τ (m/s)
6.7 ± 2%	2.36 ± 5%	0.43 ± 15%	5.49	2400	2.25 ± 10%	33.6

Table 3.1: Characteristic scales of the undisturbed boundary layer at M = 2.9.

3.1.2 Filtered Rayleigh Scattering Images

Image Processing

The SVHS video tapes were digitized at the Princeton University New Media Center using Final Cut Pro software by Apple. After digitization, still images were grabbed from the movies at a resolution of 480 horizontal lines by 720 vertical lines. The still images were cropped, filtered and enhanced by a histogram stretch to highlight the areas of interest in each raw image. Calibration of the images was accomplished by capturing a digital image of a calibration grid in all directions. The image processing was done using algorithms built into Matlab Version 7.0. Only the high contrast portions of the images were used so that the interface between turbulent and non-turbulent fluid could be clearly distinguished. The steps taken in modifying the original digitized images are shown in Figure 3.5.

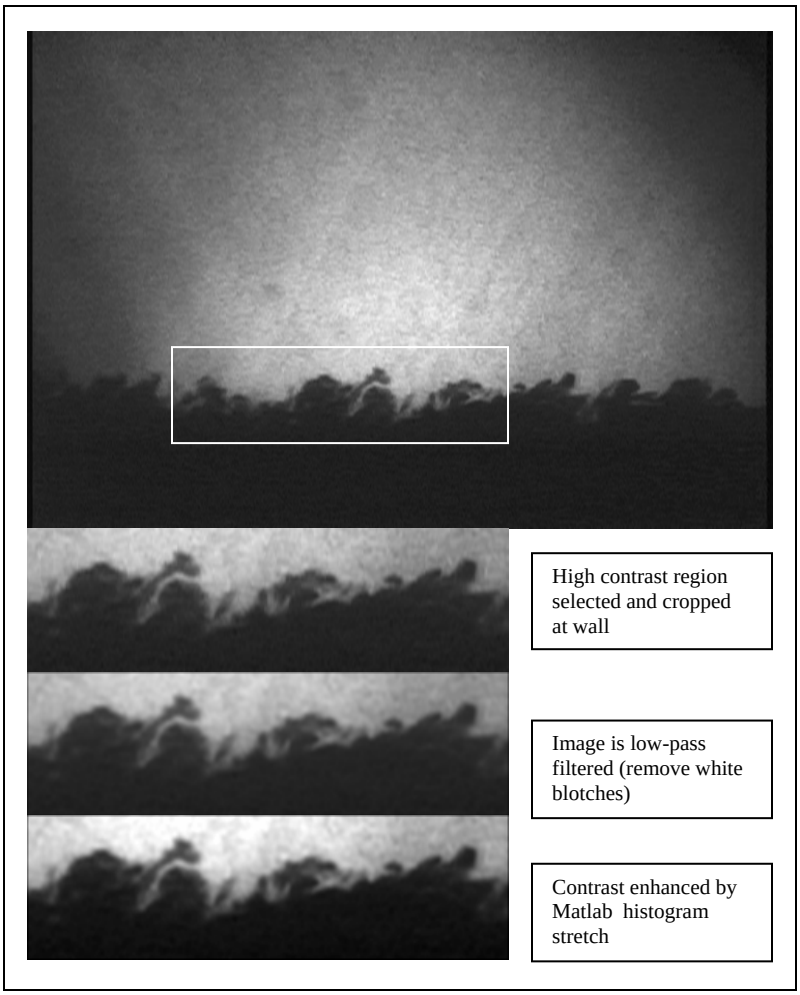

Figure 3.5: Image processing steps taken to improve original image quality.

Results

Vertical slices through the undisturbed boundary layer are shown in Figure 3.6. Each image was selected at random from over 100 digital images and represents a typical instantaneous picture of the boundary layer. It is important to remember that the images are uncorrelated due to the low laser pulse frequency. The interface between non-turbulent freestream fluid and turbulent boundary layer fluid was readily apparent, shown by the interface between dark and bright regions in the images. In several images, deep

incursions of bright freestream fluid are seen in the near-wall region and turbulent bulges are seen to extend well beyond the mean boundary layer edge.

Visual analysis of the images raises the question of what is actually being visualized in the boundary layer. The scattering signal in the images indicates the presence or absence of condensate particles, not necessarily the existence or not of turbulence. A link must be made between the concentrations of the scattering particles to the existence of turbulence. Several assumptions were necessary in order to make this link. The first was that there exists a temperature at which the vaporization of condensate particles is abrupt when reached or exceeded. Forkey (1996) offered a much more detailed explanation and analysis of the characteristics of sublimation and vaporization of

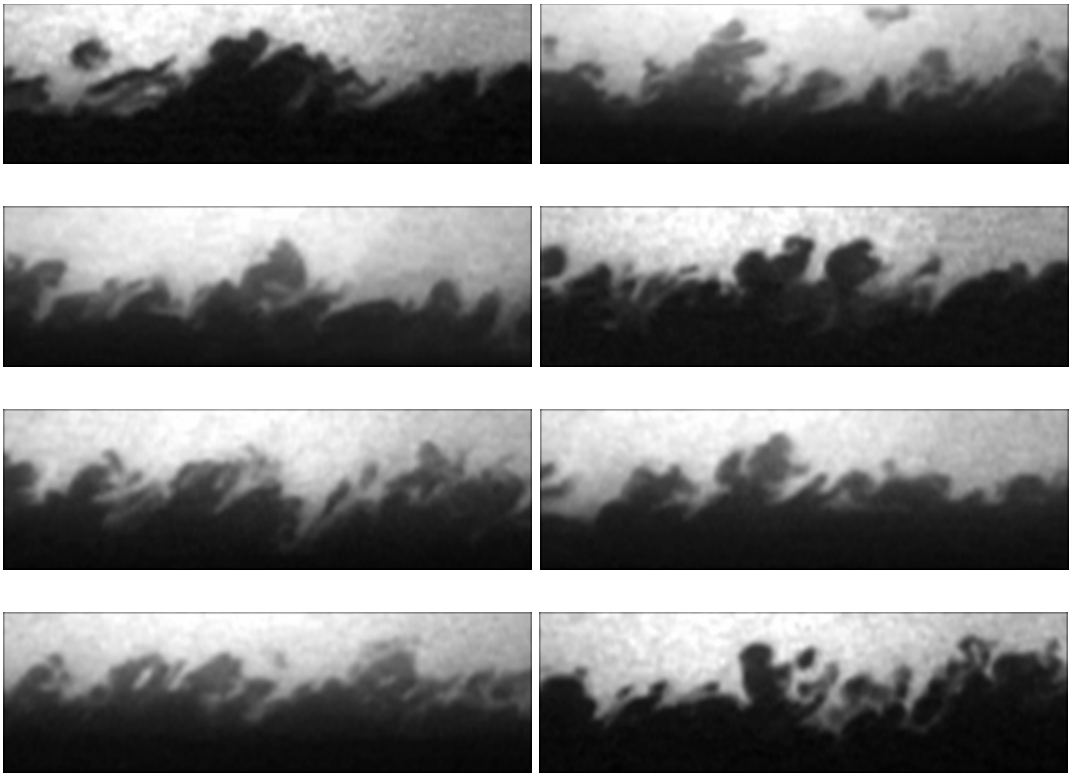

Figure 3.6: Eight-frame montage of vertical slices through the undisturbed boundary layer. Flow is from left to right and the bottom of the image corresponds to the wall location. The field of view is 1.5δ (10.1 mm) in the wall-normal direction and 5δ (33.5 mm) in the flow direction. M = 2.9, $Re_0 \approx$ 2400.

CO_2 particles, in which he provided evidence for this assumption.

The link between temperature and velocity fluctuations is made using the Strong Reynolds Analogy (SRA). The SRA is derived from the energy equation. Assuming total temperature fluctuations are small and pressure fluctuations are much smaller than density fluctuations, the SRA results in:

$$\frac{\rho'}{\overline{\rho}} \approx -\frac{T'}{\overline{T}} \approx (\gamma - 1)\overline{M}^2 \frac{u'}{\overline{u}} \tag{3.10}$$

The SRA indicates a negative correlation between temperature and velocity fluctuations. The negative correlation suggests that in a compressible turbulent boundary layer lower temperature, high speed fluid is on average swept inwards, while higher temperature, low speed fluid is ejected from the near-wall regions into the outer layers of the boundary layer. The SRA along with the analysis of the sublimation temperature of the CO_2 condensate particles provide a strong argument that the contrast between dark and bright regions in FRS images accurately represents the boundary between turbulent and non-turbulent fluid.

3.1.3 Intermittency

The intermittency function (λ) in a turbulent boundary layer provides information about the proportion of turbulent fluid at a given height in the boundary layer where $\lambda=1$ indicates a fully turbulent flow and $\lambda=0$ a non-turbulent flow. The interface between turbulent and non-turbulent fluid evolves as it moves downstream. Irrotational fluid is entrained into the boundary layer across the interface and to a stationary observer, the interface position is seen to be highly unsteady in time. The intermittency factor is often incorporated into the modeling of outer-layer turbulence. Klebanoff (1955) studied the

intermittency of incompressible boundary layers and defined the intermittency function at a given location as

$$\lambda(y) = \frac{1}{T}\int_0^T \Lambda(y,t)dt \tag{3.11}$$

where the boxcar function Λ is defined as 0 if the fluid at (y,t) is non-turbulent and 1 if the fluid at (y,t) is turbulent. A slightly different approach with the same concept was used to evaluate the intermittency of the compressible undisturbed boundary layer at Mach 2.9.

The intermittency function was evaluated from the high-contrast grayscale FRS images of the undisturbed boundary layer using a simple threshold technique. This technique involved selecting a threshold pixel value that determined whether a given pixel represented turbulent or non-turbulent fluid. Pixels with a value greater than the threshold became the maximum 8-bit grayscale value of 255, while pixel values at or below the threshold became a grayscale value of 0. The threshold pixel value was found by visual comparison of various threshold levels. The value that best represented the interface was found to be 65. Figure 3.7 shows the effect of varying the threshold ±10. Variation of the threshold level ±10 was taken as the uncertainty in determining the intermittency at a given height in the boundary layer. This corresponds to an uncertainty of ±10% for the threshold technique.

Thresholding was applied to an ensemble of 100 images with a field of view of 5δ in the streamwise direction and 1.5δ in the wall-normal direction, similar to those shown in Figure 3.6. The composite length of the image ensembles was over 700 δ. The intermittency function at various heights in the boundary layer was found by evaluating

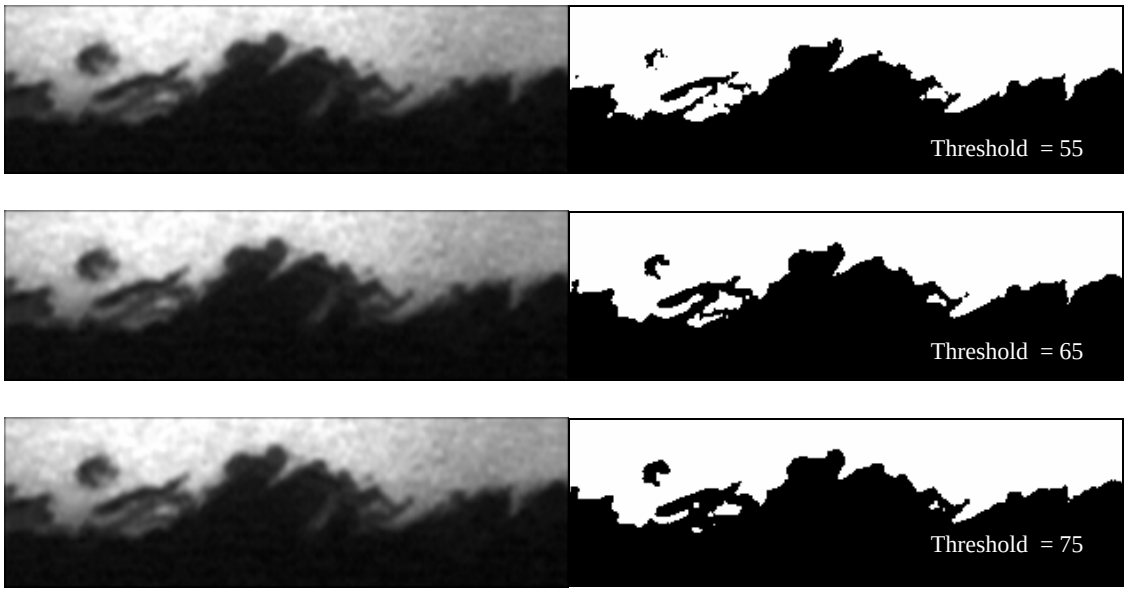

Figure 3.7: Effects of varying the threshold pixel value on the FRS images of the undisturbed boundary layer. The value of 65 most accurately represents the interface between turbulent and non-turbulent fluid. The two other example threshold levels show how the interface is misrepresented by a variation of ±10.

the fraction of turbulent pixels in a single row of pixels in the streamwise direction. The result of the threshold technique to find the intermittency function is shown in Figure 3.8 compared to the incompressible curvefit of Klebanoff's data from White (1991). The M = 2.9 data is remarkably similar to the incompressible curve. The profile is slightly steeper, suggesting that the turbulent fluid persists further into the outer layers of the boundary layer. However, the differences in techniques and the uncertainty involved in the subjective nature of the threshold technique made it difficult to draw a strong conclusion on any real difference between the compressible and incompressible intermittency profiles. The mean position of the interface (where λ is 50%) was found to be at about $y/\delta = 0.77$. This is in excellent agreement with the mean position of the interface for incompressible boundary layers (Smits, 2000).

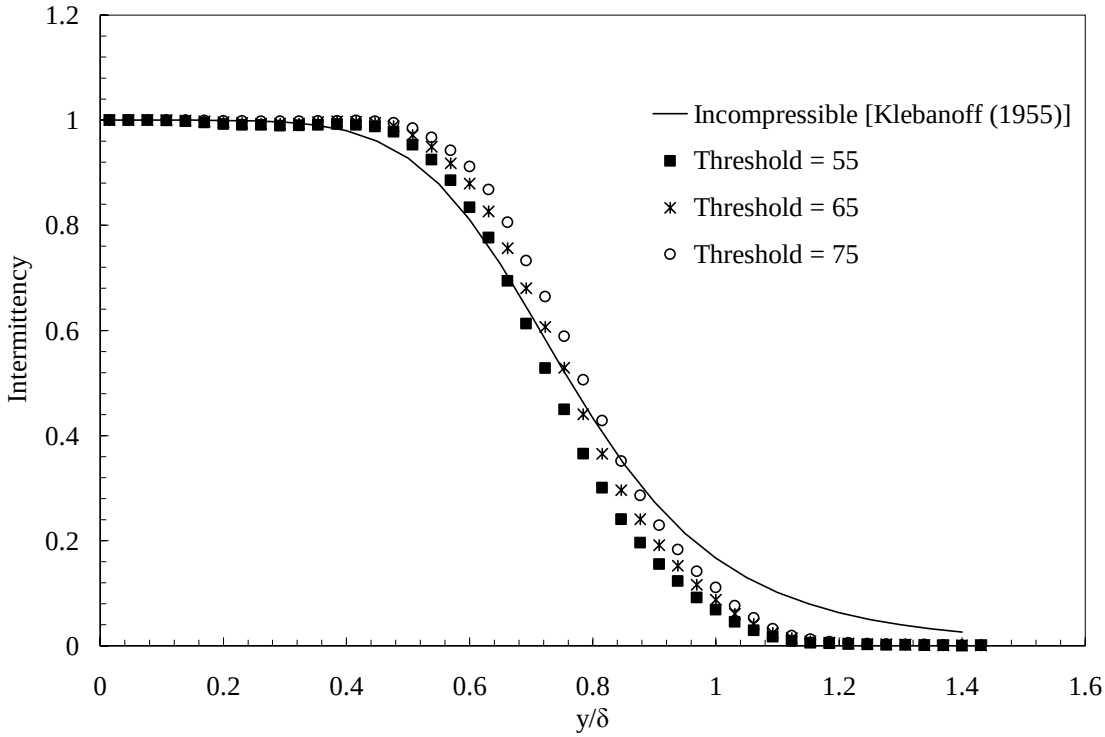

Figure 3.8: Intermittency function taken from 100 FRS images of the undisturbed boundary layer.

3.1.4 Mean Structure Angle

The FRS images also provided quantitative information about the mean structure angle of organized structures in the undisturbed boundary layer. The angles were determined from the use of spatial correlations of the FRS imaging data. Correlations indicate the tendency of two random variables to have a linear relationship, and are useful to determine any functional relationship between the pair of variables. The correlation coefficient is defined as follows (Milton and Arnold, 1986):

$$\mathbf{C} = \frac{\mathbf{Cov(X,Y)}}{\sqrt{\mathbf{Var(X)}}\sqrt{\mathbf{Var(Y)}}} \tag{3.12}$$

The sample size is limited by the number of images used, so estimators for the covariance and variance of the random variables must be used. The familiar equations for the

variance and covariance of a random sample are used as these estimators [cf. Poggie (1991)], resulting in the correlation coefficent:

$$C_{i,j} = \frac{\sum_{n=1}^{k} \left(X_{i,j}^{k} - \bar{X}_{i,j} \right) \left(X_{i_0,j_0}^{k} - \bar{X}_{i_0,j_0} \right)}{\sqrt{\sum_{n=1}^{k} \left(X_{i,j}^{k} - \bar{X}_{i,j} \right)^2} \sqrt{\sum_{n=1}^{k} \left(X_{i_0,j_0}^{k} - \bar{X}_{i_0,j_0} \right)^2}} \tag{3.13}$$

where, in the context of the FRS images, X^k is the variable representing the grayvalue of frame *k*, *i* and *j* are pixel coordinates, 0 denotes a reference coordinate and $\bar{X}$ is the ensemble grayvalue average. A correlation coefficient of 1.0 indicates a perfect linear relationship between the two random variables. A zero indicates no relationship, while a coefficient of -1.0 indicates a perfect inverse relationship.

Correlations were completed on the same ensemble of FRS image as the intermittency analysis. The original 1.5δ x 5δ image was separated into three 1.5δ x 1.5δ sections to increase the number of frames available for the correlation. The extent of the correlation was not expected to be any greater than δ, so the divided frames were assumed to be independent realizations of the turbulence structure. With the division of the images, the correlations were performed on an ensemble of 300 frames. In order to evaluate the correlation at various heights in the boundary layer, the location of the reference point was varied in the wall-normal direction from the wall to just outside the boundary layer edge. The reference point in the streamwise direction was held constant at the center of the images. Figure 3.9 shows four representative images of the correlations, where the correlation coefficient has been mapped into grayscale values. Included are versions of the coefficient maps where the correlation coefficients have been mapped into seven levels to aid in interpretation. Coefficients less than 0 are represented

by black; grayvalues represent levels of 0 to 0.2, 0.4 to 0.6, 0.6 to 0.7, 0.7 to 0.8, and 0.8 to 0.9; coefficients greater than 0.9 are represented by white.

The results reveal that there exist large areas of correlation when the reference point is taken near the boundary layer edge. These large areas appeared in both the $y/\delta = 1.0$ and $y/\delta = 0.75$ as shown in Figure 3.9 as freestream fluid often penetrated into the outer layer of the boundary layer. As the reference point was moved closer to the wall, the correlation levels quickly degraded, as shown in the correlation plot for $y/\delta = 0.3$. The loss of signal began for correlations taken at $y/\delta \leq 0.4$. The horizontal feature of the correlations indicated some kind of uniform noise or loss of signal that was not believed to be attributed to the actual structure of the boundary layer at these heights. It was therefore possible to draw conclusions only on the organized structures in the outer half of the boundary layer.

Another feature of the correlation images is the inclination of the major axis of the ellipse-like isocorrelation contours. Although not obvious to the naked eye, the angle with respect to the wall of the contours increases with height. In order to quantify these angles, ellipses were fit to the isocorrelation contours using a direct least squares fitting method developed by Fitzgibbon et al (1999). The algorithm was applied to contour levels of 0.7, 0.8 and 0.9 for each correlation corresponding to the various boundary layer heights, and the angle of the major axis with respect to the wall of each contour was determined The average of the three contours at each boundary layer height was taken to be the mean structure angle. The result of the mean structure angle analysis is shown in Figure 3.10 compared to the hot-wire space-time correlations of Spina et al. (1991) for flow at $M = 2.9$, $Re_\theta \approx 80{,}000$.

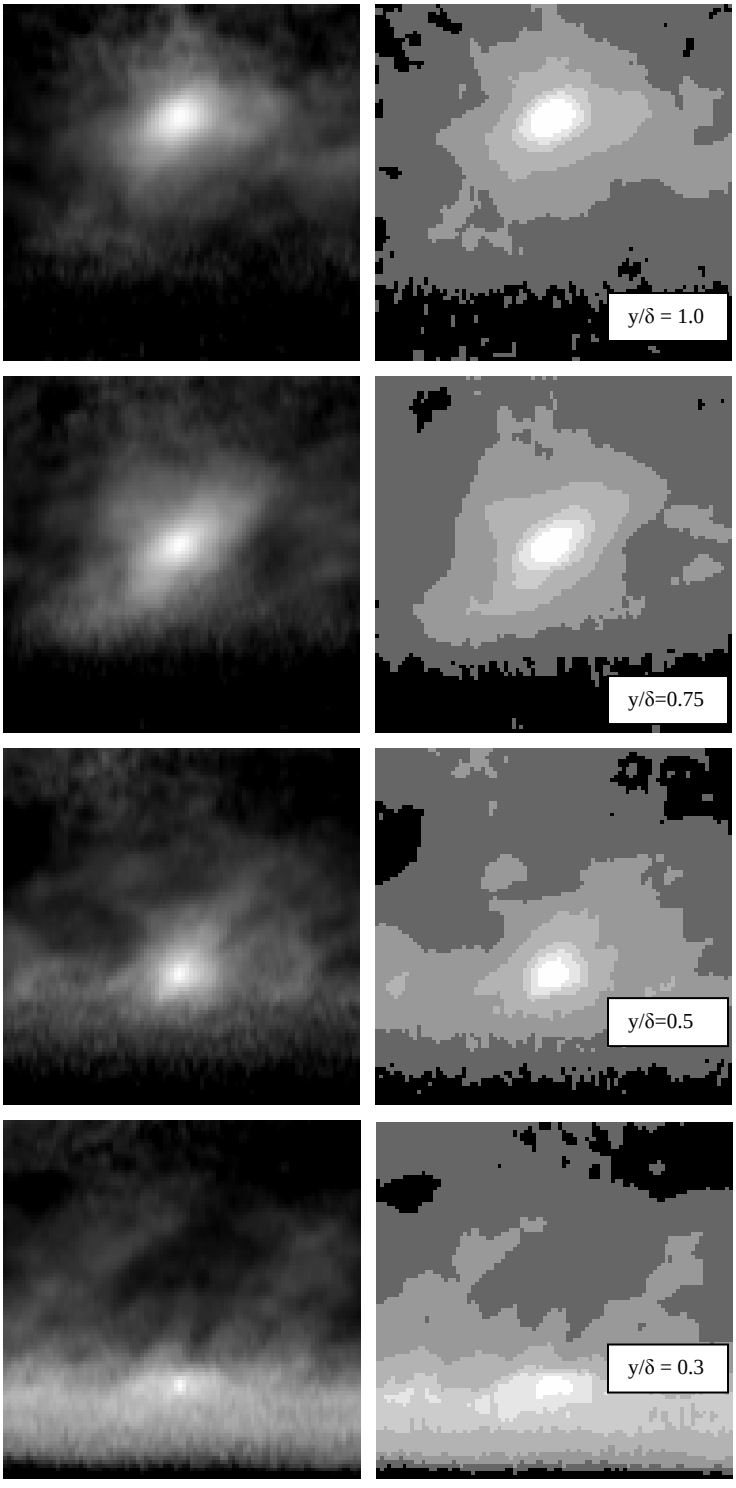

Figure 3.9: Correlations of Mach 2.9 undisturbed boundary layer. Images on the left represent raw values of the correlation coefficient. Images on the right represent the coefficients mapped into seven levels. Images are 1.5δ x 1.5δ with the flow from left to right, with the wall location indicated by the bottom of the image.

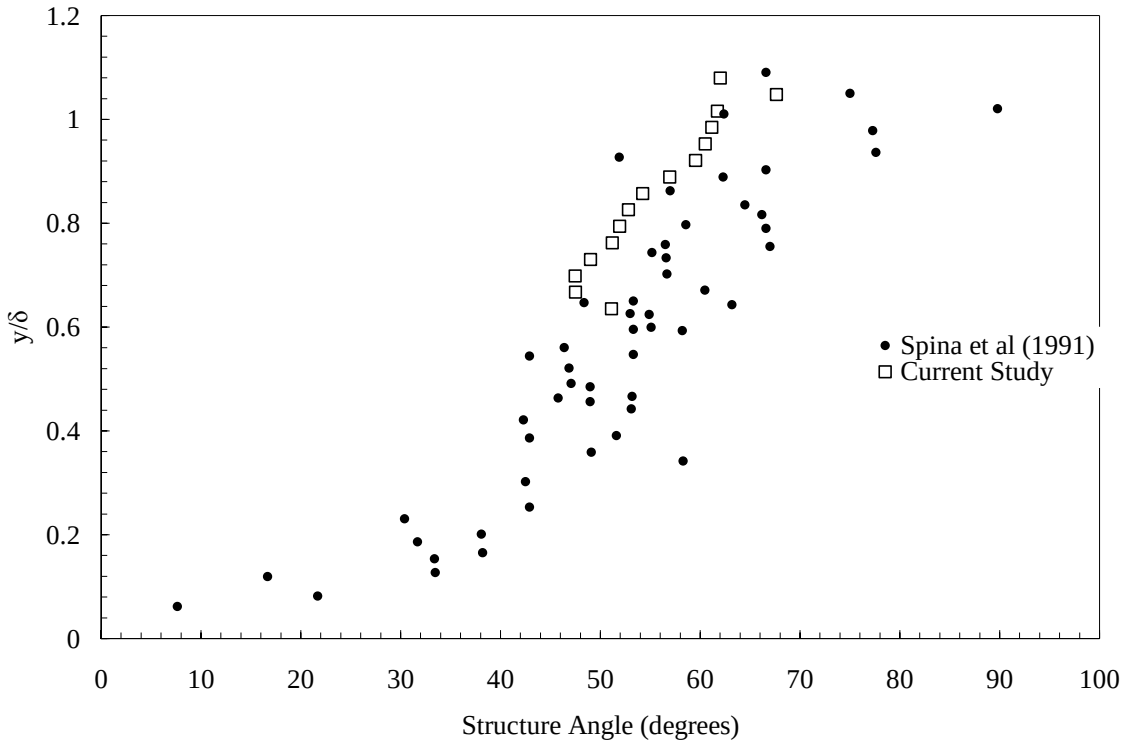

Figure 3.10: Mean structure angle in the undisturbed turbulent boundary layer at Mach 2.9, Re_θ = 2400 compared to the hot-wire results of Spina et al (1991), M=2.85, Re_θ = 80,000.

The measurements of Spina were taken at various hot-wire spacing. The angle of the structures was seen to be dependent on the spacing and tends to shift the points up and to the left in Figure 3.10. The structure angle results showed excellent agreement with Spina's results, lying on the lower extent of the higher Reynolds number data. The correlations taken in this study were done over very large areas (1.5δ x 1.5δ), so the fact that there was good agreement with large hot-wire spacing was not surprising.

3.2 24º Compression Corner Interaction

The 24º compression corner interaction was studied at the same conditions as described for the undisturbed boundary layer. The flow was examined using surface flow visualization, boundary layer surveys, surface pressure measurements, and FRS. The results of these experiments are reported in this section.

3.2.1 Surface Oil Flow Visualization

The 24º compression corner was visualized using the silicon/graphite mixture described in Chapter 2. A typical surface flow visualization image of this interaction is shown in Figure 3.11. Significant features of the image are highlighted for clarification.

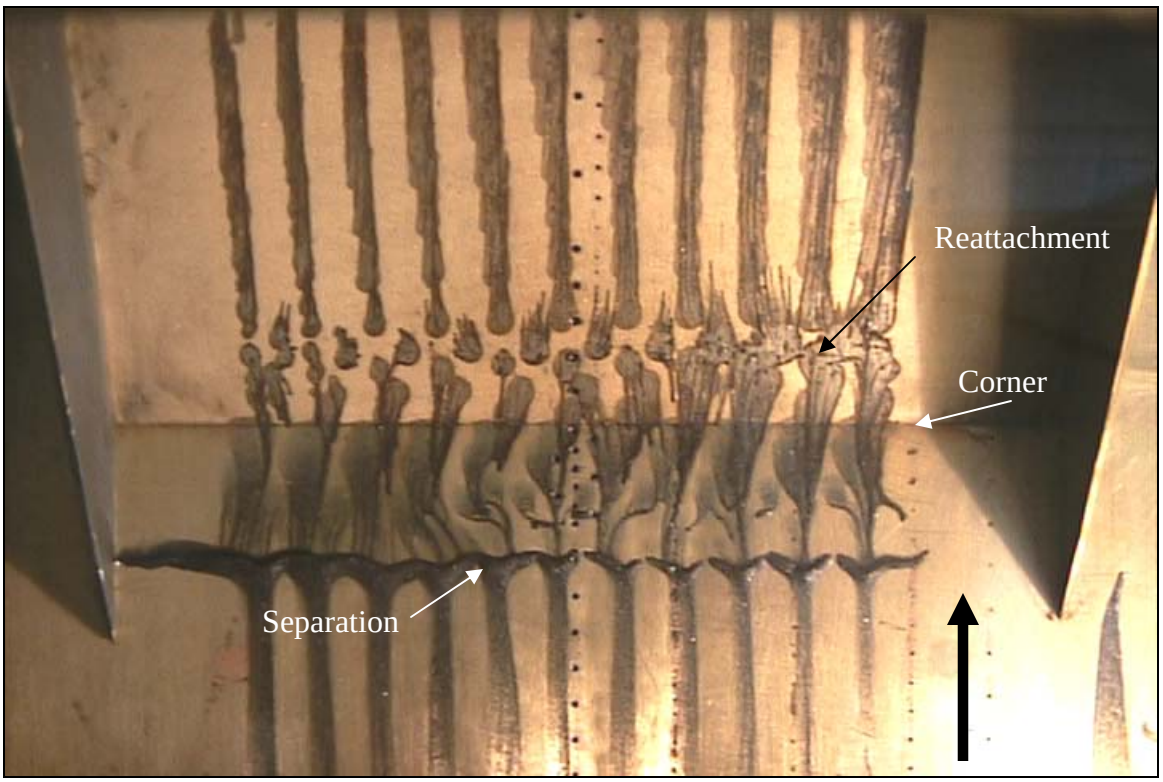

Figure 3.11: Surface flow visualization of the 24º compression corner at Mach 2.9, Re_0 = 2400.

Measurements were made of the location of the separation line from Figure 3.11. The mean location of separation was found to be 3.2 δ_0 upstream of the corner. Also evident from Figure 3.11 was the three dimensional nature of the interaction. The combination of the curvature of the separation line and the alternating direction of curving surface lines in the separated region probably indicate the presence of pairs of counter-rotating vortices aligned in the streamwise direction. Reattachment was found to occur 1.6 δ_0 downstream of the corner. Beyond reattachment, the surface flow was highly two-dimensional as the fluid is seen in very straight streamwise lines in Figure 3.11. The location of the separation and reattachment lines indicated that the streamwise extent of the separated region was significantly greater than the same configuration at higher Reynolds number. Settles (1975) found the separation and reattachment lines to occur at $x = -1.7\ \delta_0$ and $x = 0.8\ \delta_0$ respectively.

3.2.2 Surface Pressure Distribution

The surface pressure distribution was measured through the use of 25 static pressure ports installed into the centerline of the flat plate and the compression corner model. The pressure ports were connected to the Scanivalve, and it was found that a one second delay was sufficient to allow the pressure to equilibrate between successive ports. One thousand samples of the voltage from the transducer from a one second measurement period were averaged to determine the pressure at each pressure port. The resulting pressure distribution is shown in Figure 3.12 compared to the higher Reynolds number result of a 24º compression corner at Mach 2.85 found by Settles (1975).

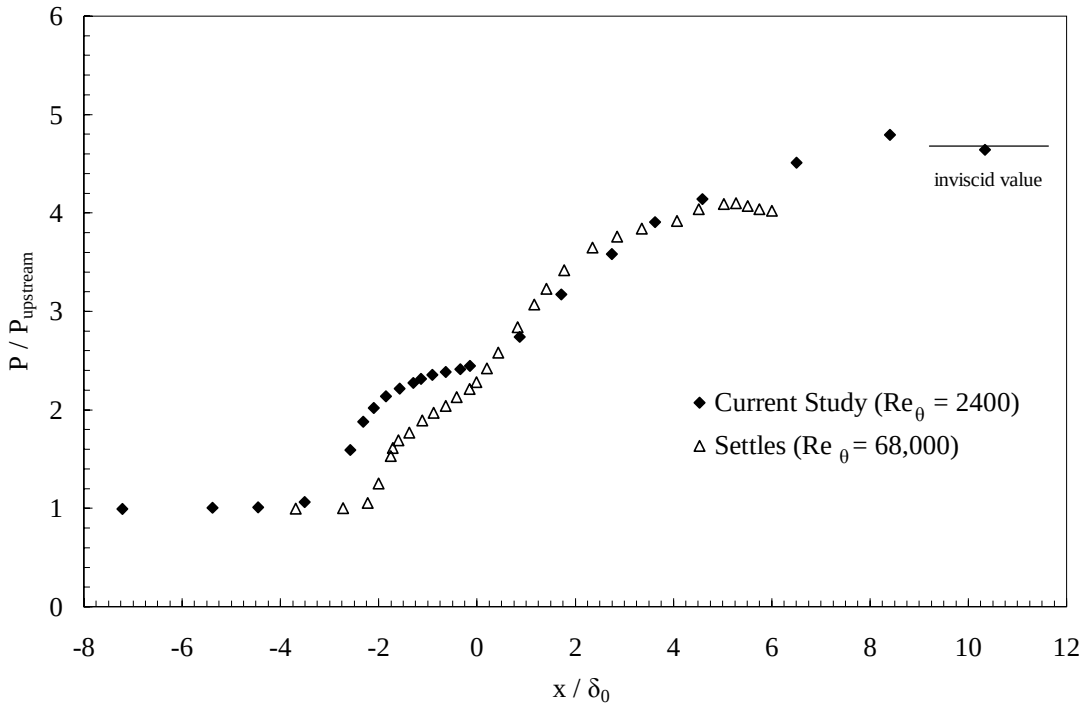

Figure 3.12: 24º compression corner surface pressure distribution at Mach 2.9. The corner location corresponds to $x/\delta_0 = 0$.

The results indicated that the upstream influence of this interaction was larger than that of the higher Reynolds number interaction of the same configuration. By extrapolating the quasi-linear initial pressure rise at separation, the upstream influence, X_U, was found to be 3.4 δ_0 upstream of the corner in good agreement with the surface flow results (3.2 δ_0). The upstream influence for Settles' higher Reynolds number experiments was found to be 2.2 δ_0. The results of the current study also show that the initial pressure rise was stronger than the higher Reynolds number data as the quasi plateau occurs at a higher pressure ratio. The quasi plateau in the pressure profile is also much flatter than the corresponding higher Reynolds number results. The low Reynolds number results closely follow the higher Reynolds number gradual pressure rise downstream of reattachment. Also of interest is the pressure overshoot that occurs at $x/\delta_0 = 8$, after which the pressure

settles to the inviscid value at $x/\delta_0 = 11$. Settles found that the face of ramp model used in his experiments did not extend far enough downstream to capture the full pressure recovery. However, the results of the current study found that total pressure rise and flow turning of this interaction was reached by the end of the model.

3.2.3 Boundary Layer Surveys

Mean Pitot pressure surveys were made at two locations downstream of the corner, which was taken to be the streamwise reference. The surveys took place along the centerline of the 24º wedge model at 2δ and 8δ downstream of the corner. An estimate of the total temperature profile was made by interpolating the profile from the undisturbed boundary layer. The surveys resulted in the velocity profiles shown in Figure 3.13 compared to that of the undisturbed boundary layer.

The profile at $4\delta_0$ downstream of the corner shows that the flow in the boundary

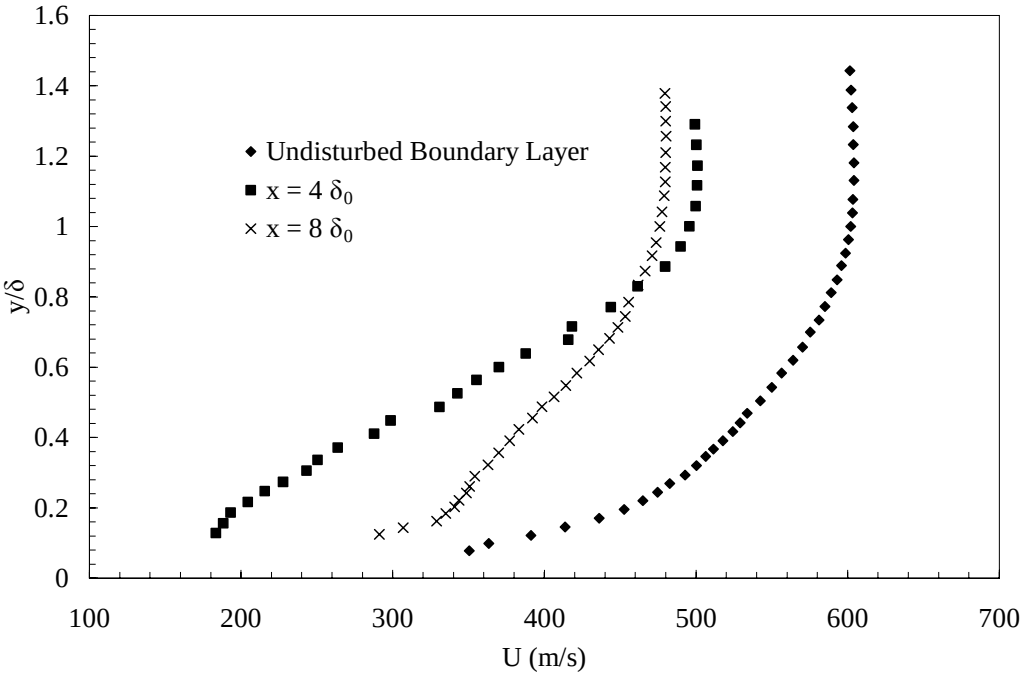

Figure 3.13: Velocity profiles through the Mach 2.9 24º compression corner interaction.

layer was attached but still highly retarded from the separated region, where the velocity profile would have a wake-like shear layer velocity profile. As the flow moved downstream, the profiles taken at 8δ downstream showed a rapid filling out. Close examination of the undisturbed profile and that at 8δ revealed that the flow had not completely recovered. Unfortunately, due to size constraints of the model to avoid tunnel blockage, surveys downstream of $8\delta_0$ were not possible so that the full extent of the recovery zone could not be studied. Also of interest was the relatively gradual decrease in the velocity at the edge of the boundary layer as seen in Figure 3.13. This reflects the gradual pressure rise and flow turning seen from the surface pressure distribution.

3.2.4 FRS Images

FRS images taken in vertical slices through the 24º compression corner interaction are shown in Figure 3.14 and Figure 3.15. The images were selected at random from over 150 images and represent typical instantaneous pictures of the interaction. There are several distinct features in these images that require clarification. As shown in the first image of Figure 3.14, there are two distinct lines in the flowfield. The most upstream diagonal line is the aerodynamic fence used to prevent spillage off the sides of the ramp. The bright regions are a reflection off the fence from the incident laser light on the ramp. We expected the filter to attenuate this light, however repeated attempts to correct the problem failed. The unattenuated light present in these images was believed to be a secondary mode of the laser light, which was later corrected with a major overhaul of the laser. The repairs were not completed in time to present better images. Also, it is

important to understand the loss of signal downstream of the shock. The signal within the boundary layer was seen to persist for several boundary layer thicknesses behind the shockwave, but the contrast quickly fades further downstream because the temperature behind the shock rises to a level greater than the sublimation temperature of the carbon dioxide resulting in a rapid loss of signal. Despite the problems with the laser, many features of the turbulent boundary layer/shock interaction were readily apparent in the images. The shockwave was clearly seen (as labeled in Figure 3.14), forming well ahead of the corner location and indicating the presence of a separated region. In some images, this separation shock was seen to penetrate nearly halfway into the boundary layer. These penetrations seemed to occur through the freestream fluid incursions as well as through some of the turbulent structures. In other images, the shock seemed to wrap around the large scale turbulent bulges. In the initial part of the interaction, the separation shock was seen to lie along the boundary layer edge as the flow went through its initial turning above the separation bubble. In contrast, the reattachment shock was not visible in any of the images, although its effect in strengthening the external shock was seen as the external shock angle increased and moved away from the boundary layer edge. The temperature rise and associated loss of signal behind the shock may be the reason the reattachment shock was not visible. The other possibility is that the reattachment was gradual and resulted in a series of compression waves that were not strong enough to show up in the flow visualization.

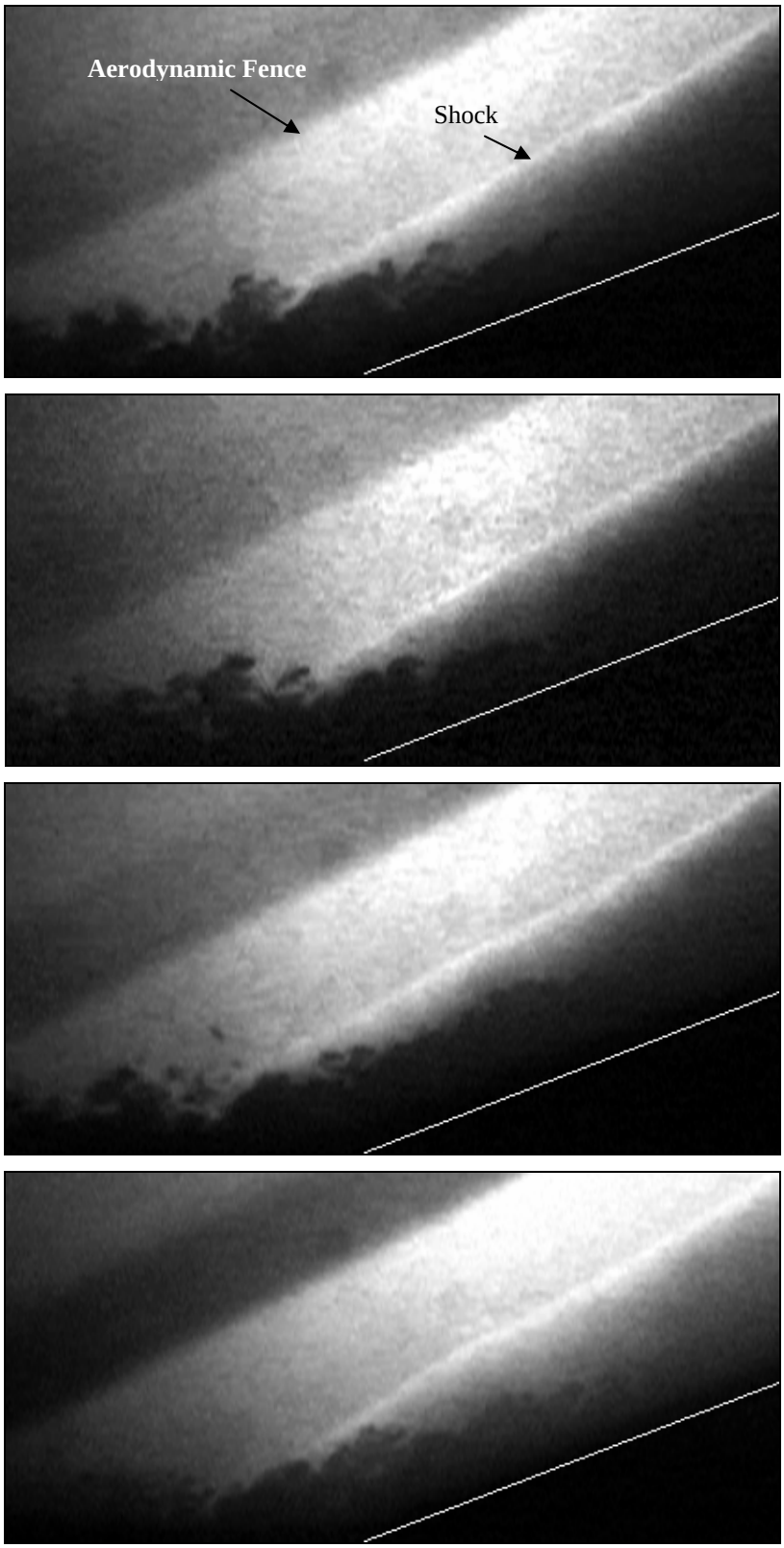

Figure 3.14: FRS images (1) of the 24º compression corner interaction at Mach 2.9, Re_0 = 2400. The bottom of the image represents the wall location and the white line represents the location of the ramp. Field of view is $3.3\delta_0$ x 7 δ_0.

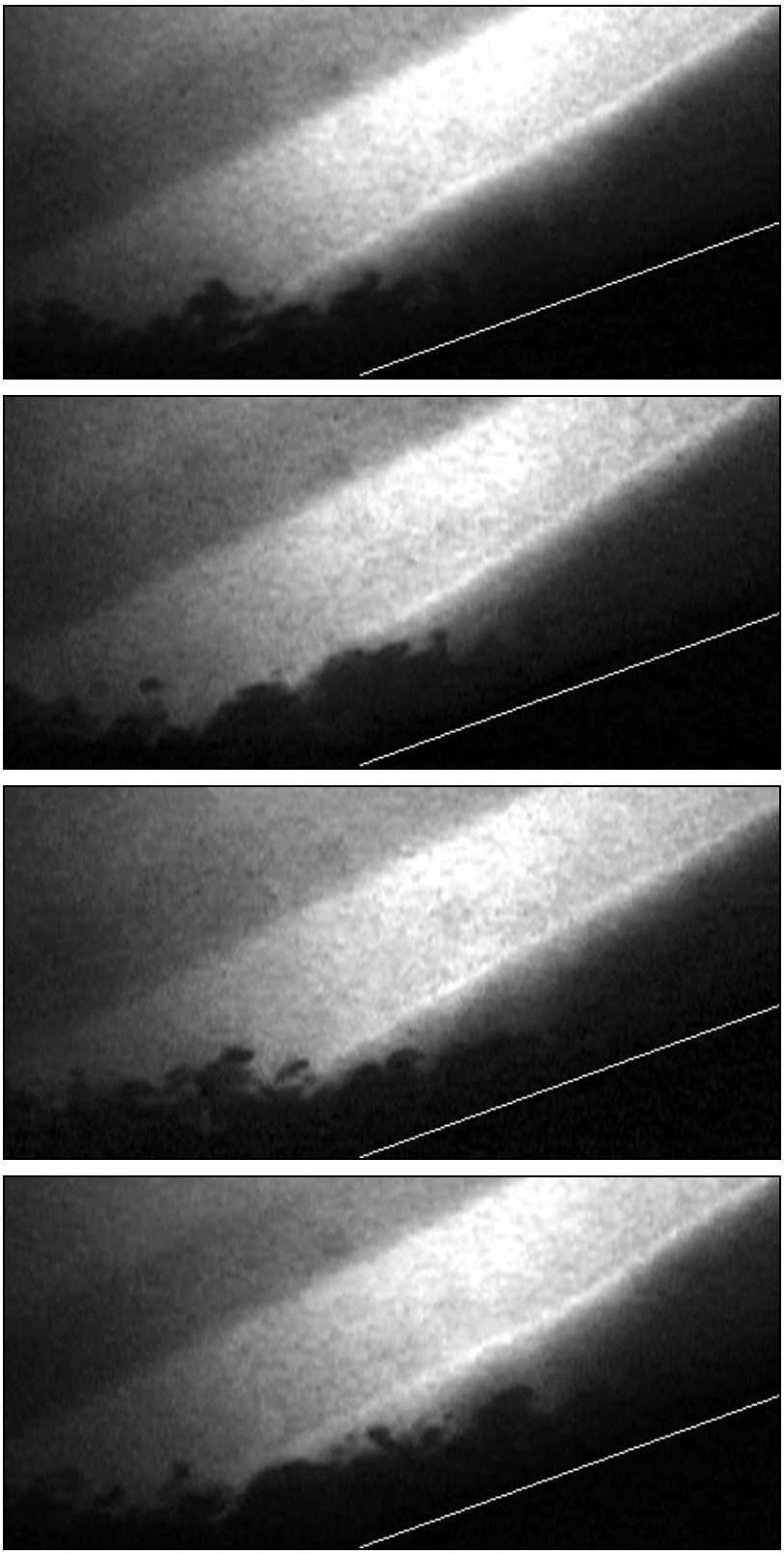

Figure 3.15: FRS images (2) of the 24º compression corner interaction at Mach 2.9, Re_0 = 2400. The bottom of the image represents the wall location and the white line represents the location of the ramp. Field of view is $3.3\delta_0$ x $7\delta_0$.

3.2.5 Intermittency

Because the FRS signal behind the shock deteriorated quickly, analysis from the FRS images was possible only in the region of the interaction upstream of the compression corner. Using the same threshold technique as described for the undisturbed boundary layer, the intermittency was evaluated at two locations in the initial part of the interaction. Two $1\delta_0$ x $1.5\delta_0$ frames were selected from each of the 150 FRS images of the 24º compression corner interaction. The center of these frames were located at x = $-1.5\delta_0$ and x = $-0.5\delta_0$, where the corner location is x = 0 and the coordinate system is as described in the introductory remarks in Chapter 1 of this thesis. The intermittency structure was assumed to have no significant change in the streamwise distance of δ_0 to make the analysis of the intermittency profile. The result of these analyses is shown in Figure 3.16 compared to that of the undisturbed boundary layer.

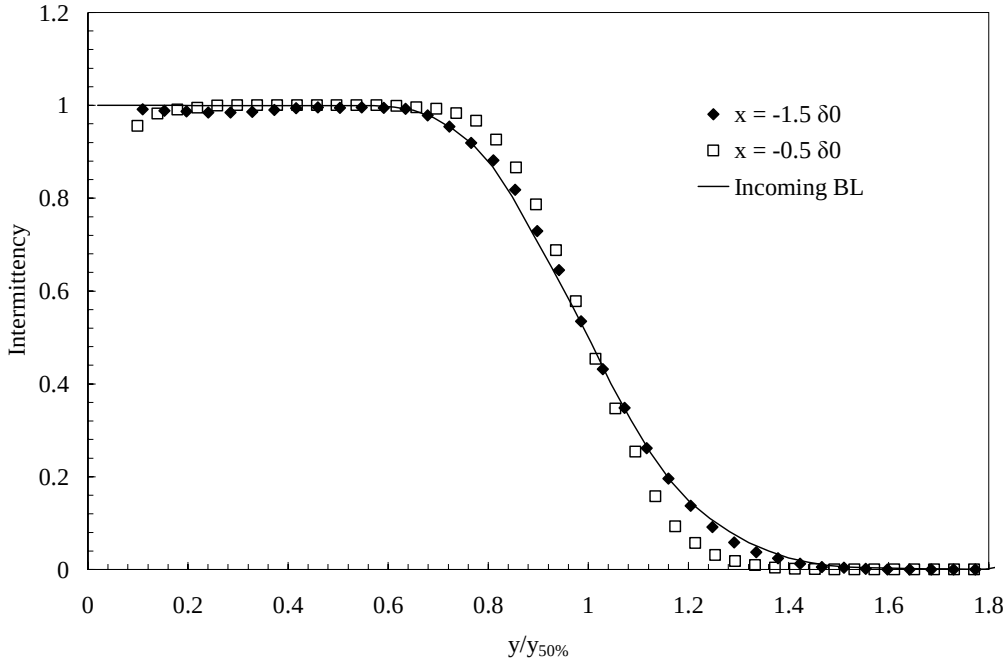

Figure 3.16: Intermittency functions in the initial interaction of Mach 2.9 24º compression corner.

In the previous discussion of the intermittency for the undisturbed boundary layer, the wall normal position was normalized by the boundary layer height δ_0 ($\delta_{99\%}$). Since the local boundary layer thickness was unknown at the locations analyzed in the compression corner interaction, the wall normal position was normalized by the mean position of the interface, where the intermittency reaches 50% ($y_{50\%}$). For the incoming boundary layer, this occurred at $y = 0.8\delta_0$ and increased to $0.85\delta_0$ by $x = -0.50\delta_0$.

3.2.6 Mean Structure Angle

The FRS signal was still strong in the initial part of the interaction just downstream of the separation shock. This allowed for the analysis of the initial interaction region with the correlation method discussed above for the undisturbed boundary layer. The results of the correlations over a streamwise distance of $1\delta_0$, centered $0.5\delta_0$ upstream of the corner are shown in Figure 3.17 where the angles were measured relative to the flat plate. The results would lead one to believe that the orientations of the organized structures in the interaction boundary layer were more upright than those in the undisturbed boundary layer. Since the correlation analysis was taken behind the shock, the initial turning of the flow had already taken place. Measurements of the mean angle of the separation shock were made from correlations with the reference point varied through the estimated shock location. The average angle determined from this study was 28º. This corresponds to a turning angle of 10º for an incoming Mach number of 2.9. This agreed with the measurements of the initial flow turning in previous studies of 24º compression corners at the same Mach number (Smits and Dussauge, 1996). The difference in structure angle shown in Figure 3.17 between the undisturbed boundary layer and initial interaction was about 5-6º. Taking into

account the initial 10º turn of the flow, the average structure angles behind the shock measured relative to the local mean flow were about 4-5º less than those of the undisturbed boundary layer. The large organized structures in the boundary layer seem to lie down when encountering the shock, albeit a small change in average angle.

The overall trend of decreasing angle with decreasing height seen in the undisturbed boundary layer angles was preserved in the initial part of the interaction. This indicated some overall rotation of the structures throughout the boundary layer, although the lack of signal in the lower half of the boundary layer FRS images made it difficult to draw any definite conclusions on the influence on structure angle by the shock. Similar to the undisturbed boundary layer data, at $y/\delta \leq 0.5$, the correlations degraded quickly in the initial part of the interaction; however a few correlations above y/δ of about 0.4 were acceptable.

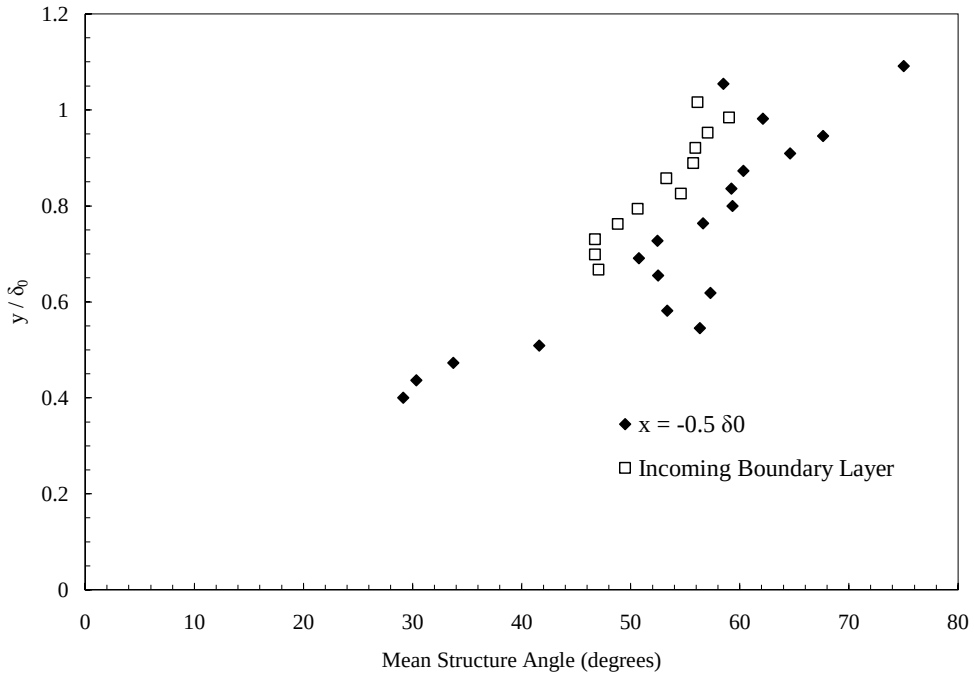

Figure 3.17: Mean structure angles for the 24º compression corner interaction at Mach 2.9, Re_0 = 2400.

3.3 12º Reflected Shock Interaction

The 12º ramp model mounted in the ceiling of the test section generated the shock which impinged on the flat plate boundary layer approximately 330 cm from the leading edge of the plate. Surface oil flow visualization, surface pressure measurements, mean pressure surveys and FRS imaging was used to interrogate the resulting interaction. The shock impingement and reflection was found to create a large fully separated region in the boundary layer.

3.3.1 Surface Flow Visualization

The surface shear stress pattern was visualized using the silicone/graphite mixture described in Chapter 2. The mixture was applied in discrete dots throughout the expected interaction region. A typical visualization is shown in Figure 3.18 showing the highly three-dimensional nature of the interaction with two large counter-rotating vortices present at the surface of the flat plate. The streamwise extent of the separated zone was much larger than the compression corner interaction. At the plate centerline, the streamwise distance from separation to reattachment was 10.5 δ_0. Dupont et al. found the streamwise extent of several reflected shock generators at Mach 2.3, $Re_\theta = 4500$. The largest turning angle, $\alpha = 9.5^o$, produced a streamwise extent of $x = 6.45\ \delta_0$. The results of the current study, $\alpha = 12^o$ agreed well with the trend of increasing distance with increasing shock strength. A schematic drawing of the surface streamline pattern is shown in Figure 3.19. It was hand drawn from the interpretation of four images of the surface pattern from four separate oil flow visualization experiments. Figure 3.19 shows a flattened owl-face of the second kind (Perry and Chong, 1987). The pattern was found to be almost symmetric about the centerline of the plate.

Figure 3.18: Surface flow pattern of the 12º reflected shock interaction at Mach 2.9.

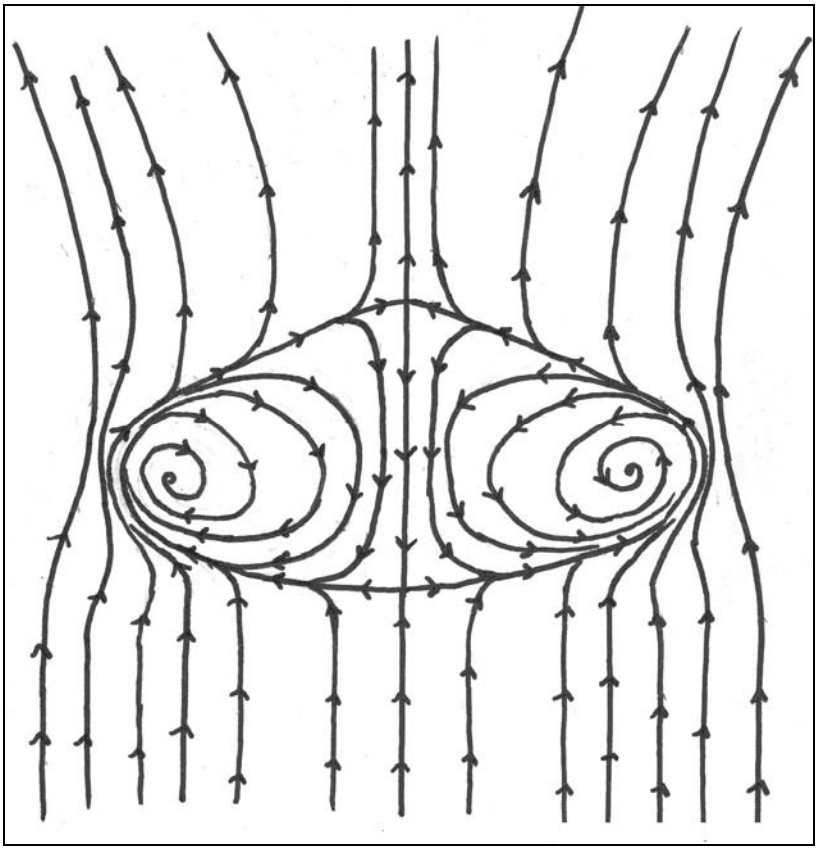

Figure 3.19: Surface pattern schematic of the 12º reflected shock interaction at Mach 2.9.

3.3.2 Surface Pressure Distribution

The surface pressure distribution was measured through the use of 25 static pressure ports installed into the centerline of the flat plate and the compression corner model. The pressure ports were connected to the Scanivalve, and it was found that a one second delay was sufficient to allow the pressure to equilibrate between successive ports. One thousand samples of the voltage from the transducer from a one second measurement period were averaged to determine the pressure at each pressure port. The resulting pressure distribution is shown in Figure 3.20 compared to the profile of the 24º compression corner. The abscissa in Figure 3.20 is the physical location of the pressure measurements for the 24º compression corner. The reflected shock distribution was shifted in the streamwise direction to lay on top of the initial pressure rise of the compression corner distribution for comparison.

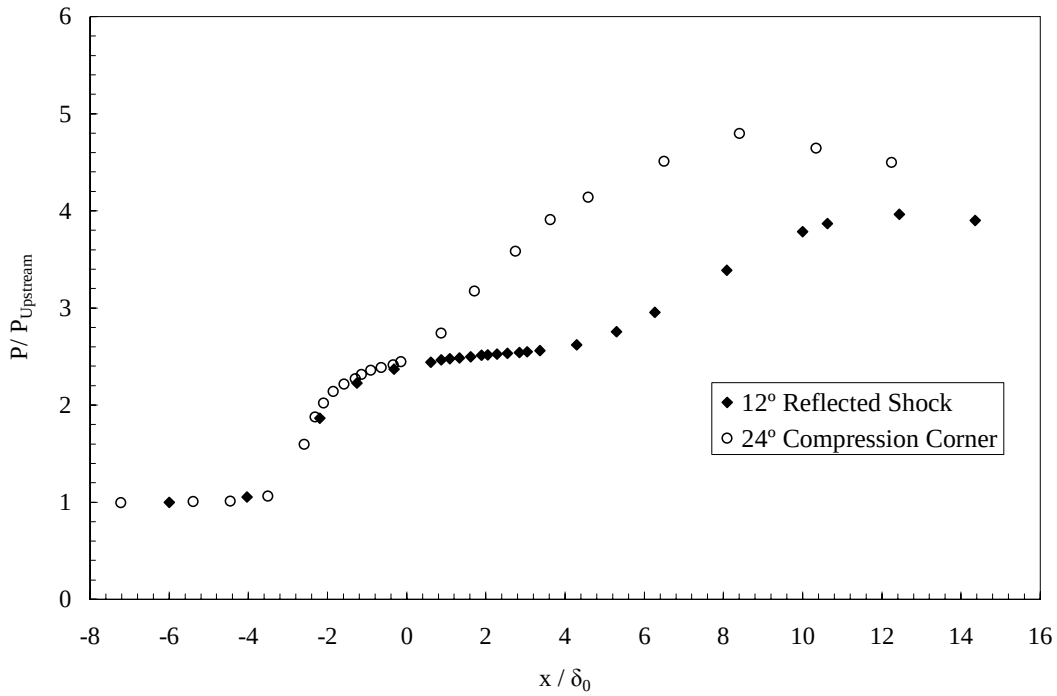

Figure 3.20: Surface pressure distribution for 12º reflected shock interaction at Mach 2.9.

The results showed that the initial pressure rise for both interactions was similar, rising at the same slope and reaching the same value at the plateau. The reflected shock distribution showed a much broader plateau, persisting for about 6 δ_0. The pressure rise after reattachment was more gradual and by the end of the row of pressure taps, the pressure had not risen to the inviscid value.

3.3.3 Boundary Layer Surveys

Due to the lack of a physical reference point such as the corner location used for the 24º compression corner, the flowfield was first imaged using FRS. The images were used to find the mean position of the intersection of the impinging shock and the separation shock, shown in Figure 3.22, which was taken to be the reference point for subsequent analysis. Pitot pressure surveys were conducted on the centerline of the flat plate at two locations downstream of the shock intersection. The resulting boundary layer profiles are shown in Figure 3.21.

It is clear that the flow at $x = 2\delta_0$ downstream of the shock intersection is highly separated with a large extent of the velocity profile exhibiting flow reversal. The Pitot probe was pointed upstream, so the magnitude of the reverse flow shown in Figure 3.21 has no real meaning. However, if we extrapolate a line to the y-axis from the data just outside the region of reverse flow, a good estimate of the size of the separation bubble can be made. The separation bubble height was found to be approximately 6 mm, nearly the same as the incoming boundary layer height. The growth of the boundary layer is evident from the survey at $x = 2\delta_0$, as the profile has not yet reached the freestream velocity at nearly twice the incoming boundary layer height. Similar to the 24º

compression corner interaction boundary layer profiles, the profile taken at $x = 8\delta_0$ shows the rapid filling. The profile had not quite reached the equilibrium shape of the incoming boundary layer, but the height of the boundary layer at $x = 8\delta_0$ had recovered to $\delta_{99} = 6.6$ mm. This location was the furthest possible with the LTVG tunnel's current configuration, so in the context of this study, the recovery of the boundary layer from the reflected shock required over $8\delta_0$ downstream of the intersection of the incident and separation shock.

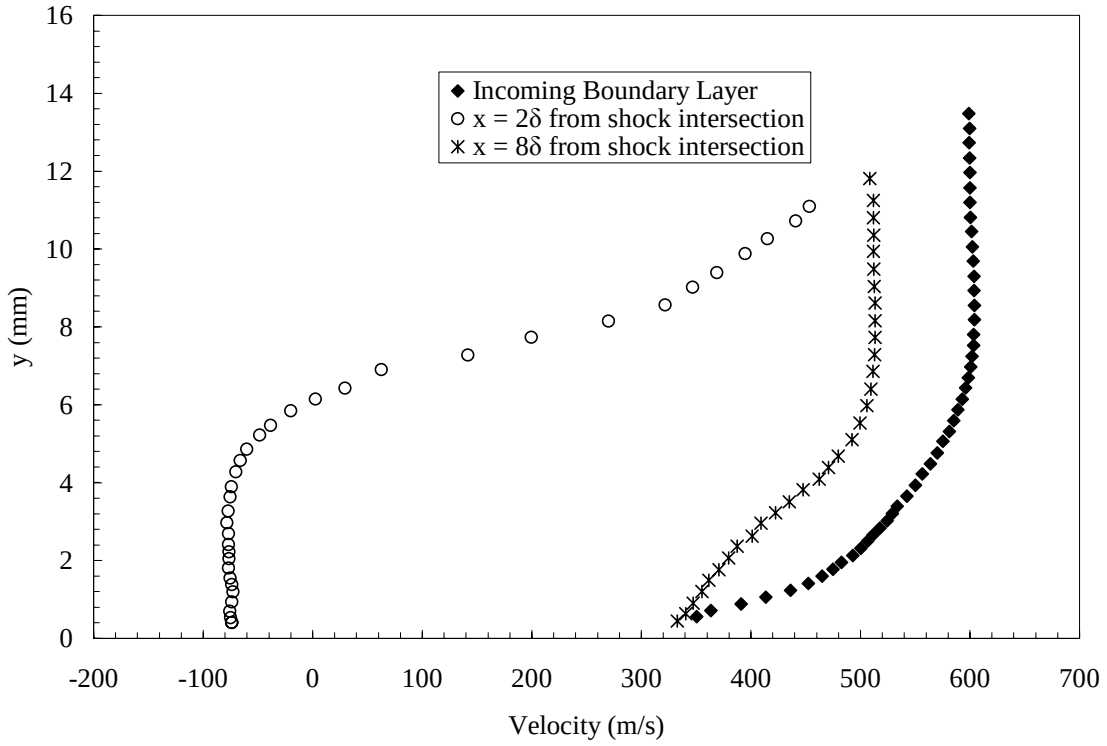

Figure 3.21: Velocity profiles through the 12° reflected shock interaction at Mach 2.9.

3.3.4 FRS Images

Vertical slices through the 12º reflected shock interaction are shown in Figure 3.22 and Figure 3.23. The images were selected at random from over 100 images and represent typical instantaneous pictures of the interaction. Similar to the compression corner images, the signal downstream of the shock system degraded very quickly as the temperature rose above the CO_2 sublimation temperature. The shock system itself was visualized very well, with the separation shock (C_2) forming well ahead of where the incident shock (C_1) would impinge on the flat plate in an inviscid flow. The separation shock intersected the incident shock at point H, which had a mean position of about $2\delta_0$ above the flat plate. This, with the significant boundary layer growth seen in the images, indicated the presence of fully separated flow. The refracted shock (C_3) was seen reentering the boundary layer at about the point where the boundary layer reached its maximum height. The refracted separation shock (C_4) was clearly seen, however, the reattachment shock was lost with the loss of signal behind the initial shock system due to the temperature rise. As with the 24º compression corner interaction, the separation shock was seen to penetrate the large scale structures in the boundary layer in some of the images. In others, the shock seemed to be wrapped around the structure. The position of the shock foot was obtained by extrapolating the separation shock with a straight line to the plate surface. This estimate, while expected to overestimate the location of the shock foot, was found to be about $2.2\delta_0$ upstream of the shock intersection (H).

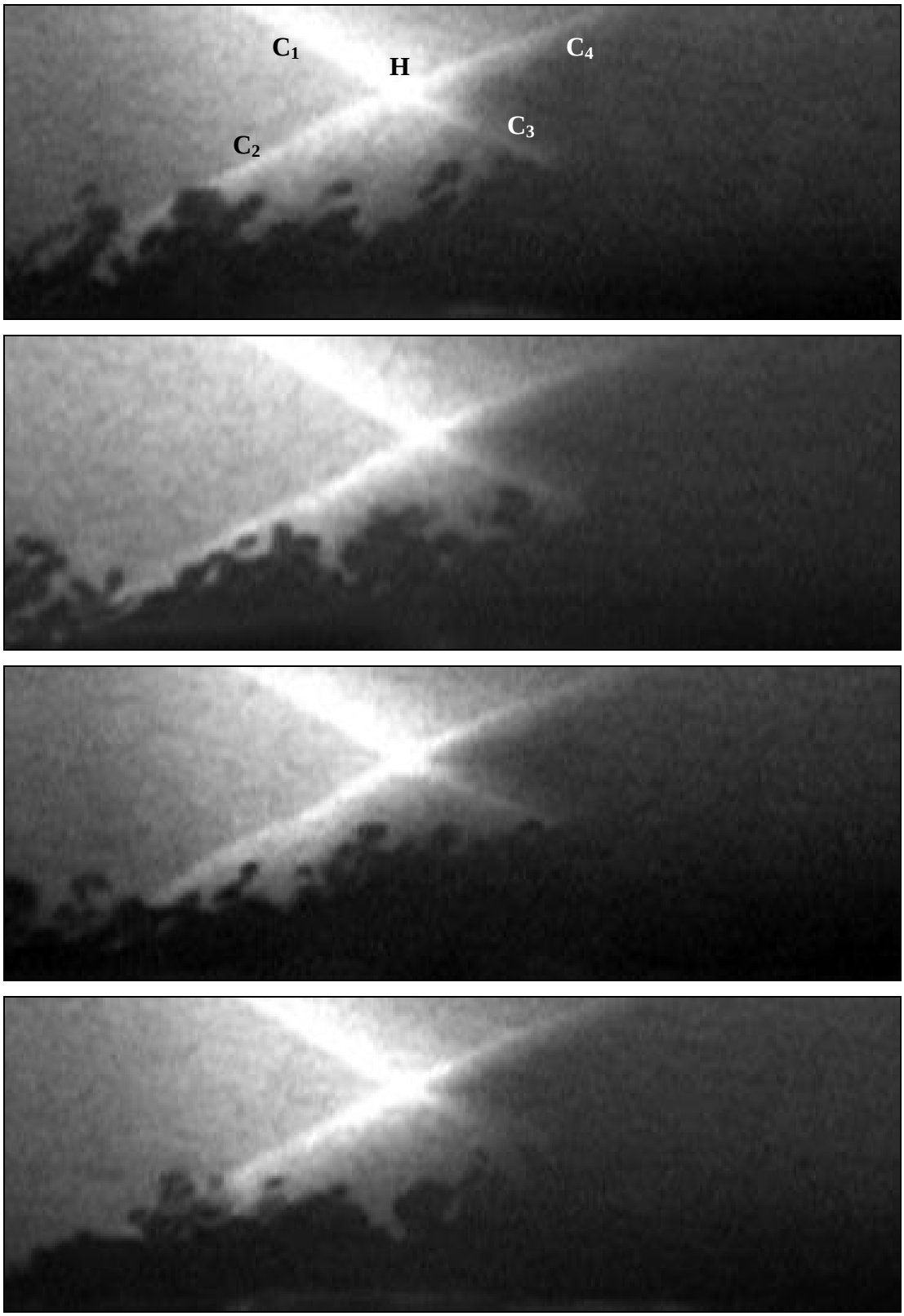

Figure 3.22: FRS images (1) of the 12° reflected shock interaction at Mach 2.9, Re_0 = 2400. The bottom of the image represents the wall. Field of view is $2.3\delta_0$ x $6\delta_0$.

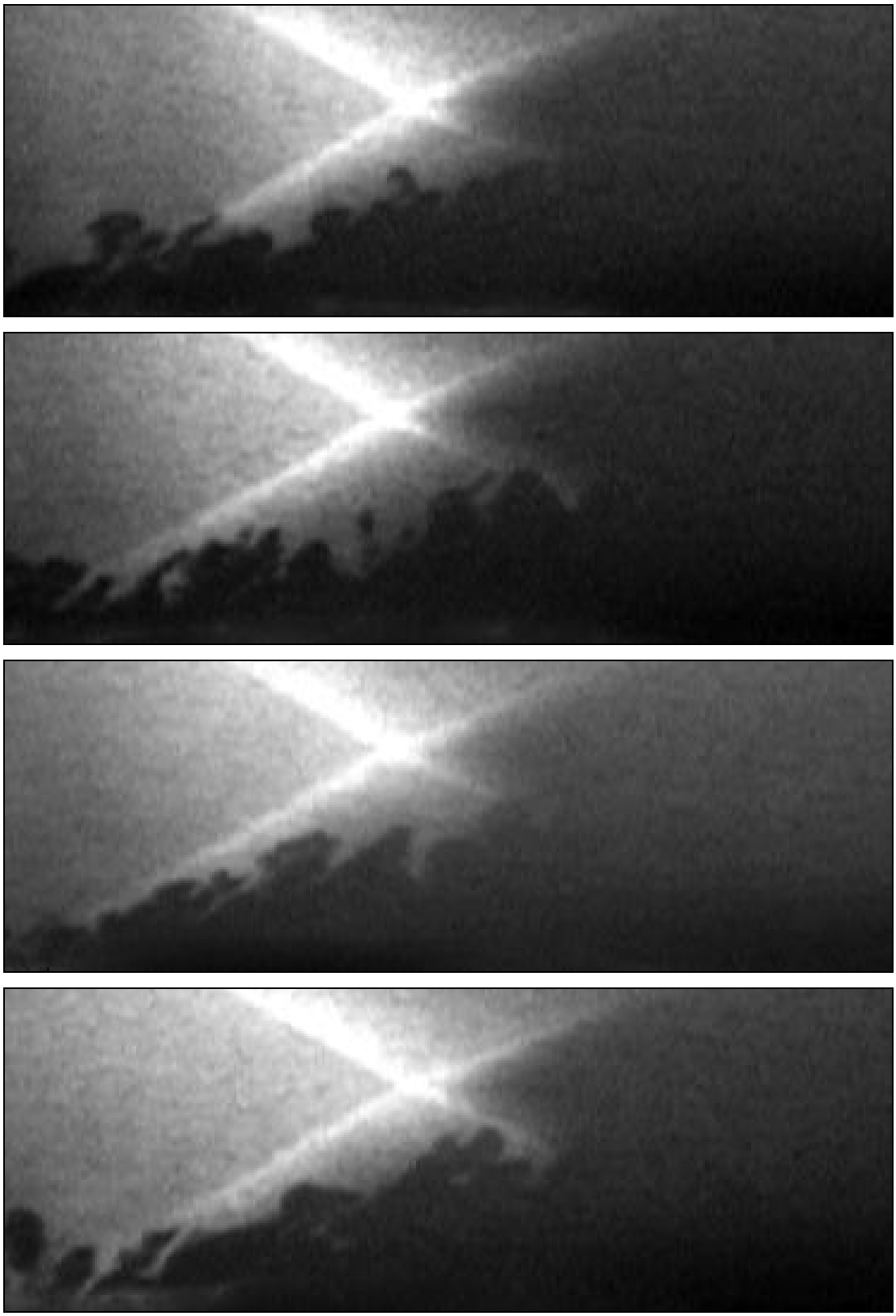

Figure 3.23: FRS images (2) of the 24º compression corner interaction at Mach 2.9, Re_0 = 2400. The bottom of the image represents the wall location. Field of view is $2.3\delta_0$ x $6\delta_0$.

3.3.5 Intermittency

The loss of signal prevented the application of an organized structure analysis downstream of the separation bubble. However, the region just downstream of the separation shock and underneath the shock intersection provided a sufficiently strong signal to which the threshold technique could be applied. Three $1\delta_0$ x $2.2\delta_0$ frames were extracted from the 75 FRS images used for the analysis. The larger wall normal extent of the frame was required to capture the growth of the boundary layer over the separation bubble. The intermittency profiles resulting from the threshold technique are shown in Figure 3.24.

The intermittency profile exhibited the similar behavior to that found in the compression corner. The profile became slightly steeper than the upstream boundary layer through the initial part of the interaction at $x = -1.5\ \delta_0$. The profiles further downstream at $x = -0.5\delta_0$ showed an even steeper shape while the intermittency profile at $x = 0.5\delta_0$ showed no more significant change. The mean position of the interface ($y_{0.5}$) increased rapidly through the interaction. The mean position of the interface for the incoming boundary layer was $y/\delta_0 = 0.77$. The $y_{0.5}$ location was seen to rise by 4%, 33% and 59%, respectively for the three streamwise positions examined in Figure 3.24. The most downstream intermittency profile revealed the mean position of the boundary layer interface height to have increased to $y/\delta_0 = 1.25$. The rapid growth in the interface position quantified the rapid boundary layer thickness growth seen in the FRS images as the flow was displaced by the separation bubble.

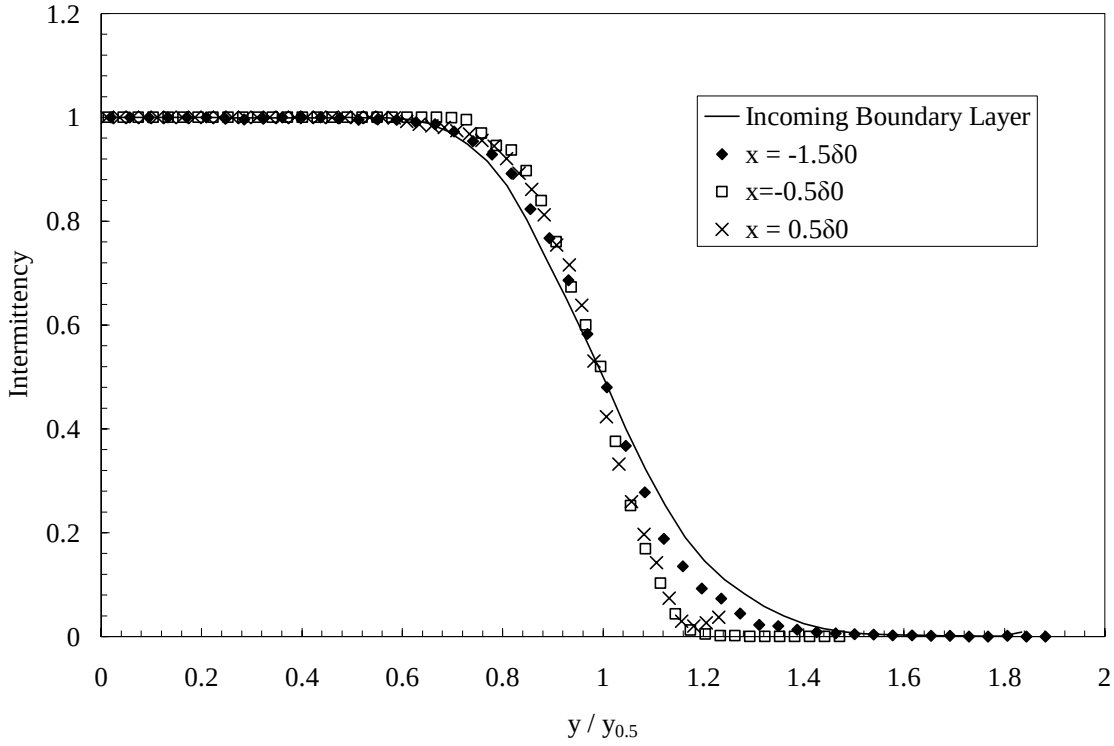

Figure 3.24: Intermittency profiles for the 12° reflected shock interaction, Mach 2.9, Re_0 = 2400.

3.4 Summary

This chapter has detailed the experimental results for the study of two shock/turbulent boundary layer interactions at Mach 2.9. Data acquisition/reduction procedures were described with a discussion of the resulting information. The main results of the Mach 2.9 experiments were as follows:

1. The incoming boundary layer appeared to be fully turbulent with the mean Reynolds number based on momentum thickness estimated to be 2400.
2. For the incoming boundary layer, the angles of large scale structures relative to the flat plate surface measured from correlation analysis compared well to the

angles determined from hot-wire anemometry at much higher Reynolds number (Re_θ = 80,000).

3. The intermittency of the incoming boundary layer was similar to the profile of an incompressible turbulent boundary layer.
4. The initial pressure rise in the 24º compression corner interaction was greater than higher Reynolds number interactions with a flatter pressure plateau in the separated region. The upstream influence was found to start at $x = -3.4\ \delta_0$.
5. In the 24º compression corner interaction, the flow separated at $x = -3.2\ \delta_0$ and reattached at $x = 1.6\ \delta_0$, indicating a broader separated region than higher Reynolds number flows ($-2.2\ \delta_0$ to $0.8\ \delta_0$).
6. Large structures in the boundary layer appeared to decrease their angle relative to the wall in response to the initial compression in the 24º corner interaction. The intermittency of the boundary layer showed a slight increase in steepness, but varied little in the initial interaction.
7. The 12º reflected shock interaction was found to be fully separated with the height of the separation bubble approximately equal to the mean boundary layer height. FRS images revealed the shock system elevated above the boundary layer height, with the separation shock forming about two boundary layer thicknesses ahead of where the inviscid shock would have impinged on the flat plate.
8. The surface pattern revealed the 12º reflected shock interaction to be highly three-dimensional with two counter-rotating vortices.

9. The surface distribution for the 12º reflected shock interaction showed an initial pressure rise similar to the 24º compression corner but with a much broader plateau. The separated region occurred over a spanwise distance of 10.5 δ_0.
10. The intermittency profile for the reflected shock revealed a slight steepening of the profile through the separated region and showed the significant boundary layer growth reflected in the mean position of the interface increasing by as much as 60%.

Chapter 4 Mach 8 Experiments

In the previous chapter, the interaction of a turbulent boundary layer and shockwave were investigated at the supersonic Mach number of 2.9. In this chapter, the discussion moves to the hypersonic flow regime where the results of studies on an 8º compression corner and a 10º sharp fin interaction at Mach 8 are presented. Included here are the results of mean flow surveys, surface oil flow visualization, and FRS flow visualization of the undisturbed boundary layer and both shock interactions.

4.1 Undisturbed Boundary Layer

An independent analysis of the undisturbed boundary layer was not undertaken in this study. The undisturbed boundary layer on a flat plate at Mach 8 in the HyperBLAF was studied extensively by Baumgartner (1997) using the same models used in the current study. A summary of the undisturbed boundary layer results of Baumgartner are presented here for completeness. The test conditions used by Baumgartner and summarized here were replicated as closely as possible in the experiments of the current study. Therefore, the conditions summarized here for the undisturbed boundary layer were assumed to be the same for the incoming boundary layer in the interactions of the current study.

4.1.1 Mean Flow Surveys

The undisturbed boundary layer studied by Baumgartner developed on the flat plate described in Chapter 2 with nominal tunnel operating conditions P_0 = 1000 psia and T_0 =

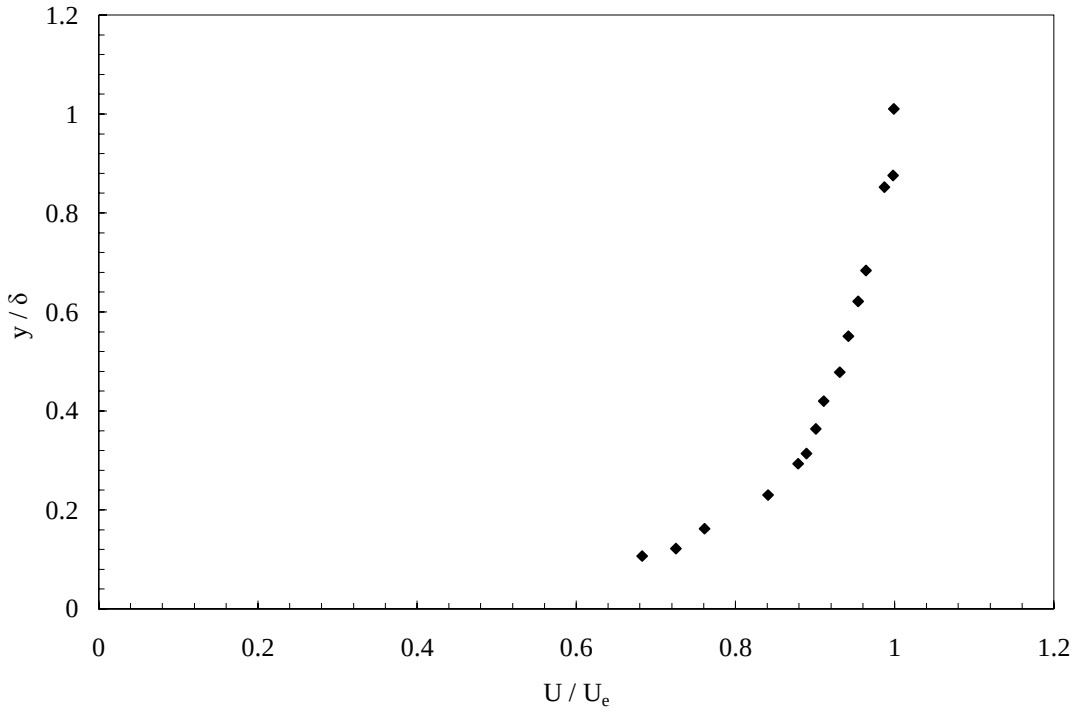

Figure 4.1: Mean velocity profile for the undisturbed boundary layer at Mach 8, Re_θ = 3500. From Baumgartner (1997).

780 K. The mean flow surveys were taken using the same combined Pitot and total temperature probe used in the Mach 2.9 experiments. Surveys were conducted on the plate centerline, 36 cm downstream of the leading edge. The mean velocity profile non-dimensionalized by outer variables is shown in Figure 4.2.

Figure 4.2 shows a log-linear plot of the experimentally derived effective velocity profiles non-dimensionalized using the van Driest transformation. The wall shear stress, τ_w, was obtained by Baumgartner using the Clauser chart method and used to non-dimensionalize the data shown in Figure 4.2. The profile reveals the boundary layer to be fully turbulent with a logarithmic region and small wake. Baumgartner found the mean strength of the wake component ($\Delta u/u_\tau$) to be approximately 1.0 at a Reynolds number based on momentum thickness (Re_θ) of approximately 3500.

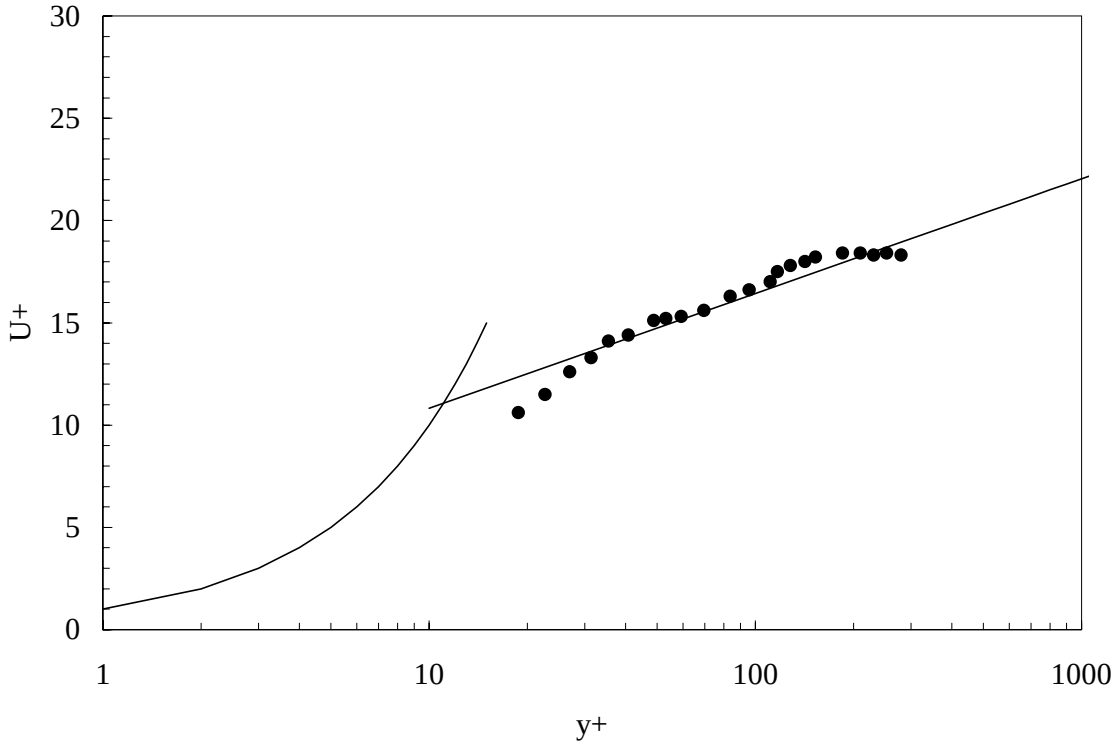

Figure 4.2: Velocity profile of the undisturbed boundary layer at Mach 8 transformed according to van Driest using the Clauser method for wall shear stress. From Baumgartner (1997).

Characteristic Scales

Table 4.1 gives the characteristic scales and ratios for the undisturbed boundary layer at Mach 8 averaged from three independent surveys: boundary layer thickness δ, displacement thickness δ^*, momentum thickness θ, shape factor $H \equiv \delta^*/\theta$, the Reynolds Number based on momentum thickness Re_θ, the skin friction coefficient C_f, and the friction velocity $u_\tau = \sqrt{\tau_w / \rho_w}$.

δ_{99} (mm)	δ^* (mm)	θ (mm)	$H = \delta^*/\theta$	Re_θ	$C_f \times 10^3$	u_τ (m/s)
11.5 ±2%	5.96 ± 5%	0.21 ±15%	28.4	3500 ±13%	0.72 ±10%	72.7

Table 4.1: Characteristic scales of the undisturbed boundary layer at Mach 8. From Baumgartner (1997).

4.1.2 FRS Images

Baumgartner extensively visualized the Mach 8 undisturbed boundary layer using FRS. Streamwise cross-sectional views were obtained by introducing the laser sheet normal to the plate surface. More specific descriptions of the experimental setup for these imaging techniques were described by Baumgartner (1997). The basic concepts of FRS imaging are the same, with small variations in experimental setup from the current study as shown in Chapter 2.

Figure 4.3 are visualizations of the hypersonic undisturbed boundary layer obtained using FRS imaging, selected at random from over 100 images. The run conditions were similar to those reported for the velocity profile surveys described in the Section 4.1.1.

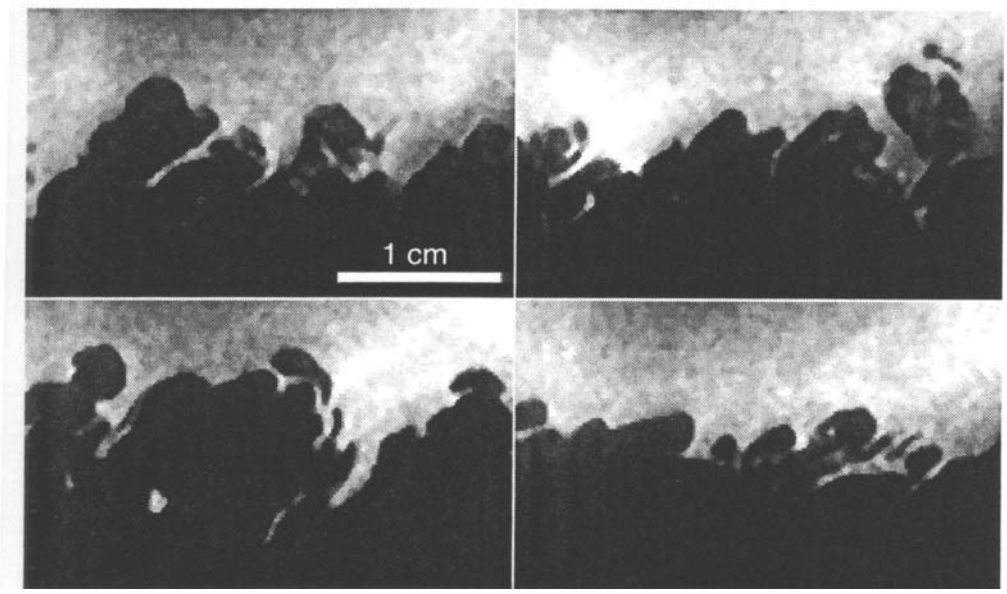

Figure 4.3: Streamwise vertical slices through the undisturbed boundary layer at Mach 8, Re_θ = 3500. The field of view is 1.5δ x 2.5δ where the wall location corresponds to the bottom of each image. Flow is from left to right. From Baumgartner (1997).

The images were qualitatively similar to those obtained for the undisturbed boundary layer at Mach 2.9. Large incursions of freestream fluid were seen deep into the boundary layer with large scale turbulent bulges extending beyond the mean boundary layer edge. The characteristic downstream lean of the large structures was evident, which was examined quantitatively by Baumgartner and is summarized in Section 4.1.4.

4.1.3 Intermittency

The intermittency function of the Mach 8 undisturbed boundary layer was computed by Baumgartner from approximately 50 images similar to those shown in Figure 4.3. The same threshold technique applied to the Mach 2.9 boundary layer was used to find the fraction of turbulent fluid present at various heights in the boundary layer. In this case, the optimum threshold pixel value was found to be 100. The results of this analysis are shown in Figure 4.4. Offered for comparison are the incompressible curve from White (1991) and an analysis of the undisturbed boundary layer just upstream of the 8º compression corner interaction of the current study. A 1.5δ x 2δ section immediately upstream of the corner was taken from each of 80 FRS images of the compression corner interaction, which will be shown in Section 4.2. The results from this analysis compare very well to Baumgartner's data, with only a small disagreement in the range of $0.4 \leq y/\delta \leq 0.7$ which is most likely due to the difference in resolution of the images. The field of view for the compression corner images was much bigger in order to capture the extent of the interaction, so the resolution of the undisturbed boundary layer was less than those used by Baumgartner. Both data sets followed the incompressible curve closely.

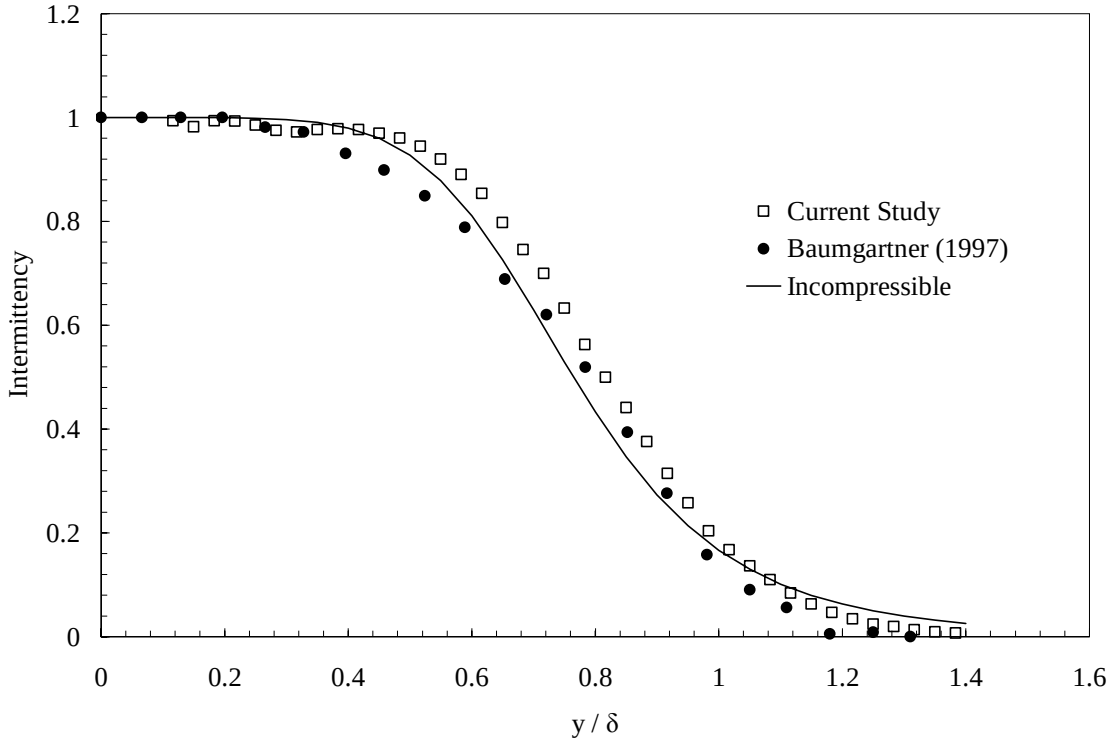

Figure 4.4: Intermittency function for the Mach 8 undisturbed boundary layer comparing the data of the current study to Baumgartner and the incompressible curve fit.

4.1.4 Mean Structure Angle

Correlations, as described in Section 3.1.3, were performed on an ensemble of 420 frames of the streamwise slices through the boundary layer. Baumgartner used these correlations to quantify the mean structure angle throughout the boundary layer with the reference point at 24 different heights. He found the mean angle of the ellipses fitted to isocorrelation contours in the range [0.6, 1.0], and the results are shown in Figure 4.5. A correlation analysis was performed on the same undisturbed portion of the boundary layer just upstream of the 8º compression corner images (Figure 4.7) used to compare the intermittency profile to Baumgartner's data. Ellipses were fit to the isocorrelation contours in the range [0.5, 0.8]. The resulting large-scale structure angles are shown in

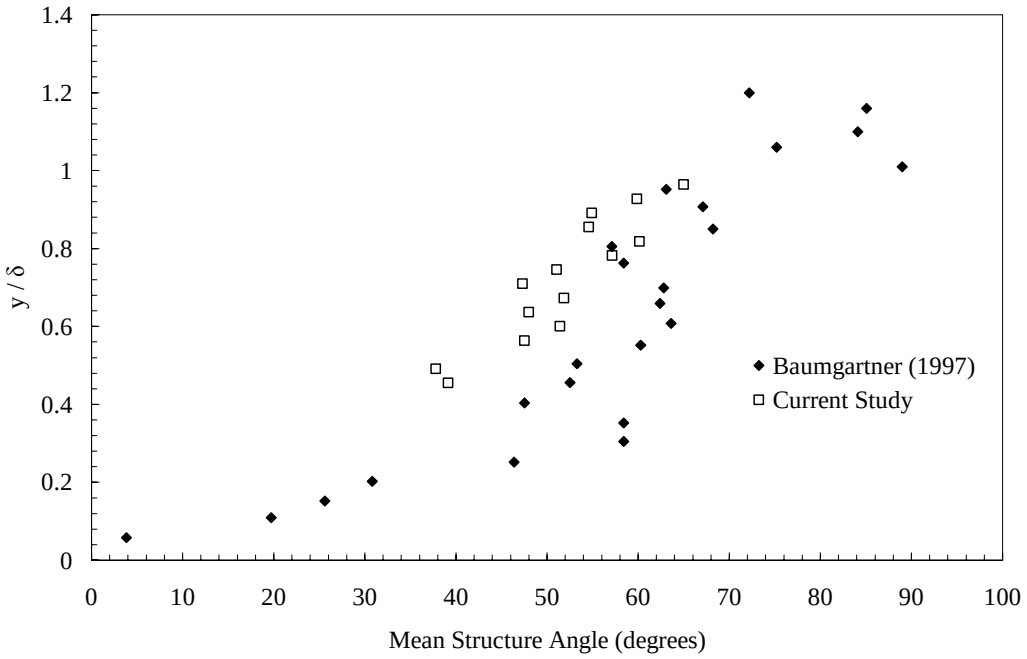

Figure 4.5: Mean structure angles for the undisturbed boundary layer at Mach 8.

Figure 4.5. The structure angles from the current study showed broad agreement with the results of Baumgartner (1997).

4.2 8º Compression Corner Interaction

Surface oil flow visualization and FRS imaging were used to study the 8º compression corner interaction. In order to duplicate the incoming boundary layer characteristics of Baumgartner, the operating conditions were replicated as closely as possible. The incoming properties to the interaction were assumed to be the same. The visualizations revealed the flow remained attached through the interaction with a highly inclined shock deeply immersed in the boundary layer.

4.2.1 Surface Flow Visualization

The Dow Corning 200 silicone fluid and titanium dioxide mixture was applied to the surface of the flat plate and ramp model in six spanwise rows of small dots. Three rows were applied ahead of the corner and three rows downstream of the corner with a plastic syringe. The tunnel was run as described in Chapter 2 and the oil flow was captured on video. The camera images were converted to digital media and still images were grabbed from the video files. An image of the surface oil flow taken from the video just before tunnel shutdown is shown in Figure 4.6. Some features of this photograph need to be pointed out for clarification. Feature A was the shadow cast by the window from the illumination source used to brighten the test section. Feature B points out the "spilling" of the flow off the edges of the ramp. Feature C was the corner location and D

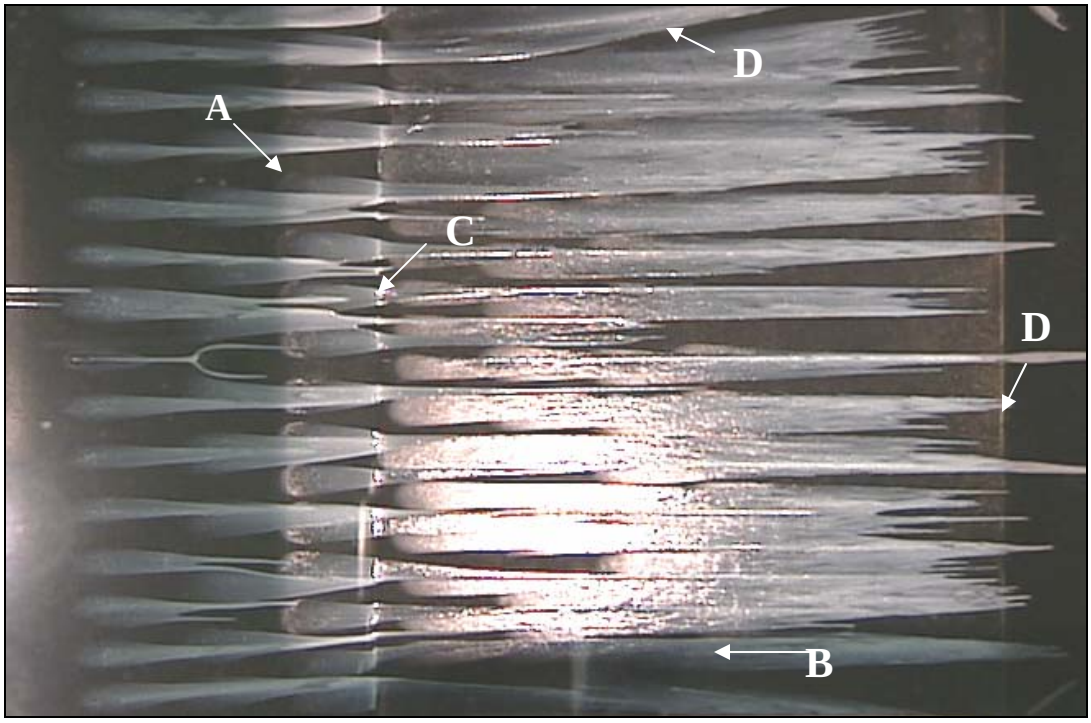

Figure 4.6: Surface oil flow visualization of the 8° compression corner at Mach 8, Re_0 = 3500. Flow is from left to right with the corner location as noted in the image.

was the apex of the wedge model where the flow turns 8º to become parallel to the incoming flow. The flow is from left to right in Figure 4.6.

The parallel and straight surface lines indicated that the incoming flow was highly two-dimensional over a 10δ wide region in the spanwise direction. Figure 4.6 also reveals no indication of separated flow, which would be marked by a build up of the oil mixture at the stagnation point where flow reversal would begin. There was no indication of a separation point as the surface lines seem very continuous up to and beyond the corner location. Analysis of the video showed that the row of dots immediately upstream of the corner location flowed continuously through the corner without stopping or reversing direction. The oil flow slowed down as it neared the corner and once past the corner accelerated up the ramp. This behavior reflected the wall shear stress decreasing as the flow approaches the corner, and then increasing downstream of the corner without going to zero which would have indicated the point of separation. Evidence from video and still images indicates that separation did not occur in the 8º compression corner interaction.

4.2.2 FRS Images

The 8º compression corner interaction was visualized in a similar manner to the 24º compression corner interaction at Mach 2.9. The laser sheet was aligned in the streamwise direction on the spanwise centerline of the flat plate and ramp model. The flow was visualized in two locations: one which included the incoming boundary layer and about 5δ downstream of the corner; and the other which concentrated attention on the full 8δ extent of the ramp. FRS images, selected at random from stacks of 100+ images, of the 8º compression corner interaction are shown in Figure 4.7 and Figure 4.8.

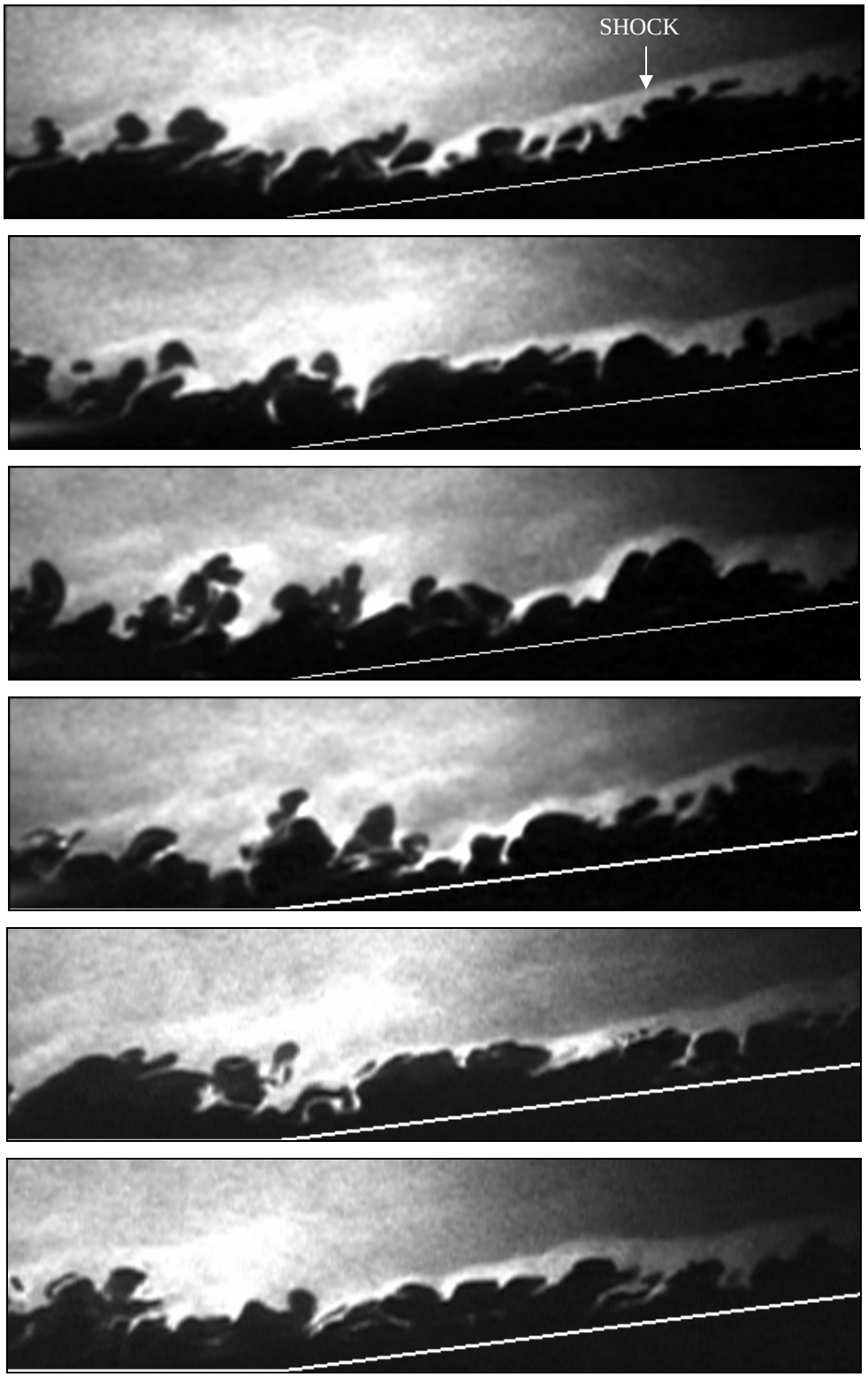

Figure 4.7: Instantaneous FRS images (uncorrelated) of the Mach 8 8º compression corner interaction at the first location. Images are $1.7\delta_0$ x $6\delta_0$. The bottom of each image corresponds to the flat plate location and the white line indicates the surface of the ramp model.

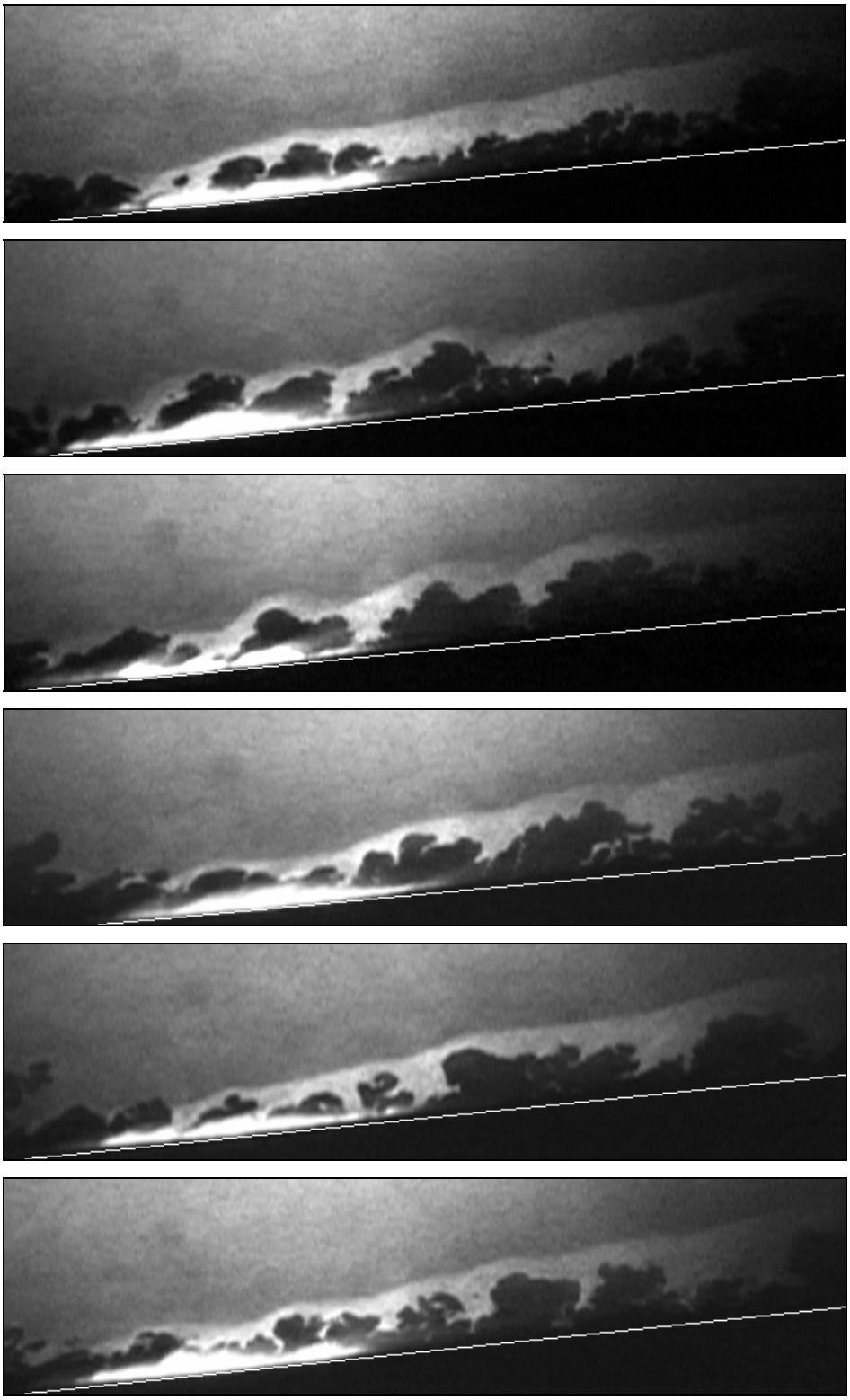

Figure 4.8: Instantaneous FRS images (uncorrelated) of the Mach 8 8º compression corner interaction at the second location (further downstream). Images are $2.5\delta_0$ x $8\delta_0$. The bottom of each image corresponds to the flat plate location and the white line indicates the surface of the ramp model.

The images in Figure 4.7 confirmed that the flow remained attached through the interaction as there seemed to be only one main shockwave that is attached to the corner location. The shock was seen to be deeply immersed in the boundary layer for several boundary layer thicknesses and highly distorted by the passing of large scale structures. The shock, in some cases mainly close to the corner, seemed to be piercing the large structures in the boundary layer. In most images, as shown in Figures 4.7 and 4.8, the shock was wrapped around the edges of the largest structures in the flow. When the structure height was below the mean shock line, the shock was fairly uniform with a shock angle close to that predicted by inviscid theory. Significant shock distortion was seen as far as 6-7δ downstream of the corner although less frequent as the shock height above the ramp increased with streamwise distance from the corner. Figure 4.7 also showed clear evidence of shocklets, where shocks emanated from large scale motions in the boundary layer upstream of the corner. Another distinctive qualitative feature of the boundary layer downstream of the corner was the apparent increased angle of the large scale structures. The structures seem to be much more inclined than the corresponding structures in the undisturbed boundary layer when referenced to the local surface direction. A qualitative analysis of this apparent difference was undertaken through the use of correlations and is discussed in Section 4.2.4.

4.2.3 Intermittency

In order to investigate the effect of the hypersonic compression on the organized structures in the boundary layer, the intermittency function was explored at successively increasing distances downstream of the corner location. Images from both FRS sets

represented in Figures 4.7 and 4.8 were used to compile the data. Five $1\delta_0$ x $1.2\delta_0$ frames were extracted from 100 images downstream of the corner. The flow was assumed to remain unchanged in regions δ_0 wide in the streamwise direction. The frames were subjected to the threshold method described above and the resulting intermittency functions are shown in Figure 4.9 with wall normal position normalized by the location of half intermittency, $y_{0.5}$. The results showed no significant change from the intermittency profile of the undisturbed boundary layer. The slight differences in the profiles were most likely the effect of the subjective nature of the threshold technique. The data shown here are from three different sets of FRS images. Although great care was taken to reproduce the laser intensity and flow seeding, the contrast from image set to image set varied. Therefore, the threshold level was not the same and had to be determined for each frame of each image set. Despite this subjective effect, the results showed no significant change through the 8º compression corner interaction at Mach 8 when taken qualitatively.

As with the Mach 2.9 intermittency profiles, the wall normal position was normalized by the location of half intermittency, $y_{0.5}$. For the undisturbed boundary layer, this occurred at $y/\delta_0 = 0.79$. The profiles downstream of the corner reached half intermittency at approximately the same height, varying ±5% which was within the uncertainty of the threshold method.

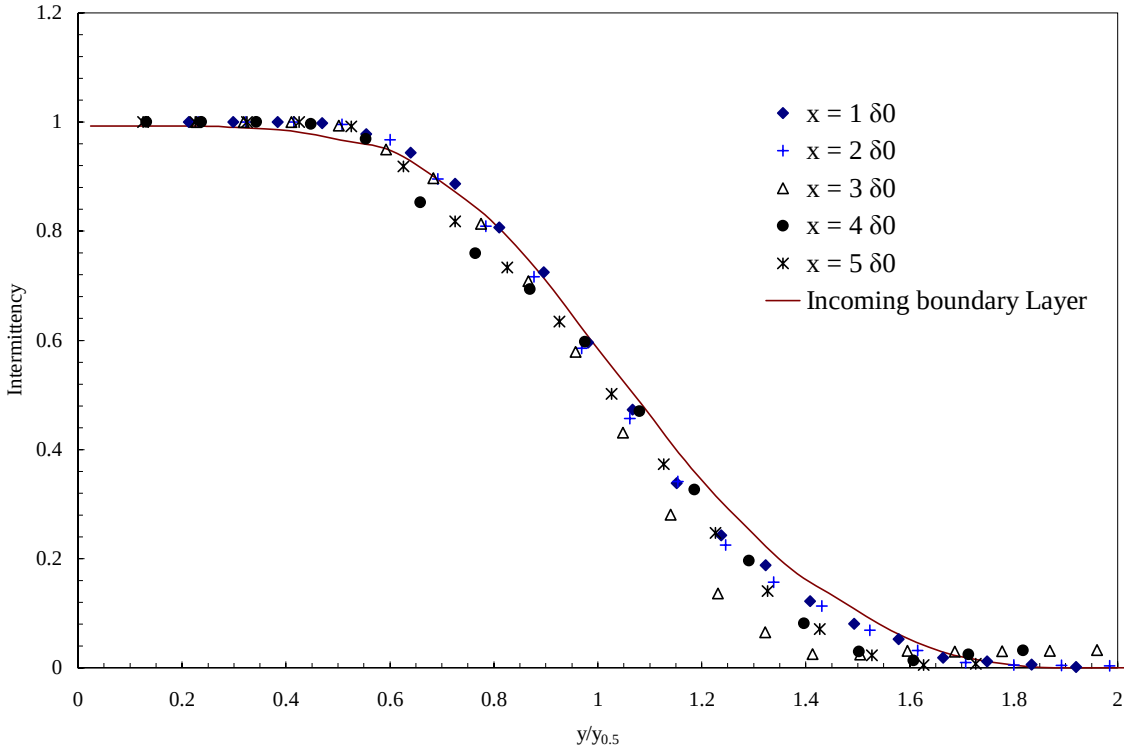

Figure 4.9: Intermittency function profiles downstream of 8° compression corner at Mach 8, Re_0 = 3500.

4.2.4 Mean Structure Angle

Correlations were made at the same downstream positions described above for the intermittency function. As shown in the FRS images, the shock was deeply entrained in the boundary layer, its location indicated by the interface in front of a region of increased brightness in the irrotational freestream fluid. The interface was extremely unsteady and its position varied greatly especially in the first three downstream positions. The effect of the deep penetration and unsteadiness of the shock was to distort the correlation images so much that fitting of ellipses to isocorrelation contours created unrealistic results, sometimes negative angles. However, the images of the furthest downstream position, x

= $5\delta_0$, revealed that the shock was sufficiently elevated above the boundary layer edge that the shock interface had little effect on correlations. Ellipses were fit to isocorrelation contours in the range [0.5, 0.8] and the angle of the major axis to the ramp surface was measured, resulting in the data shown in Figure 4.10. The results were somewhat scattered, but indicated a general trend that the mean structure angle decreased downstream of the hypersonic compression. Analysis of the data showed the greatest decrease in angle at a given height in the boundary layer to be about 18º, with an average decrease of about 11º over the spread of the data. The trend of increasing inclination of the structures was preserved downstream with what seems to be an overall reduction in angle throughout the boundary layer in the wall normal direction.

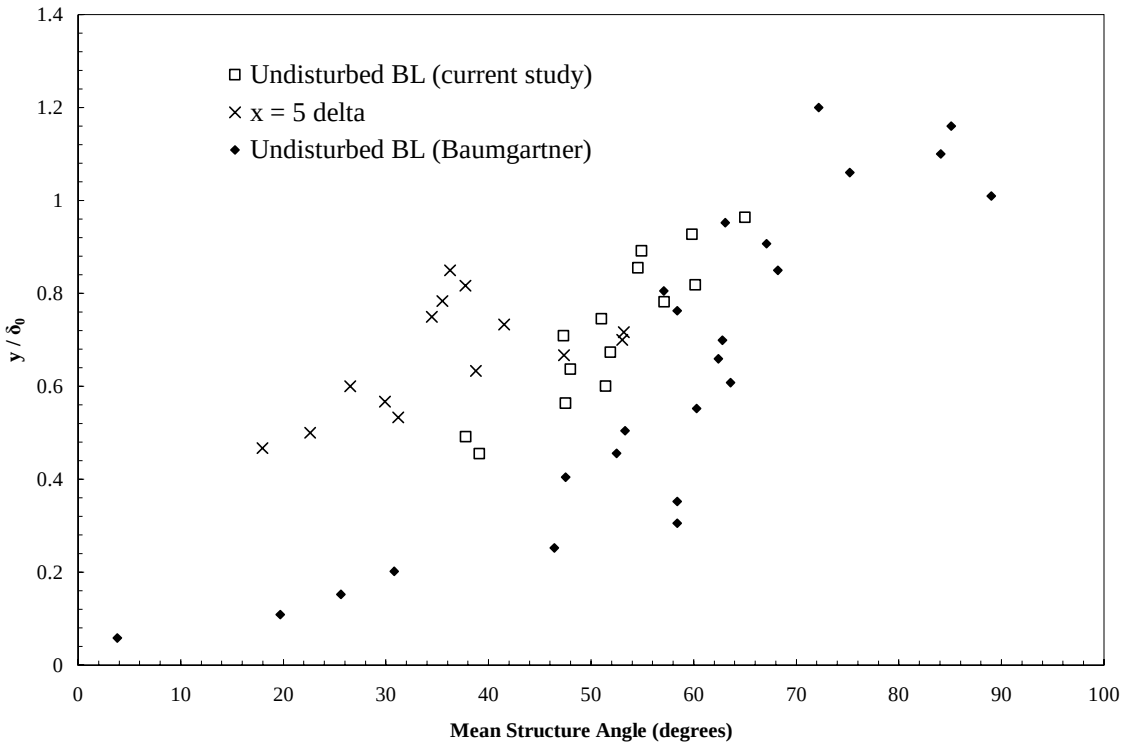

Figure 4.10: Mean structure angle through 8º compression corner interaction at Mach 8, Re_0 = 3500.

4.3 10º Sharp Fin Interaction

Surface oil flow visualization and FRS imaging were used to study the 10º sharp fin interaction. Again, the operating conditions of Baumgartner were replicated as closely as possible to duplicate the incoming boundary layer properties (Table 4.1). The visualizations revealed the expected quasi-conical nature of the interaction.

4.3.1 Surface Flow Visualization

The silicone/titanium dioxide mixture was applied to the model in a similar manner to the 8º compression corner. Three spanwise rows of dots were laid down by syringe upstream of the model. Three lines of dots were laid downstream of the sharp fin leading edge in the expected interaction region. These lines were angled downstream from the model in the interaction zone at a slightly greater angle than the calculated inviscid shock line of 15.6º. This arrangement of dots proved to be sufficient to cover the entire extent of the interaction. The video camera captured the flow of the silicone mixture and still images were grabbed from digitized media versions of the video. A still image from just before tunnel shutdown is shown in Figure 4.11, which readily displays the quasi-conical symmetry of the interaction. Some features of this photograph must be pointed out for clarification. The flow is from left to right. Feature A, just upstream of the sharp fin leading edge is a shadow cast by the edge of the window from the illumination used to brighten the test section. Feature B, is a pressure tap that was found to be slowly leaking, but did not effect the overall structure of the interaction. Feature C is the influence of the flat plate leading edge and sides on the surface flow visualization. Measurements were taken well outside of this region of disturbed flow.

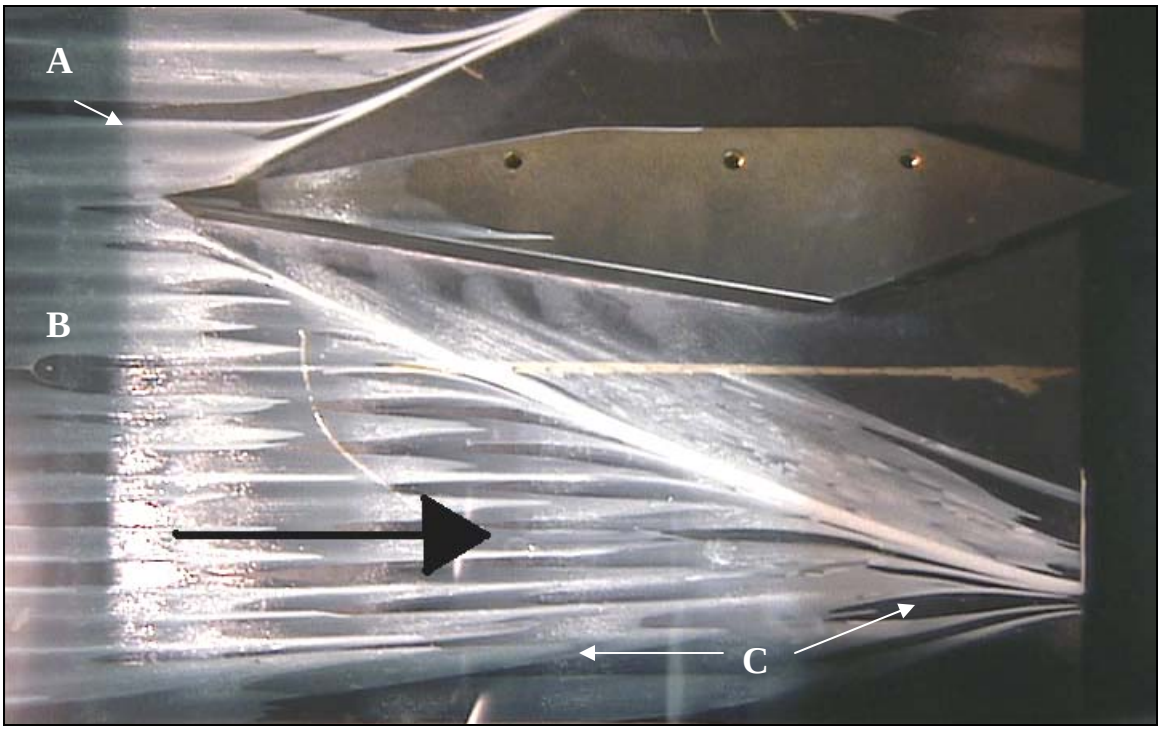

Figure 4.11: Surface flow visualization for the 10° sharp fin interaction at Mach 8.

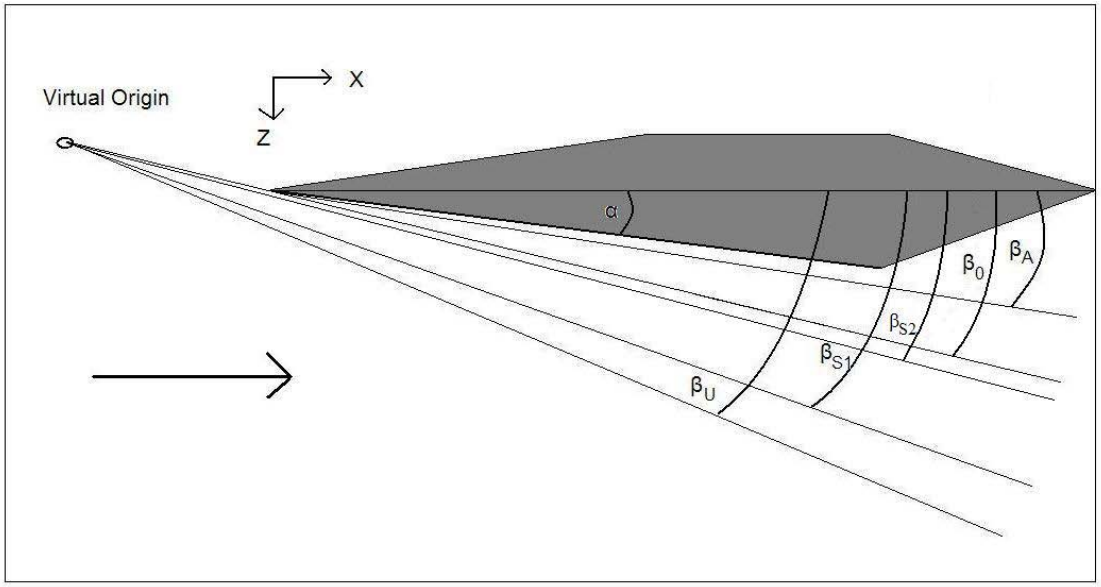

Figure 4.12: Schematic of key features of the quasi-conical interaction of a sharp fin interaction at Mach 8.

With the exception of the inception region (i.e., near the fin leading edge), surface lines could be traced upstream to a common point. A schematic of the flowfield is included as Figure 4.12, which highlights the features of the surface flow: upstream influence (U), inviscid shock surface trace (0), primary separation (S_1), secondary separation (S_2) and primary attachment (A). All lines extrapolated to a common virtual origin, substantiating the conical scaling of the interaction. Both the primary and secondary separation lines were evident. The primary reattachment line was not readily apparent, but was believed to lie very close to the surface of the fin as indicated in Figure 4.12. No indication of the secondary reattachment point was seen in the oil flow visualizations. A summary of the major angles from Figure 4.11 and Figure 4.12 are shown in Table 4.2. Measurements were made by hand from a printed version of Figure 4.12 and are estimated to be accurate within 2 degrees. Angles are relative to the upstream streamwise flow vector.

β_U	β_{S1}	β_{S2}	β_0	β_A
29º	25º	17º	15.6º	12º

Table 4.2: Characteristic angles of the quasi-conical interaction of a 10º sharp fin at Mach 8.

The relationship between shock strength and upstream influence was shown in Equation 1.4. Based on the incoming Mach number, where $\mu_\infty = 7.18º$ and $\beta_0 = 15.6º$, this relationship predicted the upstream influence line to lie at 24º. Equation 1.4 underpredicted the extent of the upstream influence of the interaction by about 5º in this case. The formulation was derived from data in the Mach range of 2 to 4, and has now been shown not to extend to hypersonic Mach numbers.

The upstream influence line, primary separation line and inviscid shock trace could be traced back to a virtual origin, which was located at x = -39 mm (-3.7δ_0) and z = -11 mm (-1.05δ_0) in the coordinates defined in Figure 4.12 where the fin leading edge is the origin. The inception length, defined as the linear distance from the fin leading edge to the beginning of the conical region, was found using the following technique. A straight line was drawn along the primary separation line. The location where this line diverged from the actual separation line was defined as the end of the inception region. Although there is some subjectivity in defining these locations and angles, more sophisticated methods have produced results that do not substantially differ from visual results [cf. Settles and Dolling (1990)]. The inception length found for this configuration was L_i = 36 mm (3.4δ_0) ±10%. The relationship of Inger (1987) relating inception length to the inviscid shock angle predicted the inception length for β_0 = 15.6º to be L_i/δ ≈3.58, which was within experimental error of the measured value from surface flow visualization.

4.3.2 FRS Images

FRS was used to visualize the interaction. As discussed in Chapter 1, the quasiconical symmetry of the interaction suggests that the natural coordinate system is a spherical coordinate frame centered on the virtual origin. This suggests that the most pertinent visual images should be made in planar sheets normal to the inviscid oblique shock generated by the fin. However, the highly swept interaction ($\beta_0 \approx 16º$) at this Mach number caused this type of imaging to be very difficult due to the optical access limitation inherent in the hypersonic wind tunnel. The laser sheet was therefore aligned

with the incoming freestream velocity vector. Images were taken at two spanwise locations to establish the growth of the quasi-conical interaction. The first set of images, shown in Figure 4.13 and Figure 4.14, were taken at z = 21 mm (1.8 δ_0) from the leading edge of the fin. The inviscid shock was readily apparent in these images with the separation shock visible about $3\delta_0$ ahead of the inviscid shock location, in good agreement with the location of the separation line determined from flow visualization images. The point of shock bifurcation (or triple point) was clearly seen just above the boundary layer edge. The turning of the flow was evident downstream of the inviscid shock as the boundary layer appears to be breaking up in the images, but this was simply a result of the structures in the boundary layer having a component of the mean velocity coming out of the image. Significant boundary layer growth was also evident; however the separation bubble appeared dark for reasons discussed earlier with regard to the loss of signal with increasing temperature.

Figure 4.15 and Figure 4.16 shows the FRS images taken at z = 32 mm (2.9 δ_0) from the fin leading edge. The inviscid shock location was not nearly as evident as at z = 21 mm. Reasons for this are unknown, but the shock location was shown by the abrupt change in contrast in the freestream and the triangular shape of the shock bifurcation location. The separation shock was seen extending upstream about $4\delta_0$ from the inviscid shock location in excellent agreement with measurements from surface flow visualization.

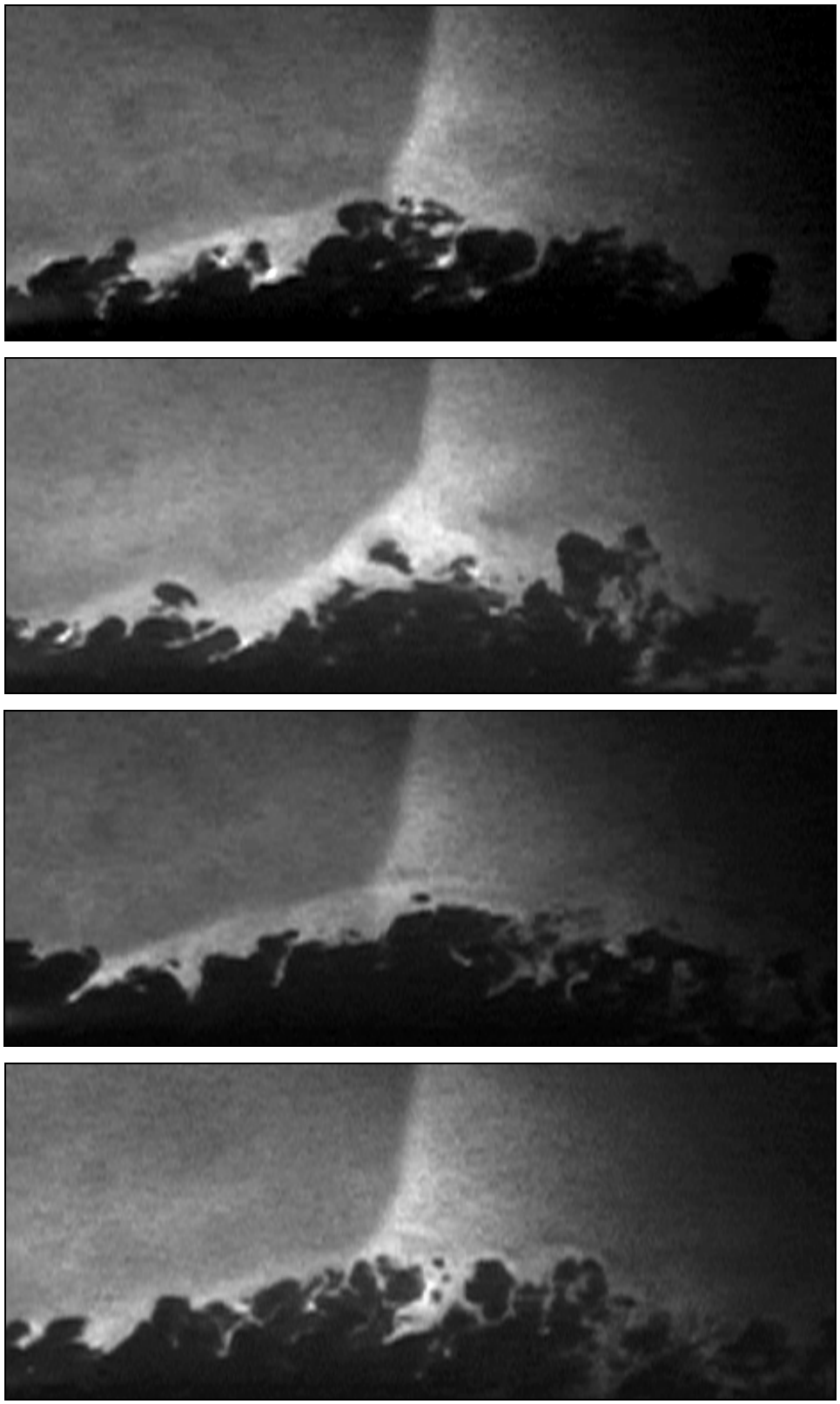

Figure 4.13: Montage 1 of instantaneous FRS images (uncorrelated) at z = 21 mm (1.9 δ_0) from 10° sharp fin. Images are $3\delta_0$ x $6\delta_0$. The wall location coincides with the bottom of each image.

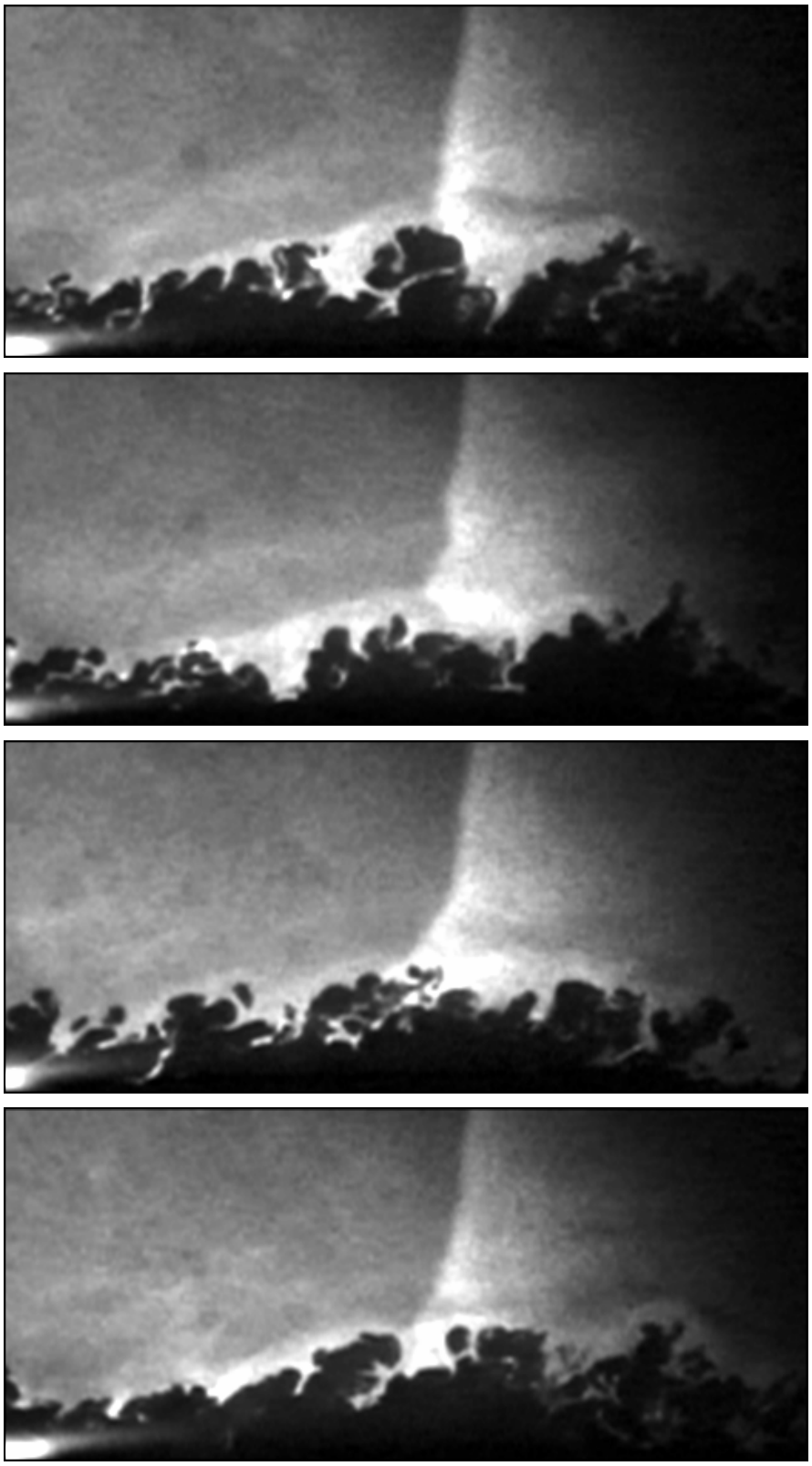

Figure 4.14: Montage 2 of instantaneous FRS images (uncorrelated) at z = 21 mm (1.9 δ_0) from 10º sharp fin. Images are $3\delta_0$ x $6\delta_0$. The wall location coincides with the bottom of each image.

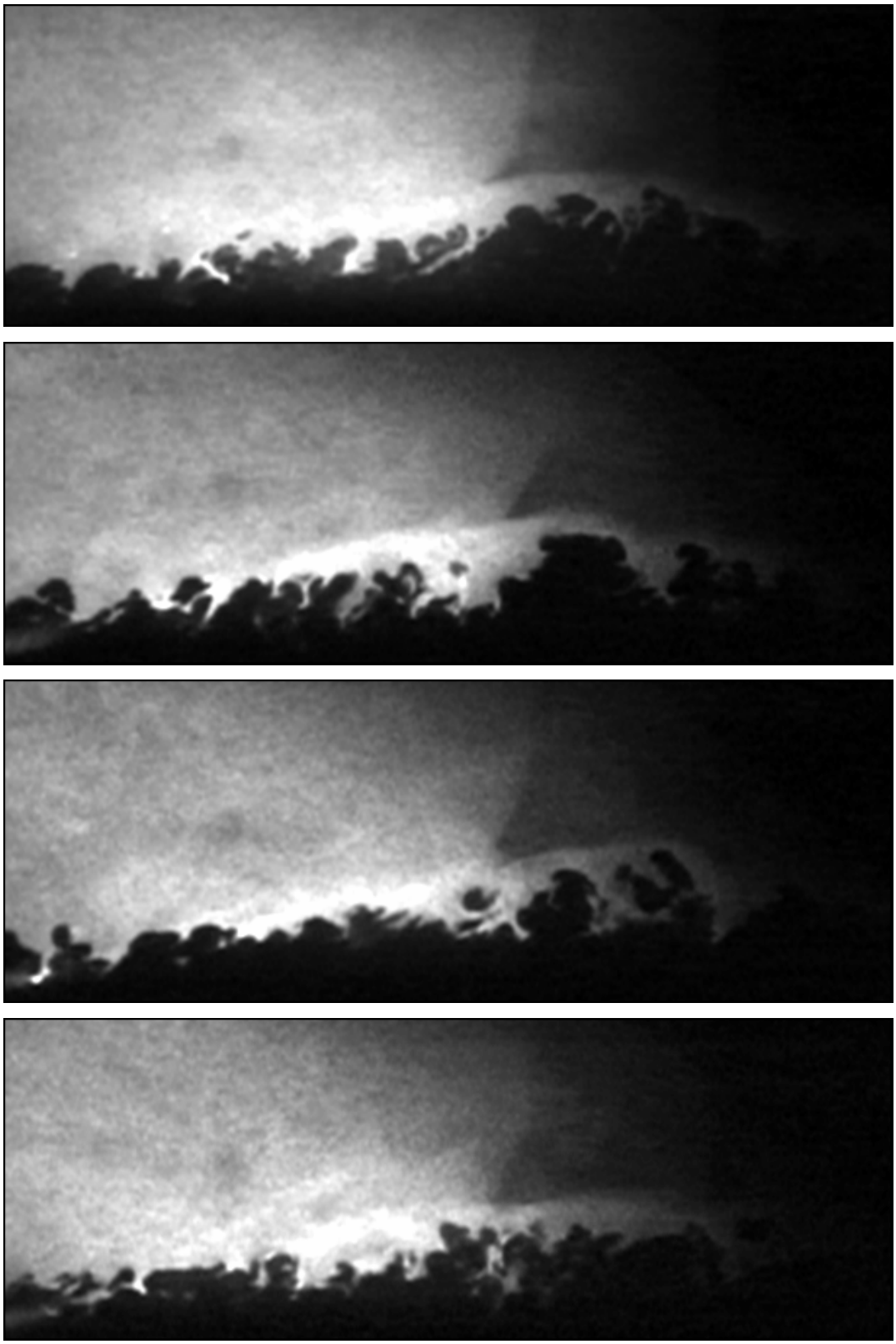

Figure 4.15: Montage 1 of instantaneous FRS images (uncorrelated) at z = 32 mm (2.7 δ_0) from 10° sharp fin. Images are 2.9δ_0 x 7.1δ_0. The wall location corresponds to the bottom of each image.

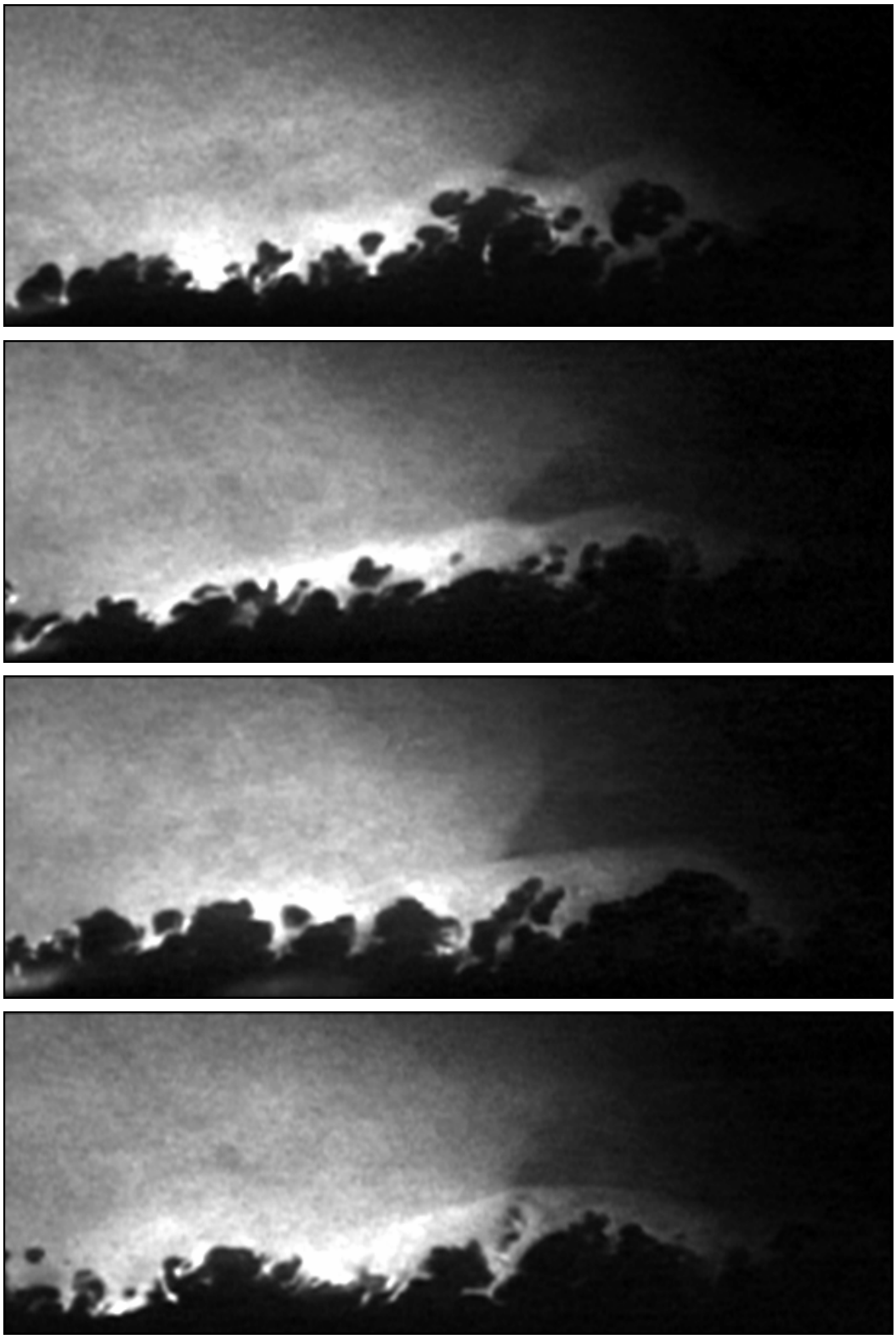

Figure 4.16: Montage 2 of instantaneous FRS images (uncorrelated) at z = 32 mm (2.7 δ_0) from 10º sharp fin. Images are 2.9δ_0 x 7.1δ_0. The wall location corresponds to the bottom of each image.

4.4 Summary

This chapter presented the experimental results of two shock/turbulent boundary layer interactions at Mach 8. Data acquisition and reduction techniques were described with the discussion of the results. The main results from the Mach 8 studies are as follows:

1. Analysis of the mean structure angles and intermittency of the undisturbed boundary layer just upstream of the interactions showed close similarity to the previous studies of the same turbulent boundary layer by Baumgartner (1997).
2. Although expected to separate, the 8º compression corner was shown from flow visualization techniques to remain attached.
3. Analysis of the structure angles from correlations revealed the boundary layer large-scale structures to become more inclined towards the wall surface with an average decrease in angle of 11º.
4. The 10º sharp fin interaction demonstrated a typical quasiconical symmetry beyond the inception region, which measured $3.4\delta_0$, in good agreement with predictors for lower Mach number flows. The virtual conical origin was upstream and offset in the spanwise direction from the leading edge of the fin.
5. FRS images of the 10º sharp fin revealed the lambda shaped shock structure, indicating it to be highly unsteady.

Chapter 5 Summary and Conclusions

This thesis has presented the results of a series of experiments examining shock/turbulent boundary layer interactions in supersonic and hypersonic flows. A 24º compression corner and 12º reflected shock interaction were studied at Mach 2.9 and Re_θ = 2400. An 8º compression corner and 10º sharp fin were studied at Mach 8 and Re_θ = 3500. The flows were investigated using surface oil flow visualizations, surface pressure measurements, mean Pitot pressure and total temperature surveys and filtered Rayleigh scattering. The results of these experiments are expected to be useful for comparison to the DNS computations being performed by Martin (2004), and Wu and Martin (2005).

The incoming boundary layer at Mach 2.9 appeared to be fully turbulent with features of the large scale structures similar to those observed in boundary layers at much higher Reynolds numbers. The 24º compression corner interaction exhibited fully separated flow with separation scales larger than higher Reynolds number flows. The length of the separation bubble at Re_θ = 2400 was almost 50% larger than for Re_θ = 80,000. Large scale structures tended to be more inclined to the surface after the initial compression and 10º turning of the separation shock. The mean position of the turbulent/non-turbulent interface remained invariant, while the intermittency profile became slightly steeper than the profile of the undisturbed boundary layer. The surface pressure distribution revealed a greater initial pressure rise at separation and flatter pressure plateau than higher Reynolds number interactions and velocity profiles revealed the relatively gradual nature of the relaxation of the boundary layer towards equilibrium downstream of separation.

The 12º reflected shock interaction at Mach 2.9 was also found to be highly separated. The velocity profiles revealed the vertical extent of the separation bubble to be approximately equal to the incoming boundary layer height (6.7 mm). FRS images showed the complicated shock system elevated above the mean boundary layer height with the mean shock intersection point at $y/\delta_0 = 2$. The surface pattern revealed the highly three-dimensional nature of this interaction and the large streamwise extent of the separated region. The surface pressure distribution showed an initial pressure rise similar to the 24º compression corner distribution; however the pressure plateau was much broader, extending 6 δ_0 in the streamwise direction. The intermittency profile showed the slight increase in steepness evident in the compression corner intermittency; however, in this case, the mean position of the interface (point where $\lambda = 0.5$) increased by as much as 60% for the locations surveyed.

The 8º compression corner interaction at Mach 8 was expected to separate since the strength of the shock was about the same as the 24º compression corner at Mach 2.9. However, surface flow visualization showed no evidence of separation probably because of the highly inclined nature of the shock that did not emerge from the boundary layer until about $5\delta_0$ downstream of the corner. The FRS images showed the shock deeply entrained in the boundary layer for at least five boundary layer thicknesses downstream of the corner. The shock was seen to penetrate some large scale structures while becoming highly distorted and wrapping around the back side of other structures. These large scale structures were shown to become more inclined to the surface than those of the undisturbed boundary layer, and the average decrease in angle was about 11º with a maximum of 18º. This reduced the average structure angle from 45º to 34º.

The 10º sharp fin interaction at Mach 8 generated the expected quasiconical symmetry with inception length of about $3.4\delta_0$, in excellent agreement with predictors intended for lower Mach numbers. However, the upstream influence line (β_U) was not well predicted by correlations based on lower Mach numbers. Surface flow visualization revealed the quasiconical nature of the interaction with characteristic lines emanating from a common virtual conical origin that was displaced upstream and to the side of the fin leading edge. Streamwise images of the interaction from FRS indicated the presence of the λ shock structure with the location of the separation shock foot in good agreement with the measurements of the separation line using surface flow visualization. The bifurcation of the inviscid and separation shock was observed to be elevated just above the boundary layer edge. The presence of a large separation bubble was indicated by the significant growth of the boundary layer just downstream of the inviscid shock. The subsequent visualization of the boundary layer at a second location further downstream revealed the streamwise extent of the interaction increasing by about 30%. Again, the location of this shock foot agreed well with surface flow visualization measurements of the separation line.

Despite the efforts of this study to provide detailed information on the scales and structure of these interactions, there is a considerable amount of work that could be done to improve the quality of the current data as well as add significantly more information.

The quality of the FRS images obtained in the Mach 2.9 flow was significantly worse than that of those acquired at Mach 8. The most likely explanation for this, although no specific tests were carried out to confirm, was the implementation of the carbon dioxide seeding system. The system was designed for the HyperBLAF, where

CO_2 was injected upstream of the heater, and the flow passed through 280 feet of helical heater pipe in which to uniformly mix the carbon dioxide into the supply air. In the LTVG system, there was only 25 feet of pipe after the injection point at which point the flow encountered a series of meshes and screens which eliminated much of the freestream turbulence, and prevented the carbon dioxide from further mixing with the supply air. A rigorous redesign of the seeding system specifically tailored to the LTVG may help to improve the quality of the FRS images in this study at Mach 2.9.

The purpose of this study was to provide an initial dataset that highlighted the major characteristics of these interactions. The interactions studied here are worthy of a single experimental program each, where a much more detailed story of the interaction could be created. For all the flows, an extensive set of mean flow surveys to characterize the separation bubble and provide more details on the recovery of the boundary layer to equilibrium should be made. Measurements of the unsteady pressure signal would help identify the unsteady nature of the shockwave and separation bubble. DNS computes the turbulent flowfield, so experimental studies of the turbulent flowfield using hot-wire anemometry or LDV would allow a direct comparison of the turbulence. Imaging the interaction using a MHz frame rate camera and FRS would allow the observation of individual structures in the boundary layer interacting with the shock. These are just a few general suggestions for future research on the interactions investigated in this study.

The majority of research on compression corner interaction has taken place at supersonic Mach numbers, mostly at Mach 3. A detailed study of compression corners at hypersonic Mach numbers has not taken place to the author's knowledge. The fact that the 8^o compression corner interaction did not appear to separate suggests that a

comprehensive study of various compression corner strengths is necessary to fully understand separation at hypersonic Mach numbers. The same general statement can be made for sharp fin interactions. The majority of the work was done at moderate Mach numbers where the predictors and relationships for the scaling of the interaction exist. The few hypersonic experiments have shown that these predictors need slight adjustment for the higher Mach numbers, particularly for β_U. A systematic study of sharp fin interactions at hypersonic Mach numbers would help to understand any differences in the two Mach number regimes.

References

Adams, N.A., "Direct Simulation of the Turbulent Boundary Layer along a Compression Ramp at M=3 and Re_0=1685,'' *Journal of Fluid Mechanics*, Vol. 420, 2000, pp. 47-83.

Alvi, F.S., and Settles, G.S., "A Physical Model of the Swept Shock/Boundary Layer Interaction Flowfield," AIAA Paper No. 91-1768, June 1991.

Ardonceau, P.L., "The Structure of Turbulence in a Supersonic Shock-Wave/Boundary-Layer Interaction," *AIAA Journal*, Vol. 22, No. 9, September 1984, pp. 1254-1262.

Baumgartner, M.L., "Turbulence Structure in a Hypersonic Boundary Layer," PhD Dissertation, Mechanical and Aerospace Engineering Department, Princeton University, June, 1997.

Baumgartner, M.L, Erbland, P.J., Etz, M.R., Yalin, A., Muzas, B.K., Smits, A.J., Lempert, W.R., and Miles, R.B., "Structure of a Mach 8 Turbulent Boundary Layer," AIAA Paper No. 97-0765, January 1997.

Bourgoing, A. and Reijasse, P., "Experimental Analysis of unsteady separated flow in a planar nozzle," *Proceedings of International Symposium on Shock Waves*," University of Texas Forth Worth, Texas, 2001.

Delery, J. and Marvin, J.G., "Shock-Wave Boundary Layer Interactions," AGARD-AG-280, 1986.

Doerffer, P. and Szawba, R., "Shock Wave/Boundary Layer Interaction Control by Streamwise Vortices," *Proceedings of ICTAM XXI*, Warsaw, Poland, 2001.

Dolling, D.S., Cosad, C.D., Bogdonoff, S.M., and Vas, I.E., "A Three-Dimensional Study of Fin-Induced Shock Wave Turbulent Boundary Layer Interaction," ARO-14026, 1977.

Dolling, D.S. and McClure, W.B., "Flowfield Scaling in Sharp Fin-Induced Shock Wave/Turbulent Boundary-Layer Interaction," *AIAA Journal*, Vol. 23, No. 2, 1985, pp. 201-206.

Dolling, D.S. and Murphy, M., "Unsteadiness of the Separation Shock Wave Structure in a Supersonic Compression Ramp Flowfield," *AIAA Journal*, Vol. 21, No. 12, December, 1983, pp. 1628-1634.

Dupont, P., Haddad, C. and Debieve, J.F., "Space and Time Organization in a Shock Induced Separated Boundary Layer," *Journal of Fluid Mechanic*, to appear.

Dussauge, J.P., Dupont, P. and Debieve, J.F., "Unsteadiness in Shock Wave Boundary Layer Interactions with Separation," *AAAF 40th Colloquium on Applied Aerodynamics*, Toulouse, France, 2005.

Erbland P.J., Baumgartner M.L., Yalin A.P. et al, "Development of Planar Diagnostics for Imaging Mach 8 Flowfields using Carbon Dioxide and Sodium Seeding," AIAA Paper No. 97-0154, 1997.

Etz, M.R., "The Effects of Transverse Sonic Gas Injection on a Hypersonic Boundary Layer," MSE Thesis, Mechanical and Aerospace Engineering Department, Princeton University, 1998.

Fitzgibbon, A.W., Pilu, M., and Fisher, R.B., "Direct Least Squares Fitting of Ellipses," *IEEE Transactions on Pattern Analysis and Machine Intelligence*, Vol. 21, No. 5, May 1999.

Forkey, T.N., "Development and Demonstration of Filtered Rayleigh Scattering: A Laser Based Flow Diagnostic for Planar Measurement of Velocity, Temperature and Pressure," Ph.D. Dissertation, Mechanical and Aerospace Engineering Department, Princeton University, 1996.

Garg, S. and Settles, G.S., "Wall Pressure Fluctuations beneath Swept Shock/Boundary-Layer Interactions," AIAA Paper No. 93-0384, January 1993.

Gibson, B. and Dolling, D.S., "Wall Pressure Fluctuations near Separation in a Mach 5, Sharp Fin-Induced Turbulent Interaction," AIAA Paper No. 91-0646, January 1991.

Green, J.E., "Interaction between Shock-Waves and Turbulent Boundary Layers." *Progress in Aerospace Sciences*, Vol. 11, 1970.

Hayakawa, K., and Squire, L.C., "The Effect of the Upstream Boundary-Layer State on the Shock Interaction at a Compression Corner," *Journal of Fluid Mechanics*, Vol. 122, 1982, pp. 369-394.

Inger, G.R., "Spanwise Propagation of Upstream Influence in conical Swept Shock Boundary-Layer Interactions," *AIAA Journal*, Vol. 25, No. 2, pp. 287-293.

Keyes, F.G., "The Heat Conductivity, Viscosity, Specific Heat and Prandtl Numbers for Thirteen Gases," Project Squid, TR 37, Massachusetts Institute of Technology, Cambridge, MA, 1952.

Knight, D., "RTO WG 10: Test Cases for CFD Validation of Hypersonic Flight," AIAA Paper No. 2002-0433, January 2002.

Knight, D., Tan, H., Panaras, A., and Zheltovodov, A., "RTO WG 10: CFD Validation of Shock Wave Turbulent Boundary Layer Interactions," AIAA Paper No. 2002-0437, January 2002.

Klebanoff, P.S., "Characteristics of Turbulence in a Boundary Layer with Zero Pressure Gradient," NACA Report 1247, 1955.

Knight, D.D., Horstman, C.C. and Monson, D.J., "The Hypersonic Shock Wave-Turbulent Boundary Layer Interaction Generated by a Sharp Fin at Mach 8.2," AIAA Paper No. 92-0747, January 1992.

Knight, D.D., Horstman, C.C., Bogdonoff, S.M. and Shapey, B.L., "Structure of Supersonic Turbulent Flow Past a Sharp Fin," *AIAA Journal*, Vol. 25, No. 10, 1987, pp. 1331-1337.

Kuntz, D.W., Amatucci, V.A. and Addy, A.L., "Turbulent Boundary-Layer Properties Downstream of the Shock-Wave/Boundary-Layer Interaction," *AIAA Journal*, Vol. 25, No. 5, May 1987, pp. 668-675.

Kussoy, M.I., Kim, K.-S. and Horstman, K.C., "An Experimental Study of a Three-Dimensional Shock Wave/Turbulent Boundary-Layer Interaction at a Hypersonic Mach Number," AIAA Paper No. 91-1761, June 1991.

Law, C.H., "Three-Dimensional Shock Wave Turbulent Boundary Layer Interactions at Mach 6," ARL-TR-75-0191, June 1975.

Magruder, T.D., "An Experimental Study of Shock/Shock and Shock/Boundary Layer Interactions on Double-Cone Geometries in Hypersonic Flow," MSE Thesis, Mechanical and Aerospace Engineering Department, Princeton University, 1997.

Miles, R.B., Forkey, J.N. and Lempert, W.R., "Filtered Rayleigh Scattering Measurements in Supersonic/Hypersonic Facilities," AIAA Paper 92-3894, 1997.

Milton, J.S. and Arnold, J.C., *Probability and Statistics in the Engineering and Computing Sciences*, McGraw-Hill: New York, 1986.

Orszag, S.A., and Patterson, G.S., "Numerical Simulation of Three-Dimensional Homogeneous Isotropic Turbulence," *Phys. Rev. Lett.*, Vol. 28, 1972, pp. 76-79.

Perry, A.E. and Chong, M.S., "A Description of Eddying Motions and Flow Patterns using Critical-Point Concepts," *Annual Review of Fluid Mechanics*, Vol. 19, 1987, pp. 125-155.

Poggie, J., "Quantitative Flow Visualization applied to the Study of Compressible Turbulent Flow," MSE Thesis, Department of Mechanical and Aerospace Engineering, Princeton University, 1991.

Pope, A. and Goin, K.L., *High-Speed Wind Tunnel Testing*, Robert Krieger Publishing, 1978.

Rai, M.M. and Moin, P., "Direct Numerical Simulation of Turbulent Flows using Finite-Difference Schemes," AIAA Paper No. 89-0369, January 1989.

Reynolds, W.C., "The Potential and Limitations of Direct and Large Eddy Simulations," Lecture Notes in Physics 357, March 1989, pp. 313-343.

Roshko, A. and Thomke, G.J., "Flare Induced Interaction Lengths in Supersonic, Turbulent Boundary-Layers, *AIAA Journal*, Vol. 14, No. 7, July 1976, pp. 873-879.

Selig, M.S., Andreopoulos, J., Muck, K.C., Dussauge, J.P. and Smits, A.J., "Turbulence Structure in a Shock Wave/Turbulent Boundary-Layer Interaction," *AIAA Journal*, Vol. 27, No. 7, July 1989, pp. 862-869.

Settles, G.S., "An Experimental Study of Compressible Turbulent Boundary Layer Separation at High Reynolds Number, Ph.D. Dissertation, Aerospace and Mechanical Sciences Dept., Princeton University, September 1975.

Settles, G.S., "Swept Shock/Boundary Layer Interactions – Scaling Laws, Flowfield Structure, and Experimental Methods," *Special Course on Shock-Wave/Boundary-Layer Interactions in Supersonic and Hypersonic Flows*, AGARD Report 792, 1993.

Settles, G.S. and Bogdonoff, S.M., "Separation of a supersonic Turbulent Boundary-Layer at Moderate to High Reynolds Numbers," AIAA Paper No. 73-666, July 1973.

Settles, G.S., Bogdonoff, S.M., and Vas, I.E., "Incipient Separation of a Supersonic Turbulent Boundary Layer at High Reynolds Number," *AIAA Journal*, Vol. 14, No.1, January 1976, pp. 50-56.

Settles, G.S. and Dodson, L.J., "Supersonic and Hypersonic Shock/Boundary Layer Interaction Database," *AIAA Journal*, Vol. 32, No. 7, July 1994, pp. 1377-1383.

Settles, G.S. and Dolling, D.S., "Swept Shock/Boundary Layer Interactions – Tutorial and Update," AIAA Paper No. 90-0375, January 1990.

Settles, G.S., Fitzpatrick, T.J., and Bogdonoff, S.M., "A Detailed Study of Attached and Separated Compression Corner Flowfields in High Reynolds Number Supersonic Flow," AIAA Paper No. 78-1167, July 1978.

Settles, G.S. and Dodson, L.J., "Supersonic and Hypersonic Shock/Boundary Layer Interaction Database," *AIAA Journal*, Vol. 32, No. 7, July 1994, pp. 1377-1383.

Settles, G.S. and Teng, H.-Y., "Flow Visualization of Separated 3-D Shock Wave/Turbulent Boundary Layer Interactions," AIAA Paper No. 82-0229, January 1982.

Schmisseur, J.D. and Dolling, D.S., "Unsteady Separation in Sharp Fin-Induced Shock Wave/Turbulent Boundary Layer Interaction at Mach 5," AIAA Paper No. 92-0748, January 1992.

Shang, J.S., Hankey Jr., W.L., and Law, C.H., "Numerical Simulation of Shock-Wave/Turbulent Boundary Layer Interaction," *AIAA Journal*, Vol. 14, No. 10, October 1976, pp. 1451-1457.

Smith, D.R., Poggie, J., Konrad, W. and Smits, A.J., "Visualization of the Structure of Shock Wave Turbulent Boundary Layer Interactions using Rayleigh Scattering," AIAA Paper No. 91-0651, January 1991.

Smits, A.J., "Viscous Flows and Turbulence," *Lecture Notes in Fluid Mechanics*, 2000.

Smits, A.J. and Muck, K.C., "Experimental Study of Three Shock Wave/Turbulent Boundary Layer Interactions," *Journal of Fluid Mechanics*, Vol. 182, 1987, pp. 291-314.

Smits, A.J. and Dussauge, J.P., *Turbulent Shear Layers in Supersonic Flows*, American Institute of Physics: Woodbury, NY, 1996.

Smits, A.J. and Dussague, J.P., *Turbulent Shear Layers in Supersonic Flows*, 2nd Edition, to appear 2005.

Spaid, F.W. and Frishett, J.C., "Incipient Separation of a Supersonic, Turbulent Boundary-Layer, Including Effects of Transfer." *AIAA Journal*, Vol. 10, No. 7, 1972, pp. 915-922.

Spalart, P.R., "Direct Numerical Simulation of a Turbulent Boundary Layer at Re_θ = 1410," *Journal of Fluid Mechanics*, Vol. 187, pp. 61.

Tran, T.T., Tan, D.K.M, and Bogdonoff, S.M., "Surface Pressure Fluctuations in a Three-Dimensional Shock Wave/Turbulent Boundary Layer Interaction at Various Shock Strengths," AIAA Paper No. 85-1562, July 1985.

Wu, M. and Martin, M.P., "Direct Numerical Simulation of Shockwave/Turbulent Boundary Layer Interaction," AIAA Paper No. 2004-2145, June 2004.

Wu, M., Bookey, P.B., Martin, P.M. and Smits, A.J., "Analysis of Shockwave/Turbulent Boundary Layer Interaction using DNS and Experimental Data," AIAA Paper No. 2005-0310, January 2005.

Zheltovodov, A.A., "Shock Waves/Turbulent Boundary-Layer Interactions – Fundamental Studies and Applications," AIAA Paper No. 96-1977, June 1996.